Wet chemical precipitation of ZnO from Cl-rich solutions – an innovative method for the recovery of Zn from municipal solid waste incineration fly ash

Dissertation zur Erlangung des Doktorgrades

an der Fakultät für Geowissenschaften

der Ludwig-Maximilians-Universität München

Vorgelegt von

M. Sc. Kai Kevin Tandon

München, 08.09.2021

Erstgutachterin: Prof. Dr. Soraya Heuss-Aßbichler

Zweitgutachter: Prof. Dr. Wolfgang Schmahl

Tag der mündlichen Prüfung: 21.01.2022

Waste is what is left when imagination fails

- Christian Ekberg 2007, Professor at Chalmers University of Technology, Gothenburg -

Table of Contents

Acknowledgements

First, I want to express my sincere gratitude to my supervisor, Prof. Dr. Soraya Heuss-Aßbichler. Without your persistence in finding funding opportunities, this research would not have been possible. Your continuous support, reviews, the creative and constructive discussions have truly improved this work. Thank you for letting me tackle and learn so many different tasks.

I also want to thank Prof. Dr. Wolfang Schmahl, who agreed to be the second reviewer of this thesis and for the opportunity to use the devices of the Section for Crystallography.

Iphi, thank you for being part of our working group, the support, the reviews, and that you were always open for discussions and never get tired of looking into details together. I also appreciate the support of the other members of our working group over the last years: Adriana Gerz, Alexandra Huber, Dr. Werner Ertel-Ingrisch, Andreas Appel, Katharina Engels, Sebastian Gölitz, Valentin Schaller, and Dr. Melanie John-Stadler.

In addition, many other people from the Department of Earth and Environmental Sciences have been supporting this work: SEM would not have been possible without the help and supervision of PD Dr. Corrado Cimarelli and Dr. Erika Griesshaber. Dr. Donja Aßbichler has provided the opportunity, advice, and help on all questions related to XRF. Antonia Wimmer and Moritz Zenkert were also always on hand regarding lab questions and support with measurements. So was the workshop, who always found the time if problems with equipment occurred.

I would like to acknowledge the members of the ZIM-Project for the scaling of the laboratory process, James Babbé and Silvia Koch, AquaChem GmbH, as well as Kerstin Zacherl-John, E&P Anlagenbau. Thank you, Dr. Irene Lindner, Gerhard Meier, and Michael Funk from municipal solid waste incineration plant Ingolstadt for providing samples and help. Michael Funk was always there when I needed further information, and his creative ideas and hands-on mentality helped to solve some obstacles during the planning of the pilot plant. Thank you, Dr. Jürgen Diemer, from the Bavarian Environment Agency, and Dr. Ottmar Hofmann and Christian Obermeier, from the Stadtwerke München for the analytical support.

Last but not least, I would like to thank my family and friends, who always supported me over the years, no matter what. It would also have been great if my mother, Angela Tandon, would have been part of this moment. Thank you, Romi, for taking the time to proofread the work despite your other responsibilities. Thank you, Georgie; I don’t know what I would have done without your support and endless motivating words. Sorry for the countless moments when I was somewhere else with my mind and for so many times preparing meals, proofreading, and enduring my moods – thank you!

List of abbreviations

APC	air pollution control
AQ	synthetic aqueous solution
FGT	flue gas treatment
FLUWA	fly ash washing
FLUREC	fly ash recycling
LCA	life cycle assessment
LDH	layered double hydroxides
LHS	layered hydroxide salts
L/S	liquid to solid
MSW	municipal solid waste
MSWI	municipal solid waste incineration
POP´s	persistent organic pollutants
PCDDs	polychlorinated dibenzo-p-dioxins
PDCFs	polychlorinated dibenzofurans
SDG´s	sustainable development goals
SPOP	Specific Product-Oriented Precipitation
S/S	stabilization/solidification

Abstract

Recently, the supply of raw materials has come more into focus and with it the potential of waste as a source of secondary raw materials. Municipal solid waste incineration (MSWI) fly ash is regarded as hazardous waste due to its high content of easily soluble salts, heavy metals, and persistent organic pollutants. Therefore, it is disposed of in special landfills, either directly or after processing by stabilization/solidification techniques or recycled underground as filler. The usual disposal or backfilling it underground means losing its valuable resources, especially Zn, which is highly enriched in fly ash.

There are several methods to treat fly ash. One example is the extraction of heavy metals by acidic leaching. The FLUWA (acidic fly ash washing) process, for example, refined the efficient extraction of most heavy metals from fly ash. With this process, easily soluble salt components also concentrate in the solution. Treatment of such eluates with milk of lime results in a thixotropic slurry with heavy metal- and salt-rich hydroxides. The high concentration of Cl in these sludges prevent the recovery of the heavy metals, as it contributes to the corrosion of the treatment facilities. Therefore, these sludges must be disposed of as hazardous waste. Only a few processes focus on the recovery of metals like Zn from such eluates. FLUREC (fly ash recycling) is a novel process for recovering Zn as a high-purity metal from MSWI fly ash after applying FLUWA. However, it is also a complex and energy-intensive hydrometallurgical process.

A new sustainable process represents the "specific product-oriented precipitation" (SPOP) of heavy metals, which focuses on practicability and low energy costs. The successful recovery of heavy metals from SO_4-rich industrial wastewater, e.g., from the electroplating industry, shows that SPOP is a promising alternative to the usual treatment with milk of lime. The concentration of the metals in the precipitate and the filtrate is determined by the specific phase formation. It can be directly controlled by adjusting parameters such as the composition of the solution, temperature, pH, and optionally Fe-addition. However, the influence of highly saline solutions on the precipitation of phases has not been studied so far. A prerequisite for a viable process in highly saline solutions is that Zn is enriched in the residue, and its Cl-concentration is low to prevent corrosion of the recycling facilities. Ideally, the proportion of hydroxides in the precipitates is low, and the filtrate meets the discharge limits after the treatment process. The criteria are best fulfilled by precipitating ZnO, where Zn is enriched by 80 wt.-%, while the Cl concentration remains low. To date, no routine exists for the synthesis of ZnO from Cl-rich solutions at low temperatures < 110 °C.

This thesis presents two new SPOP-based processes developed in a model system to precipitate Zn as ZnO from Cl-rich solutions. The basis for the synthetic Cl-rich solution was real wastewater from MSWI fly ash eluates. The precipitation of the phases depends strongly on the reaction conditions.

Gordaite $NaZn_4(SO_4)(OH)_6Cl \cdot 6H_2O$ is the stable phase at room temperature. ZnO can be achieved at 60 °C with a high yield (99.9 %). The results show that the direct formation of ZnO can be controlled by varying the alkalization rate and temperature. Optimizing the reaction conditions makes it possible to synthesize ZnO directly as a single-phase even at lower temperatures < 110 °C: a) between 60 °C – 80 °C with a medium alkalization rate or b) < 40 °C by increasing the alkalization rate. The underlying reaction mechanism is derived. It is based on the reaction of tetrahydroxozincate ions $[Zn(OH)_4]^{2-}$ to ZnO immediately after alkalization of the Zn-solution.

It was also possible to obtain ZnO in a two-step process by aging previously synthesized Gordaite in suspension. Gordaite is not stable ≥ 80 °C. In general, the higher the aging temperature, the faster the transformation reaction. At 110 °C and without stirring, Gordaite completely transforms to ZnO within 3h. Stirring during aging favors the transformation of Gordaite to ZnO. The reaction mechanism for the formation of ZnO during aging is based on dissolution-precipitation. During this process, the dissolving Gordaite crystals act as heterogeneous sites for topotactic ZnO nucleation, and the ZnO crystals grow according to Ostwald-ripening.

Based on the results in the model system, two treatment concepts were developed. These two concepts, the direct precipitation method and the aging method, were tested with two real wastewater samples from the MSWI plant Ingolstadt. In both cases, ZnO could be recovered as the main phase. Thus, the first step towards a viable industrial process was achieved.

Zusammenfassung

In den letzten Jahren rückte die Bedeutung einer nachhaltigen Rohstoffversorgung immer mehr in den Fokus und damit auch das Potenzial von Abfällen als Quelle für Sekundärrohstoffe. Flugaschen aus der kommunalen Müllverbrennung gelten aufgrund ihres hohen Gehalts an leichtlöslichen Salzen, Schwermetallen und persistenten organischen Schadstoffen als gefährlicher Abfall. Sie werden daher entweder direkt oder nach vorangegangener Behandlung durch Stabilisierungs-/Verfestigungsverfahren auf Sondermülldeponien oder Untertage im Versatz entsorgt. Jedoch sind in den Flugaschen kostbare Ressourcen enthalten, insbesondere Zink ist darin angereichert. Bei den üblichen Entsorgungsmethoden oder dem Versatz Untertage gehen diese verloren.

Es gibt verschiedene Methoden zur Behandlung von Flugaschen aus der Müllverbrennung. Ein Beispiel ist die Extraktion der darin enthaltenen Schwermetalle durch Säuren. Die FLUWA (saure Flugaschewäsche) ist ein solches Verfahren, das auf dem Extraktionsprozess basiert und weiterentwickelt wurde. Dadurch erhöht sich in den Lösungen allerdings nicht nur die Schwermetallkonzentration, sondern auch die Konzentration von leicht löslichen Salzen. Die übliche Behandlung solcher Eluate mit Kalkmilch führt zu einem thixotropen Hydroxidschlamm, welcher schwermetallhaltig und salzreich ist. Die hohe Cl-Konzentration in diesen voluminösen Schlämmen verhindert ein Recycling, da dies zur Korrosion der Verwertungsanlagen führen würde. Daher werden diese Schlämme als Sondermüll entsorgt.

Es gibt nur wenige Verfahren, die eine Rückgewinnung der Metalle wie Zn aus diesen Eluaten zum Ziel haben. FLUREC (Flugaschenrecycling) ist ein neues Verfahren, das darauf abzielt, Zn als hochreines Metall aus den Flugasche-Eluaten der Müllverbrennung nach Anwendung der FLUWA zurückzugewinnen. Bisher ist es das Verfahren mit den geringsten Umweltauswirkungen. Allerdings handelt es sich um einen komplexen und energieintensiven hydrometallurgischen Prozess.

Ein neuer, innovativer Ansatz ist die „spezifische produkt-orientierte Präzipitation“ (SPOP) von Schwermetallen. Hierbei stehen Praktikabilität und geringe Energiekosten im Zentrum. Die erfolgreiche Rückgewinnung von Schwermetallen aus SO_4-reichen Industrieabwässern, wie beispielsweise aus der Galvanik, zeigt, dass SPOP eine vielversprechende und umweltschonende Alternative zur üblichen Behandlung mit Kalkmilch ist. Der Metallgehalt im Rückstand und die Konzentration der Schwermetalle im Filtrat werden durch die spezifische Phasenbildung bestimmt. Diese kann durch die Einstellung der Parameter wie Zusammensetzung der Lösung, Temperatur, pH-Wert und optionaler Fe-Zugabe direkt gesteuert werden. Der Einfluss von stark salzreichen Lösungen auf die Phasenzusammensetzung wurde bisher allerdings noch nicht untersucht. Eine Voraussetzung für ein umsetzbares Verfahren aus salzreichen Lösungen in der Praxis ist, dass Zn im Rückstand angereichert wird und die Cl-Konzentration gering bleibt, um eine Korrosion der

Verwertungsanlagen zu verhindern. Im Idealfall ist der Anteil an Hydroxiden in den Fällungsrückständen nach dem Aufbereitungsprozess gering und das Filtrat erfüllt die Grenzwerte für die (in)direkte Einleitung. Diese Anforderungen werden am besten durch die Ausfällung von Zinkit (ZnO) erfüllt, wo Zn um 80 Gew.-% angereichert wird und die Cl-Konzentration niedrig bleibt. Bisher gibt es jedoch keine Methode für die Synthese von ZnO aus Cl-reichen Lösungen bei niedrigen Temperaturen < 110 °C.

Im Rahmen dieser Arbeit wurden zwei neue SPOP-basierte Verfahren in einem Modellsystem entwickelt, um Zn als ZnO aus Cl-reichen Lösungen auszufällen, entweder direkt oder mittels eines Zweistufenprozesses. Die Zusammensetzung der synthetischen Cl-reichen Lösung für die Fällungsexperimente basiert auf einem realen Flugasche-Eluat aus einer Müllverbrennungsanlage nach Behandlung mit FLUWA. Die Ergebnisse zeigen, dass die Ausfällung der Phasen stark von den Reaktionsbedingungen abhängt. Gordait, $NaZn_4(SO_4)(OH)_6Cl \cdot 6H_2O$, ist bei Raumtemperatur die stabile Phase. ZnO kann bei 60 °C direkt mit einer hohen Ausbeute (99,9 %) synthetisiert werden. Dabei kann die direkte Ausfällung von ZnO aus der Lösung durch Variation der Alkalisierungsrate und Temperatur gesteuert werden. Durch Optimierung der Reaktionsbedingungen war es möglich, ZnO reinphasig auch bei niedrigeren Temperaturen < 110 °C direkt zu synthetisieren: a) zwischen 60 °C - 80 °C bei mittlerer Alkalisierungsrate oder b) < 40 °C durch Erhöhung der Alkalisierungsrate. Der zugrunde liegende Reaktionsmechanismus beruht auf der Reaktion von Tetrahydroxozinkat-Ionen $[Zn(OH)_4]^{2-}$ zu ZnO unmittelbar nach der Alkalisierung der Zn-Lösung.

Das zweite entwickelte Verfahren zielt auf die Ausfällung von ZnO mittels eines Zweistufenprozesses ab. Dabei wird zuvor synthetisierter Gordait in Suspension gealtert. Die Untersuchungen haben gezeigt, dass Gordait in Suspension ≥ 80 °C nicht stabil ist. Bei 110 °C und ohne Rühren der Suspension wandelt sich Gordait innerhalb von 3 Stunden vollständig in ZnO um. Je höher dabei die Alterungstemperatur ist, desto schneller verläuft die Umwandlungsreaktion. Rühren während der Alterung begünstigt die Umwandlung. Die Ergebnisse zeigen, dass der zugrunde liegende Reaktionsmechanismus zur Bildung von ZnO während der Alterung auf einer Lösungs-Fällungsreaktion beruht. Hierbei wachsen die ZnO-Kristalle topotaktisch auf den sich lösenden Gordait-Kristallen auf. Die Zinkit-Kristalle wachsen daraufhin nach dem Prinzip der Ostwald-Reifung.

Um die Anwendung der im Modellsystem erarbeiteten Prozesse zu zeigen, wurden zwei Behandlungskonzepte erarbeitet. Beide Konzepte, die direkte Fällungsmethode und die Alterungsmethode, wurden mit jeweils einem realen Abwasser aus der Müllverbrennungsanlage Ingolstadt nach der FLUWA getestet. In beiden Fällen konnte ZnO als Hauptphase ausgefällt werden. Das bedeutet, dass das in dieser Arbeit entwickelte Verfahren in der Praxis umsetzbar ist.

Publications and contribution of authors

As a rule, Zn-rich wastewater is treated and disposed of. One example of Zn-rich wastewater is the eluate of municipal solid waste incineration (MSWI) fly ash, a serious problem due to the significantly enriched concentration of Cl and other heavy metals regardless of Zn. This thesis aims to develop a process to precipitate ZnO from Cl-rich solutions, identify the optimal conditions for ZnO precipitation in a model system, and test whether this process can be applied to MSWI fly ash eluates. The basis of the wet chemical precipitation process used in this thesis is the “Specific Product-Oriented Precipitation” (SPOP). SPOP was initially developed in the working group of Prof. Dr. Soraya Heuss-Aßbichler at the Ludwig-Maximilians-Universität München to treat Cl-poor and SO_4-rich industrial wastewater with heavy metal concentrations up to 25 g/l.

Parts of the results presented in this thesis were collected during several research projects within the last few years:

- A feasibility study in cooperation with MSWI plant Ingolstadt about the “Rückgewinnung von Buntmetallen aus Industrieabwässern – Umsetzbarkeit im neuen Anwendungsbereich Müllverbrennungsanlagen (MVA)-Rückstände” financiated by Zweckverband Ingolstadt.
- After the promising results of the feasibility study, a project was started together with three industrial partners within the framework of the “Zentrales Innovationsprogamm Mittelstand/Central Innovation Program for small and medium-sized enterprises (SMEs)” funded by the Federal Ministry for Economic Affairs and Energy. The project entitled “Innovative Entwicklung des SPOP-Verfahrens zur Rückgewinnung von Buntmetallen aus Flugaschen der Müllverbrennung für die breite Anwendung in MVA´s und Implementierung in eine innovative Abwasseraufbereitungsanlage mit integrierter Filterpresse (ZF4585201CM8)” had three objectives:
  - (i) enhancement of the laboratory process for the precipitation of Zn from fly ash.
  - (ii) Based on that, the transfer of this process to the pilot plant scale in collaboration with a plant engineering company (E&P Anlagenbau) and the MSWI plant Ingolstadt, and
  - (iii) to realize the solid-fluid-separation with a filtration specialist (Aquachem GmbH Filtrationstechnik).
- Some of the results were also collected in the following project: “Gesamtkonzept zur Umsetzung der hydroxidfreien Fällung von Metallen aus Abwässern verschiedener Branchen: Bau einer portablen Technikumsanlage (BAFOISoFo-71263)" funded by the Bavarian Ministry for the Environment and Consumer Protection.

Two different processes were developed to precipitate ZnO from saline solutions. These two processes have been submitted for patenting on 03.09.2021 (Verfahren und Vorrichtung zur Synthese von Zinkit (ZnO)). Before completion of the patent application, the core results of this work on the precipitation of ZnO from Cl-rich solutions were not allowed to be published. Independently, several aspects of the research have been presented in publications, and sections from them have been adopted in the various chapters of this thesis:

- **Tandon, K.**, John, M., Heuss-Aßbichler, S. and Schaller, V. (2018) Influence of Salinity and Pb on the precipitation of Zn in a Model System. Minerals 8(2).
  Submitted: 19 December 2017; accepted: 22 January 2018; published: 26 January 2018.
    - Parts of the content of this publication are used in chapters 1 (introduction) and 4 (material and methods), and the content of the publication is presented in chapter 5.1.
    - I conceived and designed the experiments together with Dr. Melanie John-Stadler. Valentin Schaller carried out part of the experiments as a student assistant. Some series of experiments were the content of his bachelor's thesis. I conducted the mineralogical characterization and chemical analysis with the support of Valentin Schaller. All authors discussed and interpreted the data. I wrote the paper, Prof. Dr. Soraya Heuss-Aßbichler and Dr. Melanie John Stadler reviewed it.
- **Tandon, K.**, Heuss-Aßbichler, S. (2018) Rückgewinnung von Zn und Pb aus Flugasche-Eluaten einer MVA: Erste Ergebnisse. Extended conference contribution (6 pages) submitted, accepted, and presented at the conference Recy-DepoTech, 07. - 09. November 2018.
    - The results are based on the publication in Minerals 2018. Some paragraphs presented in this thesis in chapter 3.2 (the Specific Product Oriented Precipitation (SPOP)) are taken from this publication.
    - I wrote the conference paper and gave the oral presentation; Prof. Dr. Soraya Heuss-Aßbichler reviewed it.
- **Tandon, K.**, Heuss-Aßbichler, S. (2021) Fly ash from municipal solid waste Incineration - from industrial residue to resource for zinc. Chapter in Book: Industrial Wastes – Characterization, Modification, and Application of industrial residues.
  Submitted: August 2020; accepted: September 2020; published: 23 August 2021.
    - Chapters 1 (introduction), 2 (municipal solid waste incineration), 3 (state of the art), and 6 (conclusion and outlook) contain parts of this book chapter.
    - I wrote the book chapter, Prof. Dr. Soraya Heuss-Aßbichler reviewed it.

- **Tandon, K.**, Heuss-Aßbichler, S. (2021) Direct precipitation of ZnO from saline aqueous solutions – an innovative and low-cost method to recover Zn from municipal solid waste incineration fly ash. Waste management. Submitted: 18.01.2022.
    - I planned and conducted the experiments and analyses with support from Katharina Engels and Andreas Appel as student assistants. I discussed and interpreted the data together with Prof. Dr. Soraya Heuss-Aßbichler. I wrote the paper, Prof. Dr. Soraya Heuss-Aßbichler reviewed it.
    - Parts of the publication are used in chapters 1 (introduction), 3.3 (relevant Zn-phases in Cl-rich solutions), and 4 (material and methods), and the content of the paper is presented in chapter 5.2 of this thesis.

1. Introduction

Municipal solid waste (MSW) and the way it is treated reflect the history of human development and its habits and customs (Keller 2009; Heuss-Aßbichler and Rettenberger 2016). Waste is generated daily all over the world, and therefore its treatment was essential from the very beginning (Keller 2009). Archaeologists can draw conclusions about the culture and technology of a particular society from the composition of the waste or the absence of certain components in it (Chandler et al. 1997; Heuss-Aßbichler and Rettenberger 2016). In the 14th and 15th centuries, the disposal of waste dumped in open passageways was an unresolved problem in rapidly growing cities. It became essential in the 19th century when repeated epidemics and diseases of industrialized societies made improving public health increasingly urgent. Thus, in addition to the construction of water treatment and sewage systems, the need for the appropriate handling of waste was seen as an imperative (Geels and Schot 2007; Wilson et al. 2016; Makarichi et al. 2018).

A significant change occurred after the Second World War. With the economic boom and technological progress, the rapidly growing population consumed steadily more, and in consequence, the volume of waste increased enormously (Keller 2009; Makarichi et al. 2018). On the one hand, the demand for new landfill sites raised. On the other hand, the resistance of the population against new landfills grew. To protect the environment and the population, many legislations were introduced (Keller 2009). The waste hierarchy (3R: reduce, reuse, recycle) and the waste directive were adopted to reduce the waste volume and to ensure the safety of the environment and health through proper treatment of waste (EU 2008; Schulze 2019). In the last years, the security of resource supply and thus recovery of valuable elements from waste has become increasingly important. In 2015, the agenda 2030 and the 17 sustainable development goals (SDGs) were adopted as a transnational guideline to sustainability (United Nations 2015). A key aspect of the SDGs is the realization of sustainable development by taking into account economic, social and environmental aspects. Waste management is no longer just a question of providing disposal security and pollution control. It is regarded as essential for fostering a circular economy, as the recovery of raw materials from waste should contribute to a sustainable future (EU 2008; Pinasseau et al. 2018). However, this change is a long and complex process. In Germany, one of the pioneer countries in recycling (Bing et al. 2016), only 14 % of the raw materials used originate from recycling processes (Schneidewind 2018). In comparison, 9 % of the global economy is circular (PACE 2019).

Treatment of the residues after incineration reflects the changing needs of modern society. Waste incineration was introduced at the end of the 1880s, primarily for hygienic reasons. The significant reduction in the volume of waste was also swiftly perceived as a major advantage of incineration (Heuss-Aßbichler and Rettenberger 2016; Makarichi et al. 2018). However, the stench and air pollution

caused by the incineration at that time were extreme, resulting in high resistance of the population to incineration (Keller 2009). Another disadvantage was the low calorific value of the waste. At the beginning of the 20th century, it consisted of 60 % ash, 20 – 25 % organic waste, and only small amounts of paper, paperboard, glass, and metals (Keller 2009). Despite the poor calorific value, initial attempts were made to recover the heat released during combustion (Chandler et al. 1997; Makarichi et al. 2018). Due to high operation costs, recurring technical issues, and other reasons, waste incineration was not widespread in many European cities until the middle of the 20th century (Keller 2009). The construction of MSWI plants was promoted to cope with the increased waste volume. Changing lifestyles led to a change in the composition of waste. The growing proportion of plastics in waste and the resulting increase in the calorific value made heat recovery more attractive (Chandler et al. 1997; Keller 2009; Makarichi et al. 2018), and various types of waste-to-energy power plants were constructed (Paraskevi et al. 2016). The population´s acceptance was achieved by developing a sophisticated air pollution control system for all MSWI plants (Chandler et al. 1997; Heuss-Aßbichler and Rettenberger 2016; Makarichi et al. 2018).

At the same time, more attention was paid to the residues after waste incineration – bottom ash, boiler ash, fly ash, and the remains from air pollution control – since, against initial expectations, the residues are not inert materials. They all contain a considerable amount of heavy metals, salts, and other pollutants, that are harmful to human health and the environment (e.g., Chandler et al. 1997; Sabbas et al. 2003; Sager 2007). Studies also showed that fresh bottom ashes could produce heat (Speiser et al. 2001) and release H_2 (Heuss-Aßbichler et al. 2010). First concepts about the utilization of MSWI residues, mainly of the bottom ash, were developed. In general, after quenching the hot bottom ash with water, separation and recycling of the non-ferrous and ferrous metals occur (Lechner et al. 2010; Muchová 2010; Bunge 2014). Depending on the region, the remains of this process are landfilled or used as backfill or road construction material. At the same time, alternatives to the use of bottom ash were sought. Because of its similarity to gravel, it is partly applied as a substitute for construction materials or as an additive in the cement industry (e.g., Müller and Rübner 2006), while only a few applications are established for fly ash and air pollution control (APC) residues. Fly ashes are mainly disposed of in landfills for hazardous waste because of their toxicity and easily soluble components. Among others, it contains heavy metals, with Zn being significantly enriched. The disposal of fly ash or backfilling underground leads to the loss of the valuable resources it contains.

Zn is an essential element for living organisms, and a deficiency harms the biological function of organisms. However, high concentrations of Zn are harmful to health, causing vomiting, sickness, and diarrhea (Nordberg et al. 2007). Zn is also the fourth most common metal in use. It is applied in enameling and coating processes, construction work, batteries, and medicine, to name a few areas of application. This means that an ever-increasing amount of Zn will be required with time.

In the future, the limited availability of resources will lead to increased mining of low-concentrated ores, which dramatically increases the production costs (Sverdrup et al. 2019). According to estimations, the Zn content in ores will decrease by approx. 1 % over the next decade (Schulze 2016). On the one hand, the decline in the share of valuable by-products such as silver and, on the other hand, the increase in mining costs must be considered (Schulze 2016). Therefore, the use of fly ash from waste incineration as an anthropogenic resource and the associated improved waste management towards a circular economy is gaining importance. It would benefit the environment, the climate, and the economy (Bourguignon 2018).

There are several methods to treat fly ash. One example is the extraction of heavy metals by acidic leaching, e.g., by FLUWA (acidic fly ash washing) (Schlumberger et al. 2007; Weibel et al. 2017). This method has been refined to extract most heavy metals from fly ash efficiently. With this process, easily soluble salt components are also concentrated in the solution. The usual treatment of such eluates with milk of lime leads to a slurry of heavy metal- and salt-rich hydroxides. The high concentration of Cl in this sludge makes recovery of the heavy metals impossible, as it contributes to the corrosion of the treatment facilities. Therefore, these sludges must be disposed of as hazardous waste. Only a few processes focus on the recovery of metals like Zn from such eluates. FLUREC (fly ash recycling) is one example. It is a novel but complex process leading to zinc recovery as a high-grade metal from MSWI fly ash after FLUWA. Huber et al. (2018) evaluated the FLUREC process compared to various other treatment and disposal methods for MSWI fly ash, including the use of life cycle assessment (LCA). They concluded that the FLUREC-process has the lowest environmental impact. However, at the current raw material prices for Zn, it is only economically feasible if the concentration of Zn in MSWI fly ash is above 40000 mg/kg Zn (Huber et al. 2018). This highlights the importance of a low energy and low-cost process, crucial for a sustainable and viable process to recover Zn as a resource from the metals enriched solution.

An innovative method could be the “Specific Product-Oriented Precipitation” (SPOP) of heavy metals. It was successfully used to recover heavy metals from industrial wastewater and thus offers a promising alternative to the usual treatment with milk of lime. This novel concept makes it possible to directly control phase formation by adjusting parameters such as concentration, temperature, pH, and optionally Fe-addition, resulting in the concentration of metals in the precipitates. Using SPOP, John et al. (2016d) succeeded in obtaining Zn from SO_4-rich solutions as a single-phase in the form of nanocrystalline ZnO particles, without Fe addition. Depending on the experimental parameters, the authors achieved removal efficiencies of 99.99 % for Zn under optimal conditions. However, there is no study regarding the precipitation of Zn as ZnO from Cl-rich solutions as available after FLUWA. Therefore, the question arises whether it is possible to optimize the SPOP process to treat MSWI fly

ash to recover Zn as a resource and thus develop an attractive alternative to treatment with milk of lime or energy-intensive recycling methods such as FLUREC.

This thesis aims to investigate the applicability of SPOP in highly saline solutions to (a) develop an SPOP-based process to precipitate Zn as ZnO from Cl-rich solutions, (b) determine the optimal conditions for the precipitation of ZnO in a model system, and (c) test the transferability of the results in the model system to real wastewater from MSWI.

This thesis is organized in the following way: in the beginning, the MSWI and the residues obtained after incineration are introduced. Then, chapter 2 gives an overview of treatment and utilization methods for fly ash and its resource potential with a focus on Zn. Chapter 3 covers the state-of-the-art recovery methods for Zn from MSWI fly ash and describes the SPOP process in more detail. The contents of these two chapters were published in the book “Industrial Waste” (Tandon and Heuss-Aßbichler 2021a). In Subchapter 3.3, the Zn phases that are stable in Cl-rich media are presented. The material and methods used in this thesis, including various real wastewaters from MSWI fly ash after FLUWA from Germany and Switzerland, are the subject of chapter 4.

The central part of the thesis, chapter 5, consists of four sections. The contents of two sections have already been published: The core results of section 5.1 are published in a peer-reviewed journal (Tandon et al. 2018), and that of section 5.2. are submitted (Tandon and Heuss-Aßbichler 2021b). These contributions have been adapted to a uniform chapter structure: At the beginning of every section, the purpose, scope, and nomenclature are described. Next, the experimental series are presented. The last part of every section provides the results and their discussion.

In total, seven different experiment sets are presented, continuously numbered from Set 1 - Set 7. subchapters 5.1, 5.2, and 5.3. cover laboratory experiments in a model system and subchapter 5.4 describes experiments with real wastewater. In section 5.1, the result of a systematic investigation addresses the phases that are stable at room temperature in saline aqueous solution (AQ) and what effect another element, such as Pb, has on the precipitation of phases. The two methods developed in this thesis for ZnO precipitation from Cl-rich solutions are presented in subchapters 5.2. (direct formation) and 5.3 (formation through aging). These two processes have been filed for patenting. The last section of chapter 5 (section 5.4) shows the transferability of the process developed in the model system to real wastewater from MSWI. In the final chapter 6, the core results of this thesis are summarized, advice for future research is given, and the following steps to scale up the developed SPOP process are shown. In addition, new areas of application are presented, where the processes developed in this thesis can potentially be applied.

2. Municipal solid waste incineration – fly ash as a potential resource for zinc?

2.1. Composition of municipal solid waste (MSW)

„[T]he world is on a trajectory where waste generation will drastically outpace population growth by more than double by 2050. Although we are seeing improvements and innovations in solid waste management globally, it is a complex issue and one that we need to take urgent action on." (Silpa et al. 2018)

It is expected that waste generation will increase from 2.02 billion in 2016 to 3.4 billion tons in 2050. Therefore, various studies highlight the importance of environmentally sound waste treatment on a global scale (e.g., Silpa et al. 2018). Low-income countries, where only 5 % of the world's waste is currently produced (Silpa et al. 2018), will contribute more and more to the fast-growing waste come up due to increasing wealth, urbanization, and population growth (Wilson et al. 2016; Silpa et al. 2018). The German Advisory Council on Global Change defines the 21st century to be the century of cities. It estimates that by 2050, around two-thirds of the worldwide population will live in cities (WBGU - German Advisory Council on Global Change 2016). Especially in these urban areas, tremendous amounts of municipal solid waste are generated every year. Main producers are households, including commercial wastes.

In general, waste is a very inhomogeneous material and can consist of paper, paperboard, plastics, glass, non-ferrous metals, iron, food, garden waste, rubber, leather, textiles, various composite materials, mineral wastes, and others (Bunge 2014; Neuwahl et al. 2019; Eurostat 2021) changing from day to day and from season to season (Abanades et al. 2002). The composition also depends strongly on the income level, as can be seen in Figure 2.1.

In lower to middle-income countries, the proportion of food and green waste with 50 vol.-% is by far the highest. Although the total amount of organic waste is more or less the same in all countries, the percentage in high-income countries is comparably lower due to a higher proportion of plastics and other inorganic wastes (Silpa et al. 2018). The higher the income level, the more recyclable materials (paper, cardboard, plastic, glass, metal) are in the waste, with a maximum of 50 % in high-income countries.

During the last decades, waste prevention legislations (waste directive and waste hierarchy) were introduced, and a sophisticated waste collection system helped to decrease the amount of waste that finally has to be treated. In the last 20 years, incineration has been accepted in the industrial nations as an effective contribution to waste management, including energy recovery during the thermal treatment of waste. The composition of the waste as an extremely heterogeneous material influences the composition of the residues after incineration.

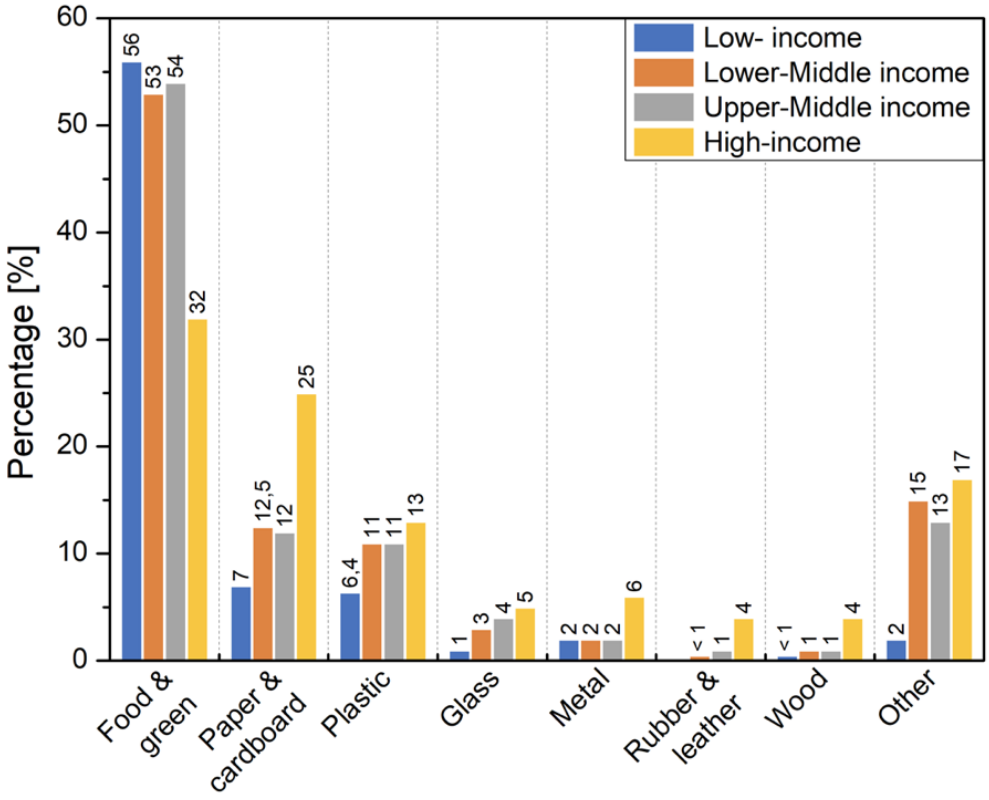

Figure 2.1: Global waste composition in dependence of income level of countries in 2016, after Silpa et al. (2018).

2.2. Principle of MSW incineration plant and types of MSWI residues

The incineration process reduces the mass and the volume by 70 wt.-% and 90 vol.-%, respectively (Hjelmar 1996; Abanades et al. 2002; Pinasseau et al. 2018; Neuwahl et al. 2019). Figure 2.2 shows a general scheme of a municipal solid waste incineration plant. Waste is unloaded in the waste bunker, homogenized, and stored for several days to decrease the moisture, varying between 20 – 30 vol.-%. Afterward, it is fed into the combustion chamber by a crane. The incineration temperature must be above 850 °C in the combustion chamber for at least 2 seconds to completely destroy persistent organic pollutants (POP.s), e.g., dioxins (polychlorinated dibenzo-p-dioxins, PCDDs) and furans (polychlorinated dibenzofurans, PDCFs) (Youcai 2017). The main products of waste incineration are bottom ash, boiler ash, and residues of the flue gas treatment. Before the flue gas is released into the atmosphere, hazardous components, and pollutants such as ash and dust particles, acid gases (e.g., HCl, HF, SO_X, NO_X) as well as organic pollutants (dioxins, furans, CO, hydrocarbon) are removed. A sophisticated technology recovers the heat transported with the exhaust gases as energy. Fly ash and flue gas treatment residues are considered as pollutant sink. They are classified as hazardous waste due to their toxic components.

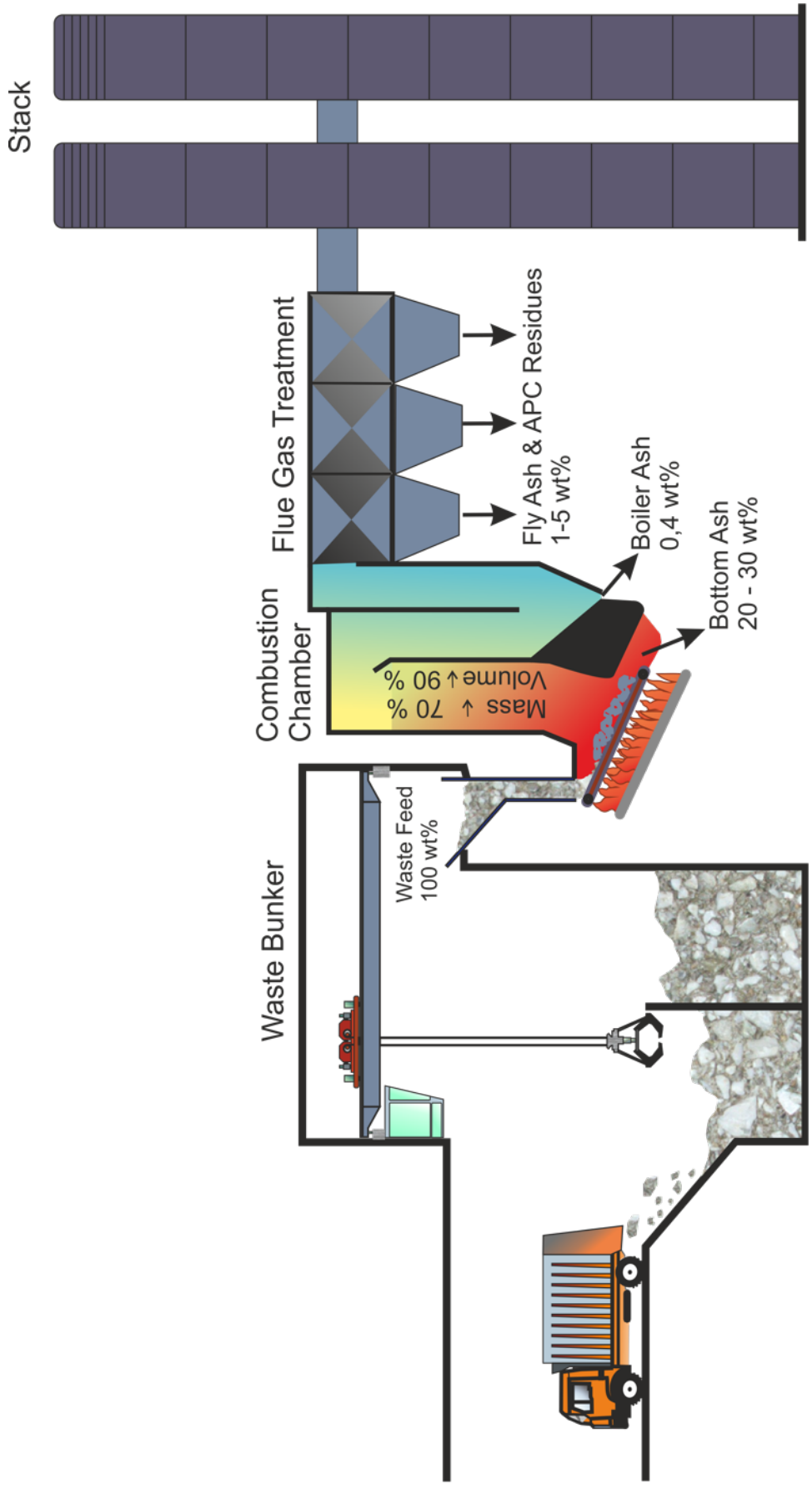

Figure 2.2: General scheme of a municipal solid waste incineration plant.

Bottom ash with 20 – 30 wt.-% is the main product of the MSW incineration process (Belevi and Moench 2000; Sabbas et al. 2003; Youcai 2017; Yin et al. 2018; Neuwahl et al. 2019) and is collected in a quenching/cooling tank after the combustion chamber (Sabbas et al. 2003). The main components of the bottom ash are vitrified particles and partly coarse-grained materials, which pass the combustion chamber without any changes, e.g., glass, ceramics, stones, metals, and unburnt organic matter. Heavy metals are especially enriched in the finer fraction of the bottom ash (Bunge 2014; Youcai 2017).

Boiler ash is only partially entrained with the flue gas and remains in the boiler. It represents 0.4 wt.-% of the original waste input and is usually treated together with the fly ash (Belevi and Moench 2000; Neuwahl et al. 2019).

Residues of the flue gas treatment (FGT) consist primarily of pollutants in the gaseous phase, which are trapped in solid particles after the cleaning process, including fly ash and air pollution control (APC) residues. Accordingly, these residues are enriched in heavy metals, salts, and organic micro-pollutants (Sabbas et al. 2003).

Fly ash makes up about 1 – 5 wt.-% of the initial waste input (Belevi and Moench 2000; Chang and Wey 2006; Youcai 2017; Neuwahl et al. 2019) and is smaller in size than bottom ash. The dust and ash particles generally consist of amorphous phases (silicate glass), oxides, and chlorides that are trapped by the flue gas and pass the heat recovery units (Sabbas et al. 2003), as shown in Figure 2.2. Volatile heavy metals are especially enriched in fly ash due to their low boiling point (Bogush et al. 2015). They either condense on the surface of the ash particles or form new, non-volatile species during cooling on the way from the combustion chamber to the flue gas treatment unit (Evans and Williams 2000; Ferreira et al. 2003; Sabbas et al. 2003; Luo et al. 2019). In the first stage of the gas cleaning process, the fly ash is removed by bag filters or electrostatic precipitators.

APC residues are generated in the next stage during the flue gas treatment of the remaining acid gases and organic pollutants (Neuwahl et al. 2019). Basically, there are two different techniques: (1) dry and semi-dry or (2) wet FGT. (1) In **dry** and **semi-dry** FGT, sorbents are fed into the flue gas stream to compensate for the acidity introduced by the gases. During dry FGT, coke, hydrated lime, or sodium bicarbonate with high porosity are injected as powder. In the case of semi-dry FGT, the sorbent is an aqueous solution, i.e., milk of lime (Neuwahl et al. 2019). By spraying it into the flue gas stream, the solution evaporates. Semi-dry methods are usually more efficient because the addition of the solution is easier to control, and therefore less excess of alkaline reagents is needed, which decreases the total volume of the APC residue. In both cases, the resulting residues are dry. (2) The **wet** treatment process differs significantly. Flue gas is injected into a scrubber that usually contains water. There, the acid gases dissolve, and a strongly acidic solution results (pH 0 – 1), especially enriched in Cl.

For efficient flue gas cleaning, parts of the scrubber water must be constantly exchanged, and the very acidic wastewater has to be treated. Usual methods are either neutralizing the wastewater with an alkaline agent (i.e., milk of lime) and disposal of the solid remains or spraying the wastewater back into the flue gas for evaporation in order to avoid wastewater treatment (Neuwahl et al. 2019).

The distribution (fractionation) of elements, and in particular the heavy metals in the respective incineration products, depend on various parameters, which are (Neuwahl et al. 2019):

- combustion conditions (temperature, oxygen supply, furnace type, residence time)
- Cl-concentration in the waste
- flue-gas treatment (FGT) system

One main factor for the element distribution is the furnace technology, as it affects temperature, oxygen supply, and residence time in the combustion chamber.

In general, the waste composition determines the total sum of elements that can be found in the respective residues after the incineration process. Material flow analyses of the individual MSWI components were performed, focusing on the heavy metals (e.g., Abanades et al. 2002; Ferreira et al. 2003; Youcai 2017). Belevi and Moench (2000) conducted a detailed study on this speciation. Figure 2.3 shows that about 79 wt.-% of the initial waste input is transferred to the exhaust gas, 0.36 wt.-% to the boiler ash, 1.9 wt.-% to the FGT-residues, and about 19 wt.-% to the bottom ash.

Looking at the fractionation of heavy metals between the different types of MSWI residues, the major part (> 80 wt.-%) of Co, Cu, Cr, Fe, Mn, Mo, and Ni, in addition to critical elements Ba, Li, P, and Ti, is concentrated in the bottom ash. It also contains the main part (> 50 wt.-%) of As, and only minor parts (< 25 wt.-%) of Cd, Pb, Sb, Sn, and Zn. The rest of these elements are distributed over the boiler ash and FGT-residues. It is noteworthy that the main fractions of the heavy metals (Cd, Sb, Sn, Zn) and the halogens (Br, Cl, F), including S, are concentrated in the FGT residues. In contrast, Pb and Cd are more evenly distributed over all types of MSWI residues. The highly toxic and volatile Hg is mainly found in the exhaust gas and the FGT residues. In the case of wet FGT, it is treated separately due to its hazardousness.

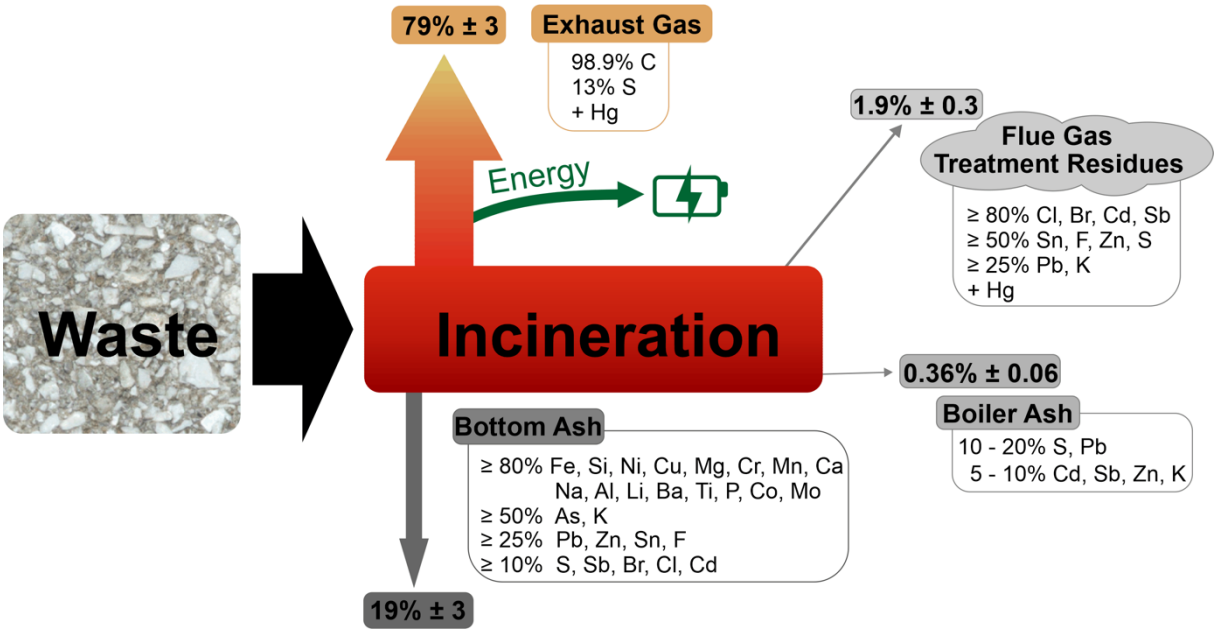

Figure 2.3: Mass transfer and fractionation of various elements in the exhaust gas, flue gas treatment residues, boiler, and bottom ash after waste incineration in wt.-%. The figure is based on numbers from Belevi and Moench (2000).

As shown in Figure 2.3, highly volatile elements are enriched in the fly ash, while less volatile elements are accumulated in the bottom ash (Youcai 2017): with increasing furnace temperature, the concentration of Zn, Cu, Cd, Pb, and Sn in the flue gas treatment residues rises (Belevi and Moench 2000; Youcai 2017), depending on the melting and boiling point of the respective metal (Me)-compounds. Decreasing or low oxygen supply during incineration leads to an enrichment of Sn and As and depletion of Zn, Cu, Mo, and Sb in the fly ash. The oxidation conditions have only little effect on the fractionation of Cd and Pb (Belevi and Moench 2000).

The concentration of Cl in the waste has an enormous impact on the fractionation of Zn, Cu, Cd, Pb, Sn, Mo, Sb, As; increasing Cl contents promote the accumulation of these metals in the fly ash (Belevi and Moench 2000). This can be explained by the low boiling point of the respective Me-chlorides (Youcai et al. 2002; Ferreira et al. 2003) and hence, a higher vapor pressure compared to the Me-oxides (Abanades et al. 2002). The FGT system determines the distribution of the heavy metals in the flue gas cleaning residues.

2.3. Treatment and utilization of MSWI fly ash

MSWI fly ash is considered the most hazardous fraction of the residues after the combustion process because of its high content of potentially toxic pollutants such as heavy metals, easily soluble salts, and POPs (Youcai et al. 2002; Zacco et al. 2014; Quina et al. 2018). According to the European Waste Framework Directive 2008/98/EC (EU 2008) (article 7, list of waste), it is classified as hazardous,

marked by waste codes EWC 19 01 13* (fly ash containing hazardous substances) apart from EWC 19 01 14 (fly ash other than those mentioned in 19 01 13*).

In the course of time, various methods have been developed and proposed for the processing and/or treatment of MSWI fly ash. In principle, these techniques can be distinguished according to their objective: a) treatment and/or disposal, b) reuse in new products.

a) Treatment and disposal

Safe disposal of fly ash and APC residues is a priority in order to prevent the dissemination of pollutants into the environment, as salts together with heavy metals, mainly Pb and Zn, can be leached upon contact with water (Quina et al. 2008b). The solubility of heavy metals is dependent on pH; due to the amphoteric properties of the metals, the concentrations may increase strongly at both high and low pH values (Benassi et al. 2016). Fly ash is mostly filled into "big bags" and stored, e.g., in parts of salt mines where backfilling is required (Huber et al. 2018), as shown in Figure 2.4, or underground caverns to avoid contact with water and for stabilization (Quina et al. 2018).

Figure 2.4: Utilization of FGT residues stored in big bags for stabilization in parts of salt mines where backfilling is required.

Various treatment methods have been developed to fix the pollutants before landfilling to minimize the quantity of hazardous waste and thus reduce the disposal costs (Zacco et al. 2014; Youcai 2017). The most used method worldwide for the entrapment of heavy metals in MSWI fly ash is the stabilization/solidification (S/S) process (Bontempi et al. 2010; Zacco et al. 2014; Benassi et al. 2016; Youcai 2017; Neuwahl et al. 2019). This process utilizes chemical or solidifying agents such as cements, iron oxides, phosphates, silicates, or organic acids to fix the pollutants in the matrix (Youcai 2017). Portland cement is the most commonly used binder. In this case, the fly ash is mixed with cement and water. This increases the weight and volume of the residue (Quina et al. 2008b) that finally has to be disposed of.

By washing the fly ash before S/S processes with neutral or basic water and thus removing soluble salts containing heavy metals, the long-time stability of the cement can be increased, and its toxicity reduced (Quina et al. 2008b). This effect is further enhanced by washing the fly ash with acids, as this hydrometallurgical process promotes the dissolution of most metals in the fly ash (Quina et al. 2009). Another possibility for treating MSWI fly ashes are thermal methods such as sintering, melting, or vitrification by using additives; all these methods have a high energy demand (Quina et al. 2018).

b) Use as product phases

Fly ash from municipal solid waste can be exploited either by using it directly or by improving some material specifications to manufacture a product, (e.g., Gianoncelli et al. 2013). Quina et al. (2018) presented in their paper the following possible applications of MSWI fly ash: ceramic materials, glass-ceramics, cement, secondary building materials, epoxy composites, zeolite-like material, adsorbent, and thermal energy storage materials.

Various methods have been proposed to treat fly ash, such as separation techniques (based on magnetic properties, size, or density), washing, carbonation, or stabilization, to improve the technical properties of fly ash as a product or additive, and to reduce the hazard potential. Washing, for example, removes highly soluble heavy metals with the salts. In most cases, however, fly ash is added to the actual raw materials only in small quantities in order to avoid a negative influence on the chemical or mechanical properties. For example, only 1 – 10 wt.-% fly ash can be added for the production of ceramics (Quina et al. 2014b, 2014a; Jordan et al. 2015; Kizinievich et al. 2019). Even an addition of 5 wt.-% fly ash has a significant effect on the properties of the ceramics, among others, the heavy metals contained in the ashes can be released to such an extent that local regulations cannot be met (Kizinievich et al. 2019). The situation is similar in cement production. Between 5 – 15 wt.-% (Wang et al. 2015) and 5 – 35 % of the dry mass of the fly ashes (Bogush et al. 2020), washed and unwashed, were used for clinker production. With increasing addition of fly ash, the mechanical properties decrease dramatically. Substitution of 35 wt.-% clinker with fly ash lead to a negligible compressive strength of the cement after 28 days (Bogush et al. 2020). Moreover, it is not entirely clear to what extent the heavy metals can be released through contact with water. A similar observation was made in relation to the use of fly ash in brick production, where only 2.5 – 7.5 wt.-% ash was added. With the increasing amount of added ash, the H_2O absorption in bricks increases, too, and the compressive strength decreases.

2.4. Fly ash – an anthropogenic resource for Zn?

The previous section shows that fly ashes are mainly disposed of in landfills for hazardous waste because of their toxicity and soluble components. In consequence, the metals they contain are lost as a resource. Recently, waste is increasingly discussed as a potential source for valuable compounds. Especially Zn is enriched in the fly ashes. Table 2.1 shows the Zn-concentration in mg/kg of MSWI fly ash from different countries. It shows that the Zn-concentration in MSWI fly ash varies significantly, from 3000 mg/kg up to 70000 mg/kg Zn. The values differ even within a country. The Ca-content can be by a factor of 10 higher than Zn, varying between 58000 mg/kg and 410000 mg/kg Ca. High Ca contents are caused by the addition of milk of lime during wet or semi-dry/dry FGT.

Table 2.1: Zn- and Ca-concentrations of selected literature in mg/kg. It is marked if Ca was added during the FGT (yes, no, no Info). The values were differentiated by country.

Country	Zn [mg/kg]	Ca [mg/kg]	Ca-Addition	Reference
Denmark	31700	181000	no	Hyks et al. (2009)
	9100	331000	yes	
Italy	13293	58409	yes	Benassi et al. (2016)
Portugal	5826	243300	yes	Quina et al. (2008a)
	4308	287300	yes	
	6367	349600	yes	
	4939	361600	yes	
Sweden	5500	315000	yes	Karlfeldt Fedje et al. (2012)
	3300	410000	yes	
	5800	360000	yes	
	26000	210000	yes	
	55000	120000	no	
Switzerland	22000	184000	no	Belevi and Moench (2000)
	26770	191500	no	Weibel et al. (2017)
	48190	168900	no	
	65170	151150	no	
	71190	143814	no	Haberl et al. (2018)
	69345	140266	no	
	51940	176698	no	
	61348	170870	no	
	62182	164105	no	
Taiwan	9620	337660	no info	Huang and Chuieh (2015)

Table 2.1 (continued): Zn- and Ca-concentrations of selected literature in mg/kg. It is marked if Ca was added during the FGT (yes, no, no Info). The values were differentiated by country.

Country	Zn [mg/kg]	Ca [mg/kg]	Ca-Addition	Reference
UK	5800	260000	yes	Bogush et al. (2015)
	7300	270000	yes	
	2600	224000	yes	
	7300	240000	yes	
	7100	270000	yes	
	7100	240000	yes	
	6600	230000	yes	
	3700	320000	Yes	
Germany	49100	124100	no info	Bayuseno et al. (2009)
	39341	164602	no	Haberl et al. (2018)
	28131	128259	no	
	33955	152039	no	
	9831	231367	no	
	8560	302880	yes	
	13126	110138	no	

The correlation between Zn-concentrations in fly ashes and Ca-concentration shows Figure 2.5, based on the data listed in Table 2.1. Pure fly ash is generally enriched in Zn (> 20000 mg/kg Zn). In general, the Ca-concentration – except for one sample – is always < 200000 mg/kg Ca. The effect of adding Ca as milk of lime during semi-dry/dry treatment is evident as it leads to the opposite trend: in this case, the Zn concentrations are generally low (< 10000 mg/kg Zn), while the samples are enriched in Ca (> 200000 mg/kg Ca). The dilution leads not only to a decrease of Zn content but also of all other heavy metals contained in the MSWI fly ash, a trend which is also observed during a long-time study of Haberl et al. (2018).

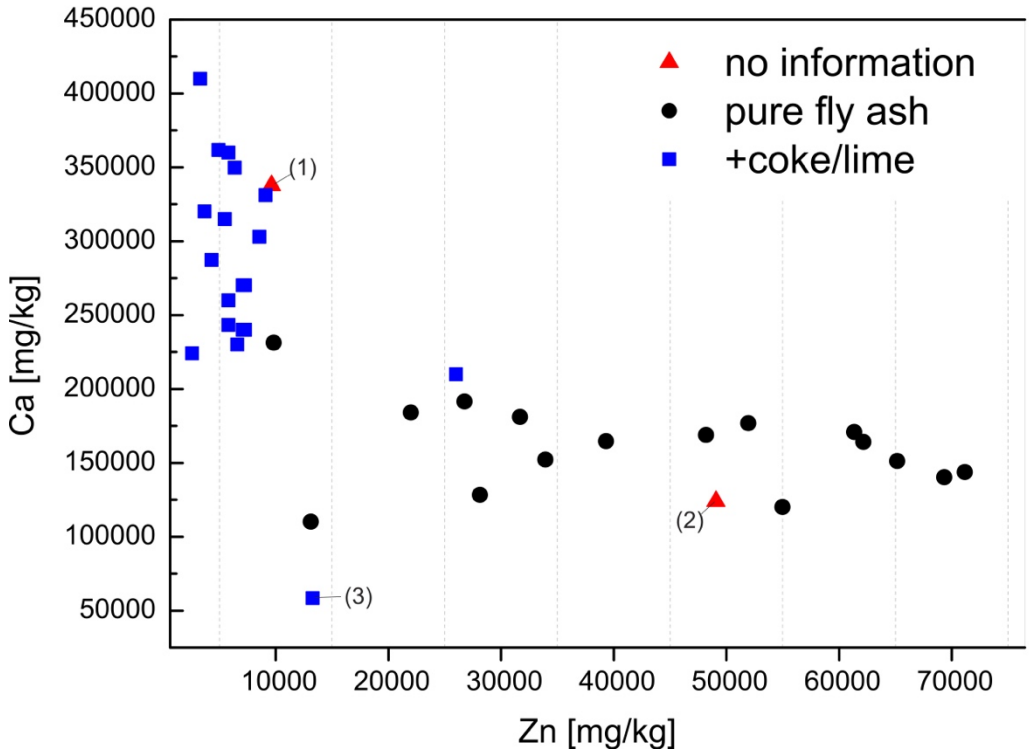

Figure 2.5: Zinc-concentration as a function of Calcium-concentration in mg/kg in MSWI fly ash in various countries. The symbols indicate whether milk of lime was added (blue square) during FGT or not (grey circle) or if no information was available (red triangle). Data is based on the literature listed in Table 2.1.

In two cases (red triangles (1) and (2) in Figure 2.5), no information was given by the authors regarding the treatment process. However, based on the Ca concentration, it can be clearly assigned that sample (1) represents an example of dry/semi-dry treatment and sample (2) pure fly ash. The most significant deviation from this trend shows sample (3), where Ca was added according to the authors (Quina et al. 2008b). The relatively low values of Zn and Ca are possibly the effect of incomplete digestion of the sample and/or choice of the analysis method. Insufficient combustion conditions during incineration can be excluded because of the very low Ca content of the sample. In total, these analyses show that the concentration of heavy metals is high enough to be regarded as a potential source for Zn.

3. State of the art

3.1. Recovery of metals from MSWI fly ash

Various concepts were developed with the aim to treat and utilize MSWI residues, in particular focused on bottom ash (e.g., Dou et al. 2017). However, fly ashes from MSWI should also be taken into account because of their high zinc content, which may reach the grade of natural ore deposits (Richards 2019). In recent decades, increased research has been conducted towards how elements from MSWI fly ash can be recovered. In a review article, Quina et al. (2018) stated that not only the recovery of Zn, but also Cu, other (precious) metals, P, and rare earth elements are in the focus of various treatment processes.

As was shown before, MSWI fly ash is very inhomogeneous, and the composition varies significantly day by day and season by season (see chapter 2.4.). Therefore, processes for the potential recovery of zinc from fly ash have to be very robust to handle the aforementioned fluctuations in chemistry. In the following sections, two methods are presented, focusing on the leaching of metals from MSWI fly ash (e.g., FLUWA, section 3.1.1), and recovering Zn from MSWI fly ash (e.g., FLUREC, section 3.1.2).

3.1.1. Leaching of metals from MSWI fly ash

There are two different types of studies that deal with the “accessibility” of heavy metals in fly ash: Most of the studies were carried out to test the long-term stability of the fly ashes in contact with water or acids, with the aim to predict the potential risk to the environment and thus making recommendations for avoiding environmental pollution (e.g., Quina et al. 2009; Ni et al. 2017).

Recent studies focus on optimizing the extraction of metals from fly ash with the aim to recover the metals contained by hydrometallurgical processes (e.g., Karlfeldt Fedje et al. 2010; Tang and Steenari 2015, 2016; Weibel 2017; Luo et al. 2019). In general, the highest leaching rates for heavy metals are obtained by using acids (Karlfeldt Fedje et al. 2010; Tang and Steenari 2016). These processes strongly depend on the extraction conditions, such as the type of acid, the addition of oxidizing agent(s), pH, liquid to solid (L/S) ratio, extraction temperature, and time. For example, Tang and Steenari (2016) achieved a yield of 70 % Cu, 80 % Zn, 93 % Cd, and 35 % Pb under optimal conditions using HCl, pH 2, a L/S ratio of 20, a temperature of 20 °C and 20 h leaching time.

The acidic washing of MSWI fly ash is already in large-scale use in Switzerland since 1997 (Schlumberger 2010; Weibel 2017). This so-called FLUWA process has been further developed over the years and is now state of the art in more than 60 % of waste incineration plants in Switzerland (Weibel 2017; Quina et al. 2018). Prerequisites for the FLUWA process are MSWI plants equipped with a wet FGT system.

In the first step of the process, the alkaline fly ash is mixed with the (Hg depleted) acidic flue-gas-scrub water produced in the wet FGT process and then remains in a three-stage tank cascade for 60 minutes each. Table 3.1 shows a typical elute composition obtained after the FLUWA process (Schlumberger 2010). One parameter to optimize the leaching conditions is the addition of H_2O_2 as an oxidizing agent to increase the yield of all metals, especially of the redox-sensitive metal Cu. Weibel et al. (2018) obtained an optimal yield of 55 % Cu, 68 % Zn, 97 % Cd, and 62 % Pb by using HCl 5 % at pH 2.5, 60 °C and addition of 30 L H_2O_2/t fly ash. The extraction of metals can be further enhanced by a second leaching step using concentrated NaCl-solution (NaCl 300 g/l, pH 3.5, 85 °C), leading to a yield up to 81 % Cu, 78 % Zn, 100 % Cd, and 98 % Pb (Weibel et al. 2018).

Table 3.1: Typical composition of the elute after the FLUWA process. Values after Schlumberger (2010).

Matrix compounds		**Heavy metals**	
Element	**Concentration [mg/l]**	**Element**	**Concentration [mg/l]**
Cl	30000 – 70000	Zn	4000 – 12000
F	200 – 600	Pb	500 – 2000
SO_4	1000 – 5000	Cu	20 – 300
Ca	3000 – 12000	Cd	40 – 200
Mg	500 – 2000	Hg	0.003 – 0.01
		Fe	< 5
		Ni	< 1

The addition of H_2O_2 promotes the oxidation of metals, e.g., Fe^{2+} to Fe^{3+}, and promotes the precipitation of Fe-hydroxide, which can be removed before further treatment (Weibel 2017). The solids in the suspension are then separated from the liquid by using a vacuum-belt-filter, and the filter cake depleted in toxic heavy metals and salts can be treated together with the bottom ash (Quina et al. 2018). After the FLUWA process, the metal(s) in the filtrate are usually neutralized with milk of lime, as a state-of-the-art treatment of heavy metals containing wastewater, which is an easy-to-apply and cheap method (see also Anagnostopoulos and Heuss-Aßbichler 2021).

3.1.2. Hydrometallurgical Zn-recovery from MSWI fly ash

A new process called fly ash recycling (FLUREC) is complimentary for FLUWA and was developed with the aim to recover Zn as a valuable resource. This process was first described by Schlumberger et al. (2007) and optimized over the last years (Weibel 2017). It is now in use on an industrial scale in a waste incineration plant in Zuchwil, Switzerland (Schlumberger et al. 2007). The overarching goal of the FLUREC process is the recovery of Zn as a high-grade metal (SHG, 99.995 % Zn) that can be used as high-quality raw material. The hydrometallurgical process is divided into three steps: 1) cementation, 2) solvent-extraction, and 3) electrolysis.

1) As the first step and in preparation for solvent extraction, all heavy metals except zinc are removed by cementation. Therefore, Zn-powder is added to the metals enriched filtrate after the FLUWA process. Hereby, according to the electrochemical series, all metals which are nobler than zinc are reduced. The dissolution of metallic Zn^0-powder leads to the precipitation of Cu^0, Pb^0, and Cd^0 as cementate (see equation 3.1).

(3.1) $$Cd^{2+}, Pb^{2+}, Cu^{2+} + 3\ Zn^0 \rightarrow Cd^0 \downarrow, Pb^0 \downarrow, Cu^0 \downarrow + 3\ Zn^{2+}$$

The filtered cementate has a high dry substance content (> 60 wt.-%) and can be sent to the smelter. It is of interest due to its high content of Pb^0 (50 – 70 wt.-%) (Schlumberger 2010).

2) The selective extraction of Zn from the solution occurs by a solvent-solvent extraction process in a counter-current mixer-settler setup. A chelating agent forms an organic complex with Zn, which is insoluble in water and strongly pH-dependent. The optimal condition for Zn complexation is pH 2.7 – 3.0 (Schlumberger et al. 2007). Another important parameter is the contact time of the immiscible phases to form these complexes. The smaller the droplets, and hence the higher the contact surface of the two phases, the faster the exchange. However, too small droplets cause a stable suspension which inhibits the next step: the separation of the two liquid phases (Schlumberger et al. 2007). Under optimal conditions, 99.5 % of Zn can be stripped by this process. In the stripped solution, < 25 mg/l Zn remains, which is then treated with milk of lime to meet the local regulations of discharge (Schlumberger 2010). The remains of the organic phase in this solution need to be treated, too.

3) The next step is washing the loaded organic phase to remove impurities that would cause problems during electrolysis. Finally, sulfuric acid (at adjusted pH) is added to re-extract Zn from the organic phase to achieve a concentrated Zn-sulphate solution (> 160000 mg/l Zn). The organic phase is regenerated for the complexing process (2) (Schlumberger 2010; Schlumberger and Bühler 2013). The recovery of Zn is performed by electrolysis using an aluminum cathode and a titanium anode. By applying a DC voltage, SHG zinc is deposited on the aluminum cathode as plates (99.995 % Zn) and H_2-, O_2-, and traces of Cl_2-gas are generated on the anode. These zinc plates can then be mechanically separated from the aluminum cathode and sold. The generated gases are treated in-house. The reaction tank is constantly filled with a Zn-rich solution to compensate for the loss of Zn during electrolysis. Tang and co-workers also recognized the potential of combining leaching and selective extraction of copper and zinc on laboratory (Tang and Steenari 2015) and pilot-scale (Tang et al. 2017). They have developed a method similar to the FLUREC process by first leaching the metals with HCl and then recovering first Cu and then zinc by solvent-extraction.

3.2. The Specific Product-Oriented Precipitation (SPOP)

The Specific Product Oriented Precipitation (SPOP) can be a viable method for the recovery of Zn from MSWI fly ash eluates after applying FLUWA. In contrast to precipitation with lime milk, treating leachate wastewater from MSWI fly ash with an optimized SPOP process can produce residues with a high potential for recycling.

SPOP is a novel concept for the recovery of metals from industrial wastewater. The SPOP process is based on the ferrite process, which was developed in the 1980s primarily to purify laboratory wastewater with low heavy metal contamination (Okuda et al. 1975; Tamaura et al. 1979, 1991). Studies with highly contaminated wastewater having heavy metal concentrations up to 25000 mg/l showed that SPOP is a suitable method to treat these wastewaters successfully (John 2016). Initially, the process was developed for copper. Depending on the experimental setup and parameter settings, Ferrite (solid solution series between Magnetite Fe_3O_4 and Copper-ferrite $CuFe_2O_4$), Delafossite ($CuFeO_2$), Cuprite (CuO_2), Tenorite (CuO), and/or metallic copper (Cu^0) can be precipitated (Heuss-Aßbichler et al. 2016a, 2016b; John 2016; John et al. 2016a, 2016b, 2016c). Thereafter, the method was applied to other SO_4-rich and Cl-poor wastewaters containing various non-ferrous and precious metals (Zn, Ni, Ag, Mn, Pb, Sn, Pd, Au), and the concept was further developed.

The chemical precipitation takes place under consideration of the mineralogy of the residues. The controlling parameters are the concentration of the heavy metals in the wastewater, reaction temperature, Fe^{2+}-addition, alkalization conditions, pH-value, aging conditions, and addition/exclusion of O_2 (John 2016). Various industrial wastewaters have already been successfully treated in laboratories (Heuss-Aßbichler et al. 2016a, 2016b; Huber et al. 2016; John 2016; John et al. 2016c; John et al. 2016d; John et al. 2017; Heuss-Aßbichler and John 2017) and first positive tests were performed with a portable pilot plant (Anagnostopoulos and Heuss-Aßbichler 2021). The metal recovery rates were always very high (> 99.9 %). Optimally, the precipitation products are free of hydroxides, which means a significant reduction of the volume of the precipitates. The solids have the potential to be used directly as a commercial product, or the material can be processed as an anthropogenic resource in recovery facilities. Generally, after the process, the treated wastewaters comply with the regulations for indirect or direct discharge.

3.3. Relevant Zn-phases in Cl-rich solutions

In nature, Zn-phases that contain Cl occur in the oxidized zones of Zn-sulfide deposits and at contact zones of hydrothermal fluids with seawater (Anthony et al. 1997a, 1997b; Nasdala et al. 1998). They may also occur as weathering products on Zn-bearing slags (Anthony et al. 1997c; Hawthorne and Sokolova 2002), or as corrosion products of zinc in marine atmospheres (Almeida et al. 2000).

Hagemann (2012) conducted a very detailed review on the easily soluble heavy metals Zn, Pb, and Cd in saline solutions, identified data gaps in the literature, and complemented these gaps with laboratory experiments. The aim was to better understand the processes occurring when waste dumps or other contaminated sites are in contact with water to assess the potential hazard on the ground- and drinking water resources. Based on the results, he developed a thermodynamic model and derived the stable phases present under saline conditions.

In the system $ZnCl_2$-NaCl-H_2O, at concentrations > 55 wt.-% $ZnCl_2$, $Zn_2(OH)_2Cl_2 \cdot H_2O$ is the stable phase and at lower $ZnCl_2$ concentrations, Simonkolleite $Zn_5(OH)_8Cl_2 \cdot H_2O$ is stable (Hagemann 2012). In the presence of CO_2, Simonkolleite is often observed as a corrosion product in NaCl-rich conditions with high relative humidity and as the weathering product of Zn-bearing slags (Hawthorne and Sokolova 2002), although Hydrozincite $Zn_5(CO_3)_2(OH)_6$ would be the thermodynamic stable phase (Hagemann 2012). Hydrozincite always covered Simonkolleite in these cases, forming a layer that was permeable to Cl and H_2O but not to hydrogen carbonate (Hagemann 2012).

In the System Zn-Cl_2-SO_4-H_2O under atmospheric conditions, basic Zn-Cl sulfates form as corrosion products having OH/Cl/SO_4 ratios ranging from 3:1:2 to 7:1:2 (Hagemann 2012). With sufficient available Na, $NaZn_4(SO_4)(OH)_6Cl \cdot 6H_2O$ is observed, known as Gordaite. Insufficient Na-availability leads to the formation of $Zn_4(SO_4)(OH)_4Cl_2 \cdot 5H_2O$.

All these basic Zn-Cl sulfates have a layered structure and belong to the group of layered hydroxide salts. The most relevant Zn-phases detected in the products of the experiments in this thesis are the layered hydroxide salts Gordaite and Namuwite, as well as Bechererite and Zincite. Therefore, general information about layered hydroxide salts, the relevant minerals, their crystal structure, and the standard synthesis methods of these minerals are presented in the following.

3.3.1. Layered hydroxide salts (LHS)

Layered hydroxide salts (LHS) are part of the layered double hydroxides (LDH). LDH have the unique property that they can contain exchangeable anions and water between the layers, which is why they are also called anionic clays (Rajamathi et al. 2001). In general, the LDH are composed of modified brucite-like layers (Wypych 2004; Arizaga et al. 2007). Figure 3.1 compares the Brucite structure with that of the LDH and LHS. In Brucite (Figure 3.1a), $Mg(OH)_2$, the divalent Mg^{2+}-ions are surrounded by 6 OH^--groups and these structural units are corner-linked to each other, building the octahedral hydroxide layer (Wypych 2004). These two-dimensional, neutrally charged layers are connected by van der Waals forces (Rajamathi et al. 2001; Arizaga et al. 2007).

Layered double hydroxides have the general formula $[M^{2+}_{1-x}M^{3+}_x(OH)_2][A^{n-}]_{x/n} \cdot mH_2O$ (Rajamathi et al. 2001). The anion exchange property in LDH results from the partial isomorphic substitution of the

divalent Me^{2+}-ions by trivalent Me^{3+}-ions, generating a positive charge of the layer (Choy and Park 2004). This positive charge is compensated by incorporating anions and water between the layers, as shown in Figure 3.1b.

The layered hydroxide salts have the general formula $[M^{2+}(OH)_{2-x}][A^{m-}]_{x/m}{\cdot}nH_2O$, where M represents mobile exchangeable bivalent metal-ions such as Cu^{2+}, Zn^{2+}, Ni^{2+}, Co^{2+}, Mn^{2+}, Fe^{2+}, Cd^{2+}, and others and A is for anions, such as Cl^-, NO_3^{2-} and SO_4^{2-} (Arizaga et al. 2007; Stanimirova 2019). In contrast to the LDH, the LHS do not incorporate trivalent Me^{3+}-ions in the octahedra to generate the charging of the layer. Instead, vacancies are present in the octahedral layers that generate the positive charge. This positive charge is compensated by tetrahedrally coordinated divalent cations that are located on top and bottom of the octahedral vacancies, resulting in layers with the general composition $[M^{octa}_{1-x}\,M^{tetra}_{2x}(OH)_2]^{2x+}$ (Figure 3.1c). Anions and water are intercalated between the layers, which are connected by weak electrostatic forces (Wypych 2004; Arizaga et al. 2007). The incorporation of the ions between the layers changes the basal distance while the general structure is maintained (Arizaga et al. 2007).

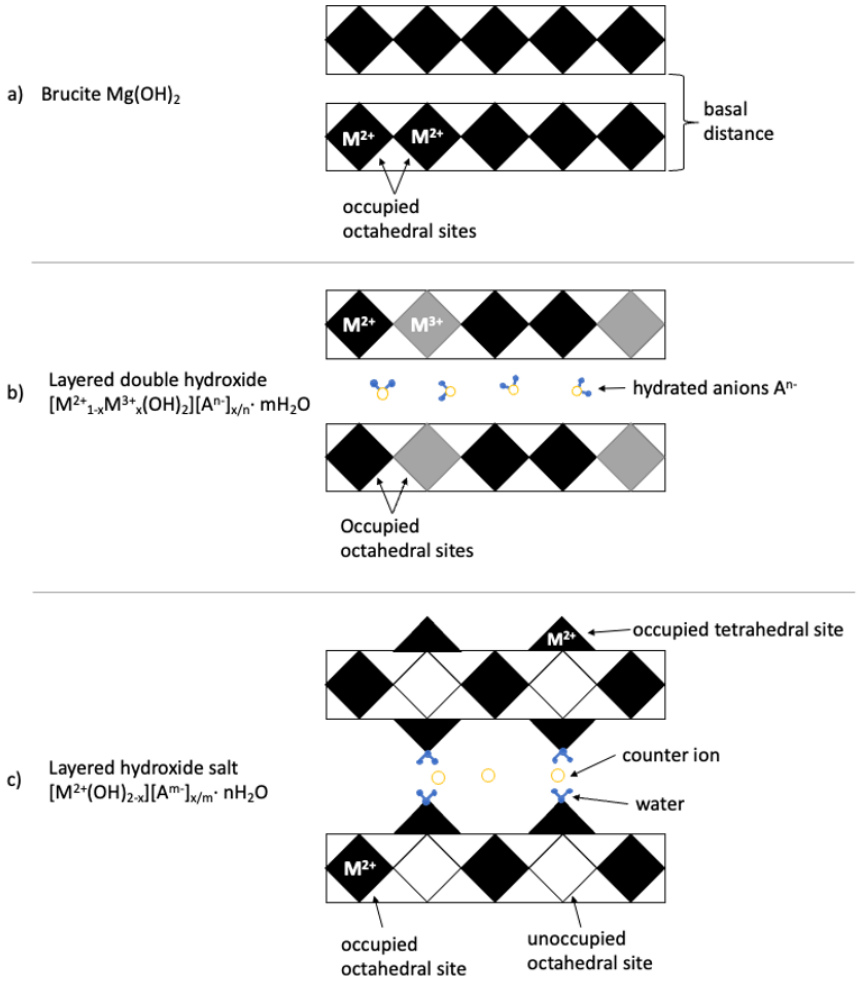

Figure 3.1: Structural features of a) Brucite structure, b) layered double hydroxides (LDH), and c) layered hydroxide salts (LHS).

LHS are usually synthesized by mixing a metal oxide with the corresponding dissolved metal salt. If the bivalent metal ion in the salt and the oxide differs, an LHS with the general formula $[M_{1-y}Me_y(OH)_{2-x}][A^{m-}]_{x/m}\cdot nH_2O$ can form (Arizaga et al. 2007). Other synthesis methods are urea hydrolysis, the controlled precipitation with an alkaline solution, and solid-state reactions involving urea or hydrothermal reactions (Arizaga et al. 2007).

LHS are easily affected by environmental changes, such as changes in pH, Eh, the concentration of the solution, component ratio, impurities, and other factors. Such changes can lead to decomposition of the LHS, or they can be transformed into other LHS (Stanimirova 2019), e.g., in the presence of Me-ions (Wang et al. 2019). A feature of the LHS are the application as ion-exchangers for the retention of selective anions or incorporating cations, as additives in polymers, as precursors for metal oxides, as anti-corrosives, or as matrices for catalysis (Arizaga et al. 2007).

3.3.2. Layered Zinc hydroxide salts (LHS)

Zinc hydroxy sulfate minerals belong to the LHS and were already studied regarding their complex structural features (Groat 1996; Adiwidjaja et al. 1997; Hawthorne and Sokolova 2002; Ohnishi et al. 2007; Rastsvetaeva et al. 2012), corrosion of Zn (Odnevall and Leygraf 1993, 1994; Almeida et al. 2000; Meng et al. 2019), corrosion protection (Stanimirova et al. 2016; Wang et al. 2019), thermal decomposition (Bear et al. 1987; Adiwidjaja et al. 1997; Stanimirova et al. 2016; Gorodylova et al. 2017; Delcheva et al. 2019), dehydration and rehydration (Stanimirova et al. 2017) and as ion-exchange materials (Rujiwatra et al. 2001; Stanimirova 2019). Several studies show the potential application of the Zn hydroxy-sulfate minerals as a precursor for ZnO (He et al. 2013; Machovsky et al. 2013; Moezzi et al. 2013; Liang et al. 2015). Gordaite and Namuwite are two zinc hydroxy-sulfate minerals. Studies of “zinc rust” show that these two minerals can form a protective layer on zinc and zinc alloys (Stanimirova et al. 2016). Recently, Wang et al. (2019) found that well-dispersed Namuwite nanoplates as coating are an effective corrosion protection due to their anion and cation exchange capacity: when incorporating Na^+, Cl^- and water into the structure, for example, Gordaite forms. Gordaite can incorporate not only NaCl. It can also incorporate KCl, $CaCl_2$, and $SrCl_2$, forming a Gordaite analog containing Cl and the cation of the respective salt (Stanimirova 2019).

3.3.2.1. Gordaite

Gordaite is a very rare mineral, observed for the first time in the oxidized zones of Cu-Zn sulfide deposits, e.g., the Francisco Mine in Sierra Gorda, Chile (Adiwidjaja et al. 1997). It also occurs along oxidized sections of a seafloor chimney, at the contact zone of hydrothermal fluids and seawater, e.g., in the Juan de Fuca Ridge, Pacific Ocean southwest of Vancouver Island, Canada (Nasdala et al. 1998) or in Kupferschiefer heaps (Jahn and Witzke 1999). Various phases isostructural with Gordaite

were observed as a secondary mineral in mines. It is also found as a corrosion product in Zn and Zn-Mg-Al slag heaps exposed to a marine environment (Diler et al. 2014). The formation of Gordaite was also reported as a result of the reaction of seawater droplets with zinc surfaces (Cole et al. 2008).

Gordaite $NaZn_4(SO_4)(OH)_6Cl{\cdot}6H_2O$ is a layered Zn-hydroxide salt with a trigonal space group P-3. The first correct description was done in 1997 by Schlüter et al. (1997). It crystallizes as platy, hexagonal crystals that are translucent white to colorless. Figure 3.2 shows the layered crystal structure of Gordaite with the main structural unit $[Zn_6(OH)_{12}O_2]^{4-}$. It is a brucite-like octahedral hydroxide layer with Zinc in the center. Every 7th octahedral site is vacant, and 1/7 of the hydroxides are substituted by oxygen atoms of the sulfate group. On top and bottom of the vacancies are $[Zn(OH)_3Cl]^{2-}$ tetrahedrons located, with three OH-groups connected with the octahedral layer and a Cl^--ion on the apex of the Zn-tetrahedron. The Cl^--ion causes a negative charge of the hydroxide layers. Charge balance is achieved by the incorporation of Na^+-ions with a hydrate shell between the hydroxide layers. The strong hydrogen bonds connect the layers (Adiwidjaja et al. 1997).

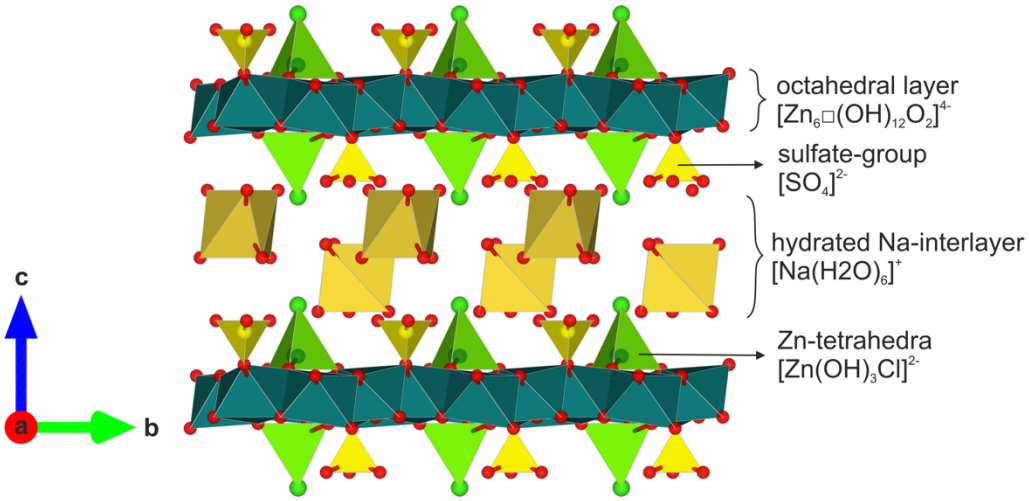

Figure 3.2: Crystal structure of Gordaite in b-c projection. Structure after Adiwidjaja et al. (1997). The crystal structure is created using the software VESTA 3 (Momma and Izumi 2011).

Many researchers have synthesized Gordaite in the laboratory (e.g., Stanimirova et al. 2017; Maruyama et al. 2017b). For synthesis, 1g ZnO powder is mixed with 15 ml of a 1.5 mol/l NaCl and 15 ml of a 0.5 mol/l $ZnSO_4$ solution. The suspension is stirred for 120h, centrifuged, washed with deionized water, and dried at room temperature in a desiccator.

Gordaite has both anion, and cation exchange capacities (Stanimirova et al. 2017), e.g., by replacing the hydrated interlayer sodium cations with hydrated lithium cations (Maruyama et al., 2017a) and by exchange of the Cl^- on the apex of the Zn tetrahedrons. Depending on the boundary conditions, Gordaite can incorporate Na, K, Ca, Li, NH_4, Sr, Ni, Co, Cu as well as Cl and Br (Burns et al. 1998; Jahn and Witzke 1999; Area Maruyama et al. 2017a; Bowles et al. 2018; Mills et al. 2019; Stanimirova 2019).

There are several examples observed in nature, showing that Zn in Gordaite can be completely replaced. Jahn and Witzke (1999) observed Cuprian-Gordaite as a secondary mineral in the heaps of Kupferschiefer ores, in which 50 % of the Zn is replaced by Cu. Kasatkin et al. (2018) described a Co-analogue of Gordaite, Thérèsemangnanite, $NaCo_4(SO_4)(OH)_6Cl{\cdot}6H_2O$. A Ni-rich Gordaite-Thérèsemagnanite is know from Cap Garonne, France (Mills et al. 2019).

3.3.2.2. Namuwite

Namuwite $(Zn,Cu)_4(SO_4)(OH)_6{\cdot}4H_2O$ is a basic zinc sulfate discovered in the Aberllyn lead mine in Wales and first described by Bevins (1982). Later on, it was also observed in Laurion, Greece (Rewitzer and Hochleitner 1989), in lower Saxony and Hesse (Schnorrer-Köhler 1991a, 1991b) and in Tsumeb, Namibia (von Bezing et al. 2008).

Namuwite is a trigonal layered hydroxide salt with space group P-3. It crystallizes either as hexagonal plates or as trigonally-shaped needle-like crystals (Groat 1996). As shown in Figures 3.2 and 3.3, the structure of Gordaite and Namuwite are closely related (Hawthorne and Sokolova 2002). The only difference is that Namuwite contains instead of Cl^- an H_2O molecule at the apex of the Zn-tetrahedra. Therefore, the incorporation of cations such as Na^+ into the interlayers for charge balance is not necessary. Instead, water molecules are in the interlayer space, binding the octahedral sheets together. Depending on the number of water molecules, three minerals with the general formula $Zn_4(SO_4)(OH)_6{\cdot}nH_2O$ can be distinguished; the pentahydrate (n=5) is known as Osakaite, the tetrahydrate (n=4) as Namuwite, and the trihydrate (n=3) as Lahnsteinite.

The synthesis of Namuwite is very similar to that of Gordaite. First, 1g ZnO powder is mixed with 30ml of a 0.5 M $ZnSO_4$ solution and periodically stirred for 72h. After washing, the residue is dried at room temperature (e.g., Stanimirova 2019).

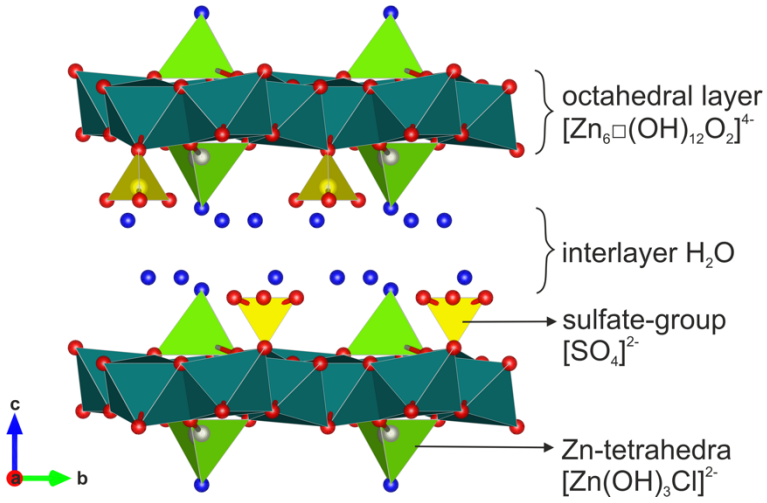

Figure 3.3: Crystal structure of Namuwite in b-c projection. Structure after Groat (1996). Structure plotted using the Software VESTA 3 (Momma and Izumi 2011).

3.3.3. Bechererite

Bechererite with the general formula $(Zn,Cu)_6Zn_2(OH)_{13}[(S,Si)(O,OH)_4]_2$ was first described by Giester and Rieck (1996). The usually light green to transparent mineral was found as a secondary mineral on dump material of the Tonopah-Belmont mine in west-central Arizona associated with Willemite (Zn_2SiO_4), Rosasite ($(Cu,Zn)_2[(OH)_2|CO_3]$), Hydrozincite $Zn_5(CO_3)_2(OH)_6$, Smithsonite $ZnCO_3$, Paratacamite $Cu_3(Cu,Zn)(OH)_6Cl_2$) and Boleite ($KPb_{26}Ag_9Cu_{24}(OH)_{48}Cl_{62}$) (Giester and Rieck 1996).

Bechererite is trigonal with the space group P3. As shown in Figure 3.4, the structure of Bechererite is similar to the LHS minerals Gordaite and Namuwite (Hawthorne and Sokolova 2002). It consists of octahedral layers with every 7th octahedra vacant. In this case, the Zn-tetrahedra, which are located on top and bottom of the vacancies, are connected over the corner. These $[Zn_2O_7]^{6-}$ pyro-groups make the Bechererite structure more stable than the LHS, where the octahedral layers are connected via hydrogen bonds. No procedure for the synthesis of Bechererite in the laboratory was found in the literature.

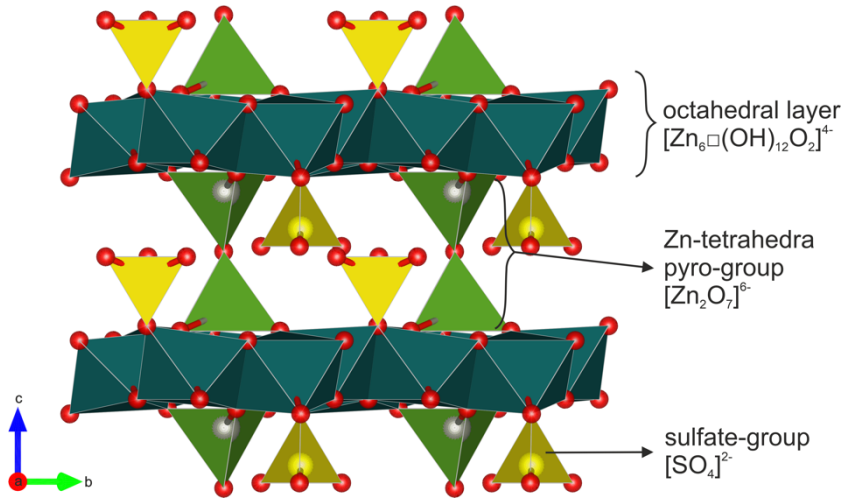

Figure 3.4: Crystal structure of Bechererite in b-c projection. Structure after Giester and Rieck (1996). Structure plotted using the Software VESTA 3 (Momma and Izumi 2011).

3.3.4. Zincite

Zincite is a rare mineral in nature which may occur in non-sulfide zinc deposits as a result of supergene oxidation of the primary sulfide mineralization. In general, Hydrozincite is observed together with Smithsonite or Hemimorphite (Nuspl and Gutzmer 2009). One of the rare locations of Zincite are Franklin and Sterling Hill Mines in New Jersey, together with other Zn-phases like Gordaite. The observed assemblages of Zincite together with Willemite and Franklinite ($ZnFe_2O_4$) indicate specific stability conditions, including high temperatures, a relatively high oxygen fugacity, a low sulfur activity, and a low Quartz saturation (Brugger 2003).

Zincite is hexagonal with the space group $P6_3mc$. Figure 3.5 shows the hexagonal wurtzite structure of ZnO. The crystal structure consists of Zn- tetrahedrons corner-connected by oxygen atoms.

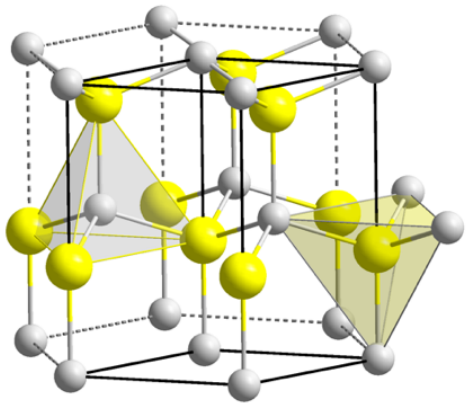

Figure 3.5: Crystal structure of hexagonal ZnO with wurtzite structure (Wikipedia 2008).

ZnO as a chemical substance has exceptional physical and chemical properties and is suitable for a broad field of applications. For example, ZnO is an antifouling and antibacterial material (Al-Fori et al. 2014; Gharoy Ahangar et al. 2015) and is often used in pharmaceuticals or cosmetics (Kolodziejczak-Radzimska and Jesionowski 2014; Pasquet et al. 2014). In cosmetics, it is found as a colorant, for bulking, skin protection, and as a UV absorber (SCCS Scientific Committee on Consumer Safety 2012). In addition, ZnO is a group II-VI n-type semiconductor with a direct bandgap of 3.37 eV and a binding energy of 60 meV at room temperature (Bacaksiz et al. 2008; Baruah and Dutta 2009; Chen et al. 2016). These properties make especially nanocrystalline ZnO useful in the high technology sector as a UV absorber, in photoelectronics as a field emitter, sensor, UV laser, or in solar cells as photocatalyst and various other fields (Kolodziejczak-Radzimska and Jesionowski 2014; Ong et al. 2018).

The wide range of applications for ZnO has led to the development of numerous very different synthesis methods. Educts that are used for synthesis include $ZnCl_2$, $Zn(CH_3COO)_2$, $Zn(NO_3)_2$, $ZnSO_4$, or Zn 2-ethylhexanoate. ZnO can be synthesized metallurgically or mechanochemically, by controlled precipitation reactions, via sol-gel methods, solvothermal and hydrothermal processes, emulsions, microemulsions, and also by growing ZnO via vapor deposition, by using sonochemical methods or microwave technology (Kolodziejczak-Radzimska and Jesionowski 2014; Ong et al. 2018). Most chemical synthesis processes are very complex, and different additives such as surfactants, organic solvents, or acids are necessary. In some cases, calcination/sintering of the intermediate product at temperatures > 300 °C is required to synthesize ZnO (e.g., Ao et al. 2006; Zhang and Yanagisawa 2007). John et al. (2016d) demonstrated the direct precipitation of nanocrystalline ZnO from SO_4-containing wastewater from the electroplating industry. They showed that Zn-containing wastewater could be used as starting material for the hydrothermal synthesis of ZnO.

Gorodylova et al. (2017) reviewed various studies on the thermal stability of layered Zn hydroxychloride ($Zn_5(OH)_8Cl_2 \cdot H_2O$), also called Simonkolleite, and its thermal decomposition into ZnO. In their review, they cite Mata Arjona et al. (1967), among others, who had produced ZnO by decomposition of Simonkolleite under vacuum at a temperature of 110 °C, and stated that ZnO is only detectable from 140 °C onwards. Samanta and Mishra (2013) synthesized ZnO nanodisks at room temperature by adding $ZnCl_2$ droplets into a 0.5M NaOH solution over 5 minutes, followed by 2 hours of stirring. After filtration and washing, the residue was dried at 150 °C. In this case, the system is H_2O-dominated.

In summary, currently practiced wet chemical synthesis routines for Cl-rich media always involve an intermediate phase, such as zinc hydroxide, zinc carbonate, or layered zinc hydroxide chlorides. These intermediate phases are further treated to produce ZnO, either by placing it in an autoclave (Choi et al. 2012), drying at elevated temperatures for several hours (e.g., Samanta et al. 2015) or calcination at temperatures > 300 °C (Chen et al. 2008). All these processes have disadvantages: they are complex, multi-stage processes, require high amounts of energy, and/or require reducing agents so that overall, all processes are cost-intensive. Alternatively, ZnO can be directly obtained after several hours at aging temperatures > 110 °C (Mata Arjona et al. 1967) or only as the main phase in a phase mixture (Delcheva et al. 2019).

To date, no synthesis procedure has been presented to produce ZnO from Cl-rich solutions at temperatures < 110 °C.

4. Material and methods

4.1. Real and synthetic leachate wastewater

4.1.1. Leachate wastewater of MSWI plant Germany

Over four years, nine “leachate wastewaters” were sampled, which were treated according to the FLUWA process (see also Chapter 3.1.1.) at MSWI plant Ingolstadt, Germany. In order to monitor the fluctuations, the most important matrix components (Na, K, Ca, Cl and SO_4) in the wastewater were analyzed in addition to the heavy metals, see Table A.1 in annex.

The boxplot in Figure 4.1a shows the statistical distribution of the main matrix components. The values including box (interquartile range, IQR), within which 75 % of all measured values lie, reflect the fluctuation of the leachate wastewater within the investigation period. The comparison of the median (long line in box) and the average (dot in box) displays to what extent the values are evenly distributed. In general, most of the wastewaters from MSWI Ingolstadt have Cl concentrations > 60000 mg/l and Na-concentrations between 21000 mg/l – 31000 mg/l. The large IQR of the dominant matrix components Na and Cl imply a high fluctuation of the concentration (Figure 4.1a). The deviation

between median and average points to an uneven distribution of the measured values. Minor matrix components are K, Ca, and SO_4, usually with concentrations in the range of 750 -10000 mg/l. The small IQR and the similarity of the median and the average indicate minor fluctuations of these components. In one wastewater, the SO_4 concentration is with 15800 mg/l considerably elevated compared to the other wastewaters.

Figure 4.1b gives an overview of the measured concentrations of the main heavy metals Zn, Pb, Cd, and Cu in the FLUWA-eluates during the study period. The dominant heavy metal is Zn, with concentrations of 700 mg/l – 3570 mg/l. The boxplot shows the extreme variation of Zn by a factor of about 5 and an uneven distribution of values. Besides Zn, Pb is also enriched in the eluate with concentrations varying between 70 mg/l - 1800 mg/l. The very high nonuniformity of the median and mean values is due to a very high measured value of 1780 mg/l Pb (WW-G1). The concentrations of Cd and Cu are usually < 100 mg/l in the leachate wastewaters from MSWI Ingolstadt.

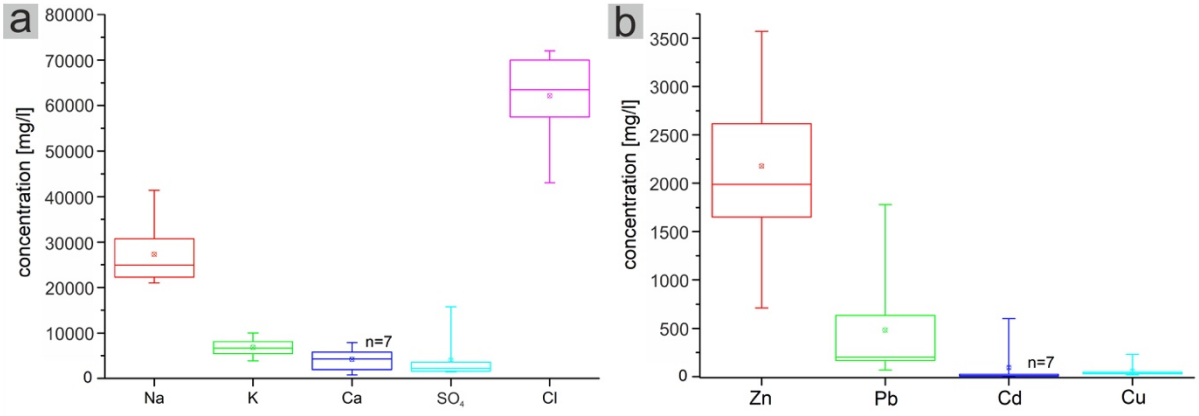

Figure 4.1: Fluctuation of (a) the matrix components (n=8) and (b) the main heavy metals (n=9) analyzed in the leachate wastewaters from MSWI Ingolstadt, Germany, treated after the FLUWA process within the study period 2016 - 2020. n = total number of samples for the respective measurement.

4.1.2. Leachate wastewater of MSWI plant Switzerland

Samples were also taken at a Swiss MSWI plant where the FLUWA-process is optimized and cementation is applied to remove Pb, Cd, and Cu in preparation for hydrometallurgical Zn-recycling using the FLUREC-process (see chapter 3.1.2.). Analyses can be found in Table A.2 in annex. One sample (WW CH-1) was collected directly after the FLUWA process, and the other samples (ZEM CH 1-3) were taken after cementation. Figure 4.2a provides an overview of the matrix components in the Swiss wastewater eluates. The narrow IQR of the matrix components in the figure shows that the concentrations of the components do not fluctuate remarkably. Dominant components are Na and Cl with concentrations around 24000 mg/l and 65000 mg/l, respectively; SO_4 and K concentrations vary between 10000 - 11000 mg/l, and minor amounts of Ca < 1000 mg/l are present in the wastewaters. Figure 4.2b compares the concentration of the main heavy metals in the

wastewater after FLUWA with the Swiss wastewater after cementation, where Pb, Cd, and Cu were electrochemically removed. The comparison of the values before and after cementation clearly shows the effectiveness of the cementation process for the removal of Pb, Cd, and Cu from the wastewater (values < 10 mg/l). What stands out in Figure 4.2b are the high Zn-concentrations in the Swiss wastewater > 12000 mg/l. This is partly caused by the addition of Zn^0-powder for the cementation of the other heavy metals.

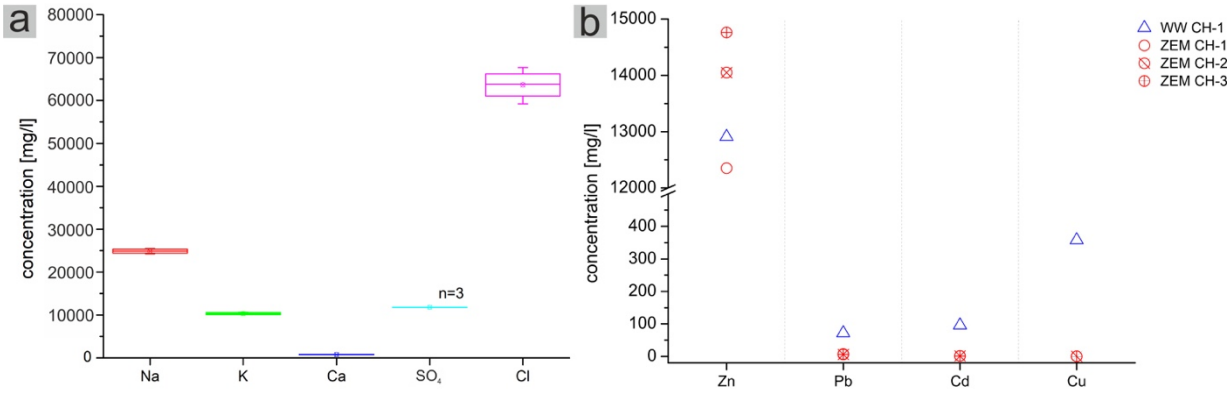

Figure 4.2: (a) Fluctuation of the matrix components (n=4) and (b) concentration of the main heavy metals analyzed in Swiss leachate wastewaters after application of FLUWA process. The wastewaters ZEM CH-1, CH-2, and CH-3 were sampled after applying FLUWA and cementation. n = total number of samples for the respective measurement.

A comparison of the German and Swiss wastewaters can only be made with caution because of the low number of analyses (n=4) of the Swiss wastewater than that of Germany (n=9). Furthermore, cementation was applied to 3 out of 4 wastewaters from Switzerland, which was not the case in any of the German wastewaters. Nonetheless, the concentration of the dominant matrix components of both MSWI, Na and Cl, are similar, while the concentration of K is slightly elevated in the Swiss wastewater. Accordingly, the matrix components seem not to be affected by the cementation process. Significant differences can be found in the fluctuations of the matrix components: the IQR is considerably smaller in all Swiss wastewaters, pointing to less variation in the matrix components. In trend, the concentration of Ca in the Swiss wastewater is lower, whereas the concentration of SO_4 is elevated compared to that of MSWI Ingolstadt, Germany.

The heavy metal concentrations from Germany (see Figure 4.1b) compared to the Swiss data (see Figure 4.2b) illustrate the effect of an optimized FLUWA process. Comparing the untreated leachate wastewater, the Swiss wastewater without cementation is significantly enriched with Zn by a factor of about 5 to 6. Also, the other heavy metal concentrations differ: in Swiss wastewater, the concentration of Pb and Cd is lower, and the Cu-concentration, at 360 mg/l, is higher than in German wastewaters.

4.1.3. Synthetic saline aqueous solution (AQ)

The precipitation experiments in chapters 5.1, 5.2, and 5.3 were carried out using a synthetic aqueous solution (AQ) to eliminate effects caused by additional elements, impurities, or organic matter. The concentration of the matrix components Na, Ca, K, Cl, and SO_4 in the saline AQ is based on sample WW-G1 from MSWI plant Ingolstadt (see Table A.1 in annex). The composition of the saline AQ is listed in Table 4.1. Analytical grade chemicals were used to prepare the saline AQ.

Table 4.1: Composition of the saline aqueous solution (AQ) and the chemicals used for the experiments.

Element	Concentration [mg/l]	Educt	Company, grade of purity
Na	30000	NaCl	VWR, analytical grade
K	7000	KCl,	Merck, analytical grade
Ca	4000	$CaCl_2 \cdot 2H_2O$ $CaSO_4 \cdot 2H_2O$	Merck, analytical grade
SO_4	2500	$CaSO_4 \cdot 2H_2O$	Merck, analytical grade
Cl	70000	HCl 32 %	Merck, analytical grade

First, HCl (32 %) was added to water with high purity (< 2 µS/cm). Then KCl, $CaCl_2 \cdot 2H_2O$, $CaSO_4 \cdot 2H_2O$, and NaCl were added to the solution under continuous stirring. When all salts are dissolved, water of high purity was added until the exact volume was obtained.

4.2. Experimental procedure and analytical methods

4.2.1. Experimental setting and procedure

Figure 4.3 shows the general experimental setup. The solution is contained in a beaker (1) and is stirred mechanically (2). Temperature is set and controlled by a heating plate (3) using a Pt100 thermocouple (4). Temperature and pH are simultaneously monitored by a titrator, either Titrator TL 7000 or Titrator TL 7800 (5) from SI Analytics (Xylem Analytics Germany, Weilheim, Germany), equipped with a Blueline 19 pH electrode (6) and Eh with a Blueline 31 Rx electrode (7). NaOH is added via a titration needle (8) connected to the titrator. All parameters were set, controlled, and recorded with the Software Titrisoft 3.3 from SI Analytics (9).

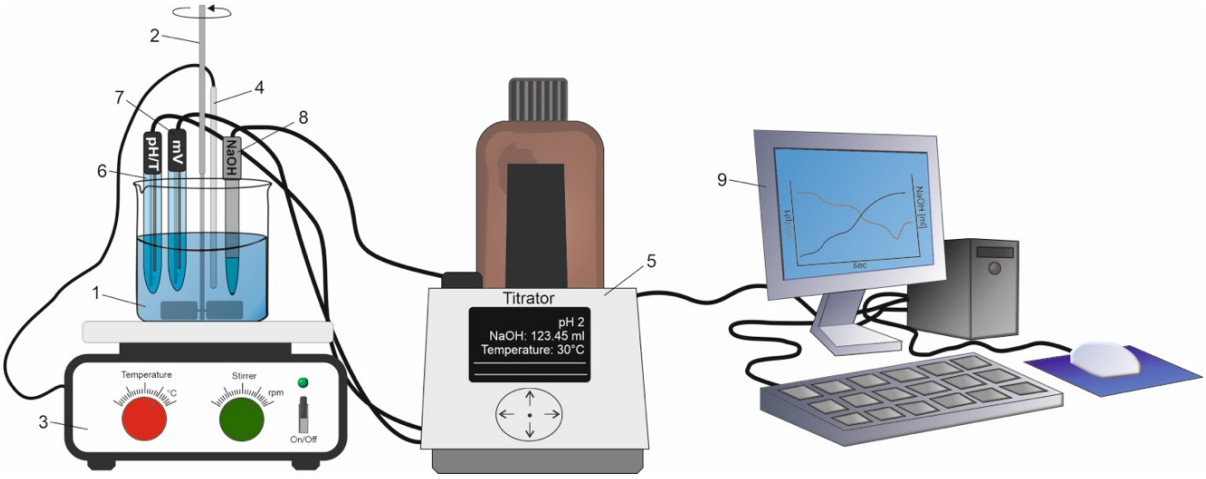

Figure 4.3: Experimental setup: (1) Beaker containing the Me-rich solution, (2) mechanical stirrer, (3) heating plate, (4) Pt100 thermocouple, (5) titration unit, (6) pH electrode, (7) Eh electrode, (8) titration needle, (9) computer with Software SI Analytics.

The precipitation experiments were always carried out as follows: First, the solution was heated up to reaction temperature under continuous stirring. When reaction temperature was reached, Zn was added to the solution either as $ZnCl_2$ or $ZnSO_4 \cdot 7H_2O$ (Merck, Darmstadt, Germany, analytical grade). When needed, Pb was added as $PbCl_2$ (Merck, Darmstadt, Germany, analytical grade). Afterward, the solution was alkalized to pH ≥ 9 by using an 8 molar NaOH. The 8M NaOH solution for alkalization was prepared using pellets (Merck, Darmstadt, Germany, analytical grade) that were dissolved in deionized water (< 2 µS/cm). After the precipitation, pH ≥ 9 was maintained for at least 5 minutes. Subsequently, the suspension was either filtered directly or first aged in a closed vessel at selected aging conditions and then filtered. After filtration, one part was washed three times with deionized water (< 2 µS/cm), while the other part was left untreated. Both residues were dried at room temperature for at least 24 h. Table 4.2 summarizes the main parameters of the experiments that were kept constant during all experiments in the model system. It also includes the change in Cl and SO_4 concentration due to the addition of the Zn-salts.

Table 4.2: Main parameters for precipitation experiments that were kept constant.

Main Parameter	
Zn-concentration	2000 – 2500 mg/l
Final pH	≥ 9
NaOH for alkalization	8 M
Cl increase due to $ZnCl_2$ as educt	+ 2170 mg/l
SO_4 increase due to $ZnSO_4 \cdot 7H_2O$ as educt	+ 2940 mg/l

4.2.2. Analytical methods

4.2.2.1. Water analysis

Cation analysis

The concentration of cations in the synthetic and real wastewater before and after the precipitation experiments were determined using an ICP-OES or an ICP-MS. Analyses were performed according to DIN EN ISO 17294-2 (E29) by the Bavarian Environment Agency (Augsburg, Germany) using an ICP-OES, type Optima 2000DV by Perkin Elmer, or by the Stadtwerke München (Munich, Germany) using an ICP-MS, type 7500 from Agilent Technologies. Before every water analysis, an aliquot of the solution was diluted to a measurable range, and 1 vol.-%-HNO_3 (VWR chemicals, 67 %, NORMATOM®) was added. Due to the very high matrix concentrations, especially of Na and Cl in the solutions, the samples needed to be diluted considerably. Therefore, the detection limit of the measurements is 2 mg/l. The low concentration of the cation to be measured compared to the high concentration of the matrix and in addition, interferences caused by the matrix composition, can cause high relative standard deviation (RSD) of the measurements. All samples were prepared at the Department for Earth and Environmental Sciences (DEES), LMU Munich (Munich, Germany).

Every sample was measured three times with an internal standard (Sc & Y), and the RSD was calculated. When the detection limit is reached, no RSD is given. Equation 4.1 was used to calculate the removal efficiency of the cations, i.e., how many of the heavy metal ions precipitate from the solution. When ZnO is the only phase that precipitates, this equation also reflects the reaction yield of ZnO from the solution.

(4.1) $$removal\ efficiency\ of\ Zn\ [\%] = \ reaction\ yield\ ZnO\ [\%] = 100 - \frac{c_1}{c_0} * 100,$$

where c_0 is the initial concentration and c_1 is the concentration after precipitation.

Anion analysis

The concentration of Cl and SO_4 in the real wastewater was determined by ion-chromatography at the DEES, LMU Munich (Munich, Germany). For the measurements, all samples were diluted with ultrapure water (18.2 MΩ) until they were in a measurable range.

Measuring conditions are listed in Table 4.3. To determine the RSD of the measurements, standards of another batch were measured after calibration, and the RSD was calculated. The RSD for Cl and SO_4 was always < 1 %.

Table 4.3: Measuring conditions for anion chromatography and RSD for Cl and SO_4.

Flow rate	0.95 ml/min
Injection volume	25 µl
Elute	8 mM Na_2CO_3/1.0 mM $NaHCO_3$
Cell temperature	30 °C
RSD Cl (%)	< 1
RSD SO_4 (%)	< 1

RSD error propagation

Error propagation was calculated after Harris (2014) according to equation 4.2. The total relative standard deviation (RSD) equals the sum of the squared RSD´s of the individual measurements.

(4.2) $$RSD_{total}[\%] = \sqrt{\sum RSD[\%]_{c_x}^2},$$

where RSD_{total} is the total relative standard deviation in [%] and RSD_{cx} is the RSD in [%] of the individual measurement.

4.2.2.2. Mineralogical characterization

In order to assign and verify the phases in XRD and FTIR spectroscopy, we considered various literature dealing with possible Pb and Zn compounds, such as phases observed in specific locations such as Laurion, Greece (Gelaude et al. 1996), investigated for crystal structure and chemistry (e.g., Groat 1996; Adiwidjaja et al. 1997; Hoffmann et al. 1997; Hawthorne and Sokolova 2002), or found as corrosion products (e.g., Santana et al. 2012).

Powder X-ray diffraction (XRD)

The phase composition of the solid residues after the precipitation experiments was analyzed by X-ray powder diffraction using a GE XRD 3003 TT with Bragg-Brentano geometry at the DEES, Section for Crystallography, LMU Munich. The ground samples were measured on brass sample holders or on zero-background quartz holders and rotated during the whole measurements for better counting statistics. Operation conditions were 40 kV and 40 mA with a primary monochromator. For data collection $Cu_{K\alpha1}$ radiation (λ= 1.540 Å) was used. Measuring conditions are listed in Table 4.4.

Table 4.4: Conditions for X-ray diffraction measurements.

Parameter	Brass sample holder	Zero BG quartz holder
Scans	2	2
Step-width (°2θ)	0.013	0.013
Exposure time (s)	20	100
Range (°2θ)	5 - 80	5 - 80

The obtained diffraction patterns were compared with patterns from the Inorganic Crystal Structure Database (ICSD, FIZ Karlsruhe, 2021) and the Crystallography Open Database (COD) (Downs and Hall-Wallace 2003; Gražulis et al. 2009, 2012, 2015; Merkys et al. 2016; Quirós et al. 2018) using the Software Match3!.

Fourier transform infrared spectroscopy

Phases with low crystallinity were analyzed using Fourier transform infrared spectroscopy (FTIR). Part of the spectra were recorded on an EQUINOX55 using KBr-powder pellets and Software OPUS 4.2 (Bruker) at the DEES, Section for Mineralogy, Petrology, and Geochemistry, LMU Munich. For the preparation of the KBr-pellets, 1 mg of ground sample was mixed with 200 mg ± 1 % KBr (Roth, Karlsruhe, for IR-Spectroscopy), that was dried for at least 24h at 110 °C, and the mixture was pressed into a pellet with 10 tons pressure for 1 min. The other spectra were recorded on a Spectrum Two FT-IR Spectrometer equipped with a monolithic diamond GladiATR unit by Pike Technologies and Software Spectrum 10 (PerkinElmer) at the DEES, Section for Crystallography, LMU Munich. Using this setup, the ground sample can be measured without further sample preparation by applying the powder directly onto the diamond of the ATR unit by a pressure device.

All spectra were recorded in a range from 400 – 4000 cm^{-1} with 4 cm^{-1} spectral resolution and are averaged over a total of 64 scans. The raw spectra were corrected for atmospheric interferences and baseline, when needed. Assignment and deconvolution of the band maxima in the spectra was done using the Software PeakFit. All spectra were normalized, and the fitted spectra were compared with files of the database RRUFF (Lafuente et al. 2015) and the literature and cited accordingly in the results sections of chapter 5.

Scanning electron microscopy

Selected samples were analyzed by scanning electron microscopy (SEM) and energy-dispersive X-ray spectroscopy (EDX) on a SU 5000 Schottky FE-SEM (Hitachi) at the DEES, LMU Munich. For best results, the dispersion method was used for the sample preparation. A small amount of the ground sample (< 0.5 mg) was added to isopropyl alcohol. The suspension was placed in an ultrasonic bath for 5 minutes to avoid agglomerates. The suspension was then dispersed on a silicon single crystal wafer acting as sample holder. After drying, the sample holder was coated with 5 - 7 nm carbon (imaging and EDX) or 5 nm gold (imaging) to ensure a conducting surface. The images were taken with accelerating voltages of 4 - 5 kV and a working distance of 3.4 – 3.6 mm. Working distance for collecting the EDX spectra was 10 mm.

5. Development of an SPOP-based process to precipitate Zn as ZnO from Cl-rich solutions

5.1. Influence of salinity and Pb on the precipitation of Zn: experiments in a model system at temperatures ≤ 40 °C

5.1.1. Purpose, scope, and nomenclature

John et al. (2016d) have already successfully recovered Zn from SO_4-containing wastewater as nanocrystalline ZnO particles using SPOP. The effects of increased Cl-concentration and the presence of another element such as Pb on the precipitation of phases have not yet been studied. Pb was chosen because it is next to Zn the most abundant heavy metal in the fly ash eluates after the FLUWA see chapter 4.1.1.). Therefore, experiments with a synthetic saline aqueous solution (AQ) of different saline concentrations were performed. The aim was to study the influence of varying salinity and Pb on the precipitation of Zn at temperatures ≤ 40 °C.

Nomenclature: The first part of the nomenclature in this chapter represents the main element Zn. The second, where necessary, indicates the concentration of Pb relative to Zn (cast as a percentage). The last part of the nomenclature denotes the AQ of the experiment: “high” for the high saline, “med” for the medium saline, and “low” for the low saline solution, e.g., Zn_10Pb_low denotes the experiment with Zn and 10 % Pb (200 mg/l) in low saline solution.

5.1.2. Experimental series (Sets 1, 2, and 3)

Sets 1 and 2: Influence of salinity

Two experimental sets were conducted to investigate the influence of salinity. Table 5.1 summarizes the composition of the AQ in the “Zn system” (Set 1). In Set 1, the Zn system, the impact of salinity on Zn precipitation was studied. Aqueous solutions with three different compositions were applied: a low saline, medium saline, and high saline AQ.

Table 5.1: Composition of the aqueous solutions (AQs) in the Zn System (Set 1).

Set	System	Experiment	Zn [mg/l]	Pb [mg/l]	Na [mg/l]	K [mg/l]	Ca [mg/l]	SO_4 [mg/l]	Cl [mg/l]
1	Zn	Zn_low	2000	0	0			2900	0
		Zn_med			3000	700	400	3150	7000
		Zn_high			30000	7000	4000	5400	70000

In Set 2, the Zn–Pb system, the influence of Pb on the precipitation of Zn in the three different AQs was tested (Table 5.2). Therefore, 200 mg/l Pb was added (10 % Pb of Zn concentration). The "low saline" solution in the Zn and Zn–Pb systems contained about 0 to 3000 mg/l sulfate and chlorine. Concentrations in "medium saline" solutions varied between 7000 and 9200 mg/l chlorine and 250 to 3150 mg/l sulfate. "High saline" AQs contained ≥ 70000 mg/l chlorine and ≥ 2500 mg/l sulfate.

Table 5.2: Composition of the aqueous solutions (AQs) in the Zn-Pb System (Set 2).

Set	System	Experiment	Zn [mg/l]	Pb [mg/l]	Na [mg/l]	K [mg/l]	Ca [mg/l]	SO_4 [mg/l]	Cl [mg/l]
2	Zn–Pb	Zn_10Pb_low	2000	200	0				2200
		Zn_10Pb_med			3000	700	400	250	9200
		Zn_10Pb_high			30000	7000	4000	2500	72200

Set 3: Influence of Pb

Table 5.3 shows the composition of the AQ in the "Zn-Pb-salt system" (Set 3). The aim here was to study the impact of Pb variation on the precipitation of Zn. The AQ in the Zn-Pb-salt system was always high saline, and the Pb-concentration was varied from 100 to 800 mg/l. The reaction temperature was 30 °C for the Zn system (Set 1) and 40 °C for both, the Zn-Pb system (Set 2) and the Zn-Pb-salt system (Set 3).

Table 5.3: Composition of the aqueous solutions in the Zn–Pb–salt System (Set 3).

Set	System	Experiment	Zn [mg/l]	Pb [mg/l]	Na [mg/l]	K [mg/l]	Ca [mg/l]	SO_4 [mg/l]	Cl [mg/l]
3	Zn–Pb–salt	Zn_5Pb_high	2000	100	30000	7000	4000	2500	72200
		Zn_10Pb_high		200					72240
		Zn_40Pb_high		800					72440

5.1.3. Results

5.1.3.1. Influence of salinity

Water purification

Table 5.4 summarizes the heavy metal concentrations of Sets 1 and 2 in the filtrates after the experiments. The calculated removal efficiency of ions reflects the recovery of the heavy metals from the solution. Thus, a high removal efficiency means that the metals are enriched in the precipitates.

Table 5.4: Concentration (mg/l) and removal efficiency (%) of Pb and Zn after the experiments of Sets 1 and 2.

Set	Experiment	Conc. Zn [mg/l]	Removal Efficiency of Zn (%)	Conc. Pb [mg/l]	Removal Efficiency of Pb (%)
1	Zn_low	≤ 0.05	> 99.99	-	-
	Zn_med	0.60	99.97	-	-
	Zn_high	3.20	99.84	-	-
2	Zn_10Pb_low	81.24	95.94	6.48	96.76
	Zn_10Pb_med	0.30	99.98	0.29	99.85
	Zn_10Pb_high	1.22	99.94	0.8	99.60

Figure 5.1 gives an overview of the removal efficiency of Zn and Pb in the Zn system and the Zn-Pb system. In the Zn system (Set 1), the removal efficiency achieved in the experiment with low saline AQ was better than 99.9 %. With increasing salinity, the removal efficiency for Zn decreased, even though it remained always > 99.8 %. After the experiment with high saline solution, the concentration of Zn was 3.2 mg/l (see Table 5.4).

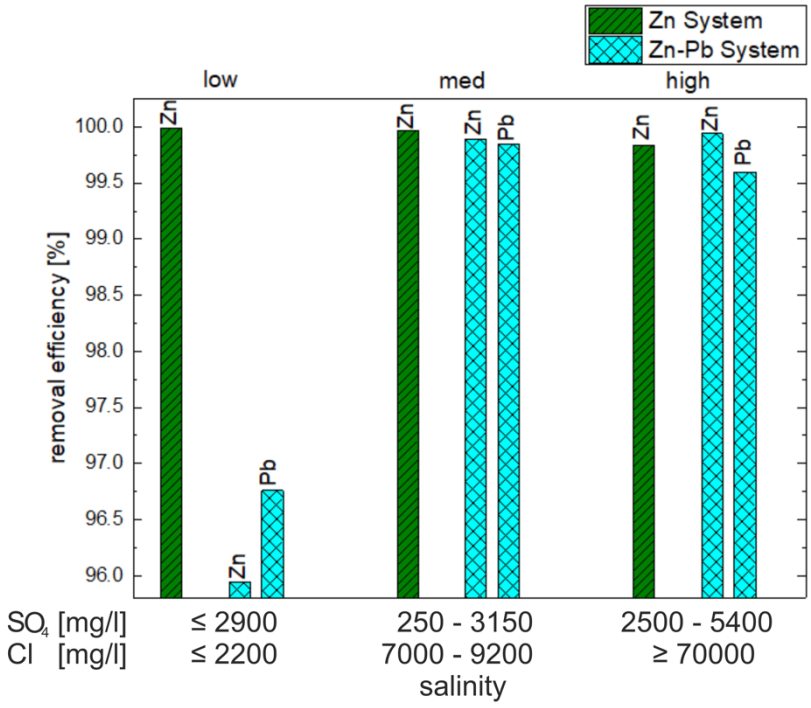

Figure 5.1: Removal efficiency ranging from 95 – 100 % of Zn and Pb in dependence of salinity in the Zn system (Set 1) and the Zn-Pb system (Set 2).

A different effect was observed in the Zn-Pb system (Set 2), with 10 % Pb added to the Zn-containing AQ (see Figure 5.1). The experiment with low saline AQ shows the lowest removal efficiency among the tested systems of 95.9 % for Zn and 96.8 % for Pb. The best results were obtained in the experiment Zn_10Pb_medium performed with medium saline solution. After the experiment, > 99.9 % Zn and 99.8 % Pb were removed. In high saline solution, however, the removal efficiency decreased again for

both Zn and Pb, even though the result was better than in the experiment with low saline AQ. In comparison with the Zn system (Set 1), the removal efficiency was even slightly better. After precipitation, the chlorine concentration in the AQ did not change with increasing salinity, whereas the concentration of sulfate decreased.

Mineralogical Characterization

XRD results

Zn system (Set 1): Figure 5.2 shows the change in the XRD pattern of the washed precipitates in the Zn system. The XRD patterns show that the salinity of the solution has an impact on the precipitated phases. The main phase in the experiment with low saline AQ was Zincite (ZnO) with sharp peaks at 31.94° 2θ, 34.44° 2θ, and 36.27° 2θ and related minor peaks (COD-ID 9011662). At 8.53° 2θ, there was a broad peak that matches the main reflex of Namuwite, $Zn_4(SO_4)(OH)_6{\cdot}4H_2O$ (COD-ID 9001719). A sharp peak with low intensity at 11.78 °2θ corresponds to Bechererite with the general formula $(Zn,Cu)_6Zn_2(OH)_{13}[(S,Si)(O,OH)_4]_2$; the additional minor peaks were also observed.

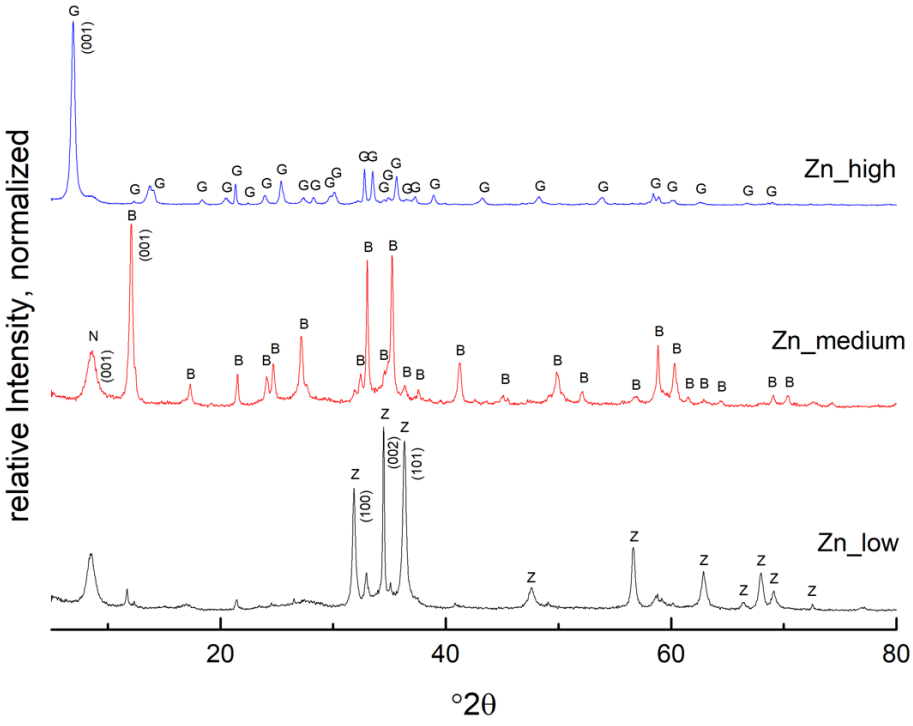

Figure 5.2: XRD pattern (Cu Kα₁) of the washed precipitates in the Zn system (Set 1) with increasing salt content in the aqueous solution.

Zincite was not detected in the experiment with medium saline AQ (Zn_medium). The main phase was Bechererite in addition to a minor amount of Namuwite. As shown in Figure 5.2, compared to experiment Zn_low, performed with low saline AQ, the intensity of the Bechererite reflexes are significantly higher.

With increasing salinity, the concentration of chloride and sulfate increased in the precipitate. The main phase in the experiment with high saline AQ was Gordaite ($NaZn_4(SO_4)(OH)_6Cl{\cdot}6H_2O$), with the main peak (001) at 6.84° 2θ. A broad peak with low intensity next to the main reflex of Gordaite indicates the main peak (001) of Namuwite. No other phases were detected in the XRD pattern of the washed precipitate Zn_high.

Zn-Pb system (Set 2): Figure 5.3 shows the XRD pattern of the washed precipitates with increasing salt content in the Zn-Pb system. The main phase in the experiment with low saline AQ is Zincite. In comparison, the experiment with medium saline AQ shows lower overall intensities with broad peaks of Bechererite and a differing proportion of Zincite main peaks. Small peaks at 24.68 °2θ and 27.11 °2θ could not be assigned to any known phase. In contrast to the Zn system (Set 1; Figure 5.2), Namuwite was not detected in the experiments with low or medium saline AQ. A change in intensity of the Zincite main peaks was also observed.

In the salt-rich experiment Zn_10Pb_high (Set 2), Gordaite was the main phase (see Figure 5.3). A broad peak with low intensity next to the main peak of Gordaite indicates small amounts of Namuwite. Other phases were not observed. No Pb-bearing phase was detected in all three experiments with 10 % Pb, neither in the XRD patterns nor in the FTIR spectra.

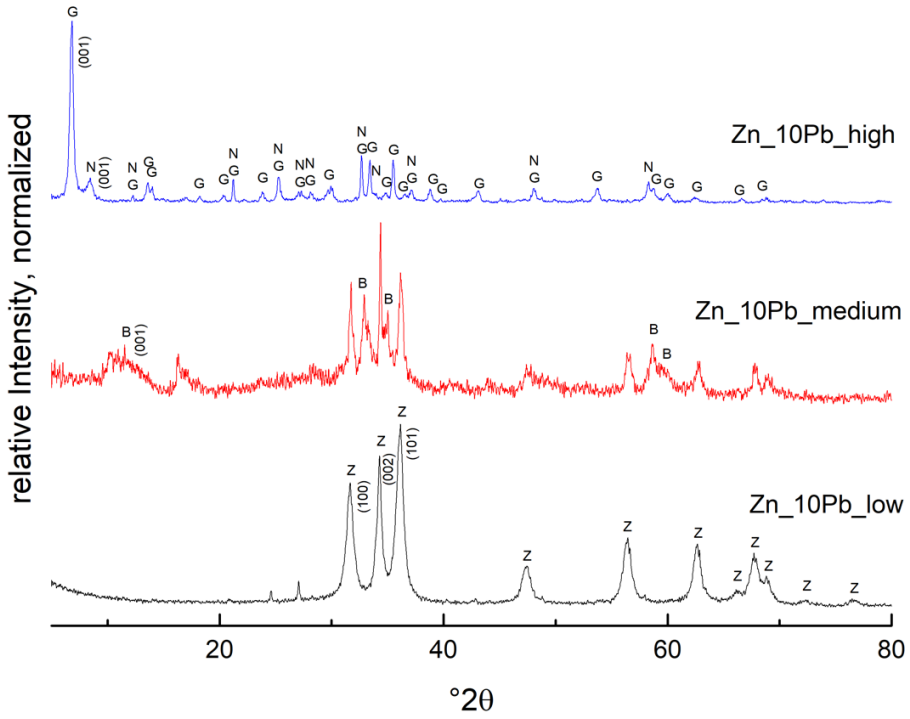

Figure 5.3: XRD pattern (Cu Kα$_1$) of the washed precipitates in the Zn-Pb system (Set 2) with increasing salt content in the aqueous solution.

5.1.3.2. Influence of Pb in high saline solution

Water purification

Table 5.5 summarizes the heavy metal concentrations in the filtrates after the experiments of Set 3.

Table 5.5: Concentration (mg/l) and removal efficiency (%) of Pb and Zn after the experiments of Set 3.

Set	Experiment	Conc. Zn [mg/l]	Removal Efficiency of Zn [%]	Conc. Pb [mg/l]	Removal Efficiency of Pb [%]
3	Zn_5Pb_high	1.17	99.94	0.74	99.26
	Zn_10Pb_high	1.22	99.94	0.80	99.6
	Zn_40Pb_high	1.23	99.94	0.86	99.89

In Set 3, the effect of varying Pb concentration from 5 % to 40 % relative to Zn (2000 mg/l) in a high saline solution was studied (see Table 5.5). As shown in Figure 5.4, variation of Pb did not have an impact on the removal efficiency of Zn (99.9 %). With increasing Pb-content in the high saline solution, the removal efficiency of Pb increased from 99.3 % to 99.9 %.

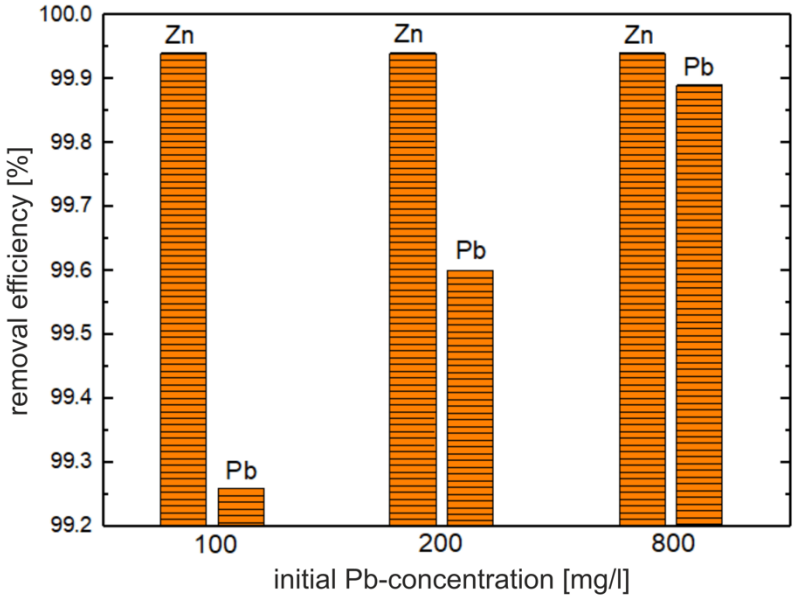

Figure 5.4: The dependence of Pb concentration on the removal efficiency ranging from 99.2 – 100 % in the Zn-Pb-salt system (Set 3).

Mineralogical Characterization

XRD

Figure 5.5 shows the effect of a Pb ratio between 5 % and 40 % on the XRD pattern of the washed precipitates in the Zn-Pb-salt system with high saline AQ. The XRD patterns of all experiments are very similar. The reflexes match to Gordaite as the main phase. Starting with a concentration of 10 % Pb in the solution, a broad peak appears next to the main peak of Gordaite, matching the (001) reflex of

Namuwite. When 40 % Pb was added, the relative intensity of this reflex decreased. Additional reflexes occurring in the XRD pattern match Laurionite (Pb(OH)Cl) with main peaks at 22.15 °2θ (210), 27.06 °2θ (111), and 35.49 °2θ (301).

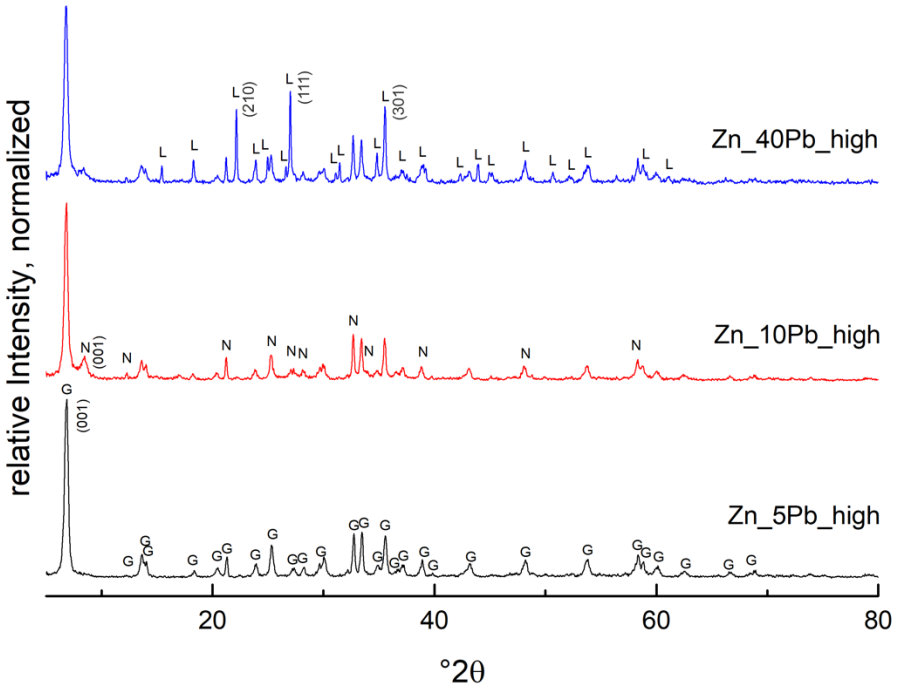

Figure 5.5: XRD pattern (Cu Kα$_1$) of the washed precipitates in the Zn-Pb-salt system (Set 3) with increasing Pb content in high saline solution.

FTIR

Figure 5.6 shows the FTIR spectra of the washed precipitates from experiments with varying Pb concentration in high saline AQ (Set 3). The variation of Pb from 5 % to 40 % shows only slight effects. The relative intensity of the bands of Namuwite at 1158 cm^{-1} and 1387 cm^{-1} increased slightly with increasing Pb concentration. This effect is observable at 390 cm^{-1}, too. Bands of Laurionite show no change in their intensity and are always present. Bechererite bands show a slight decrease at 815 cm^{-1}. A shift of the bands with increasing Pb content was not observed.

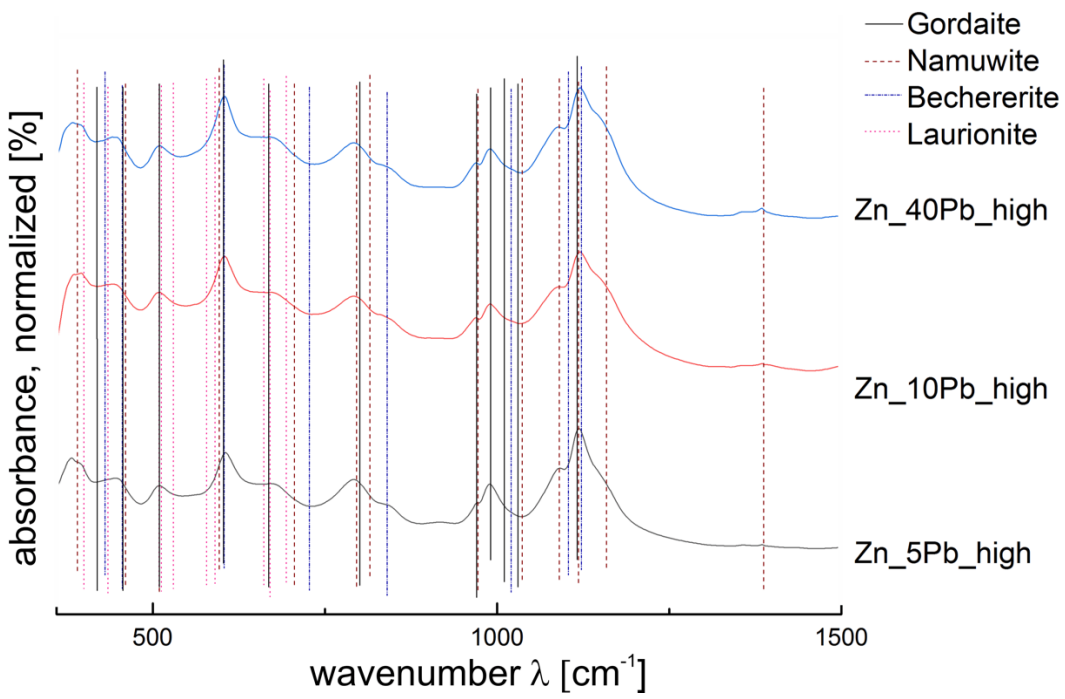

Figure 5.6: Fingerprint area (400 – 1500 cm^{-1}) of the IR Spectra of the washed precipitates in the Zn-Pb-salt system (Set 3) with varying Pb content.

5.1.3.3. Washing the precipitates

One part of the precipitates was always washed before mineralogical characterization to remove water-soluble salts, such as Halite; the other part was left as is. In the experiments with low saline AQ, no change of the XRD pattern was observed. However, after washing the precipitates obtained from AQ with medium and high salinity, the XRD pattern differ.

Zn system (Set 1): Figure 5.7 shows the XRD pattern of the washed (_w) and unwashed (_uw) precipitates of experiment Zn_medium. The XRD pattern of the unwashed sample exposes sharp peaks of Gordaite as the main phase and minor peaks of Bechererite. After washing the precipitate, the XRD pattern in the experiment with medium salinity in AQ differed considerably. Bechererite occurred as the main phase together with smaller, broad peaks assigned to Namuwite. Gordaite was no longer detected.

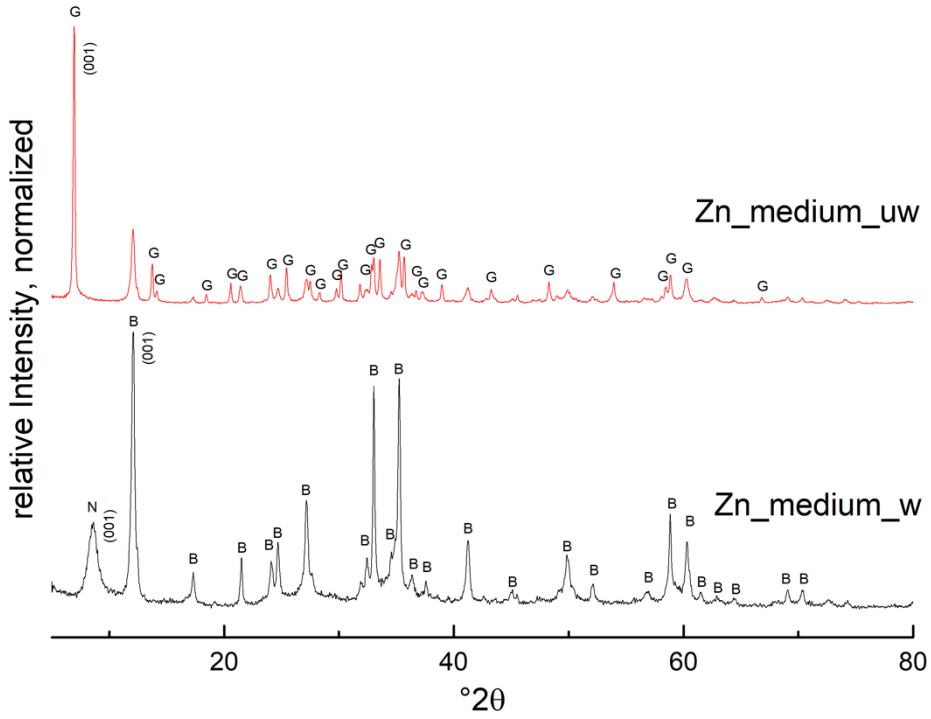

Figure 5.7: XRD pattern (Cu Kα$_1$) of the washed (_w) and unwashed (_uw) precipitates of experiment Zn_medium (Set 1).

Zn–Pb system (Set 2): In the experiment with 10 % Pb added to AQ, the main phases of the unwashed samples were Halite and Gordaite together with a small amount of Zincite and traces of Bechererite. After washing the precipitate, Halite and Gordaite were no longer present, and Zincite and broad peaks of Bechererite were observed.

Zn-Pb-Salt system (Set 3): No significant change in the phases was observed in the experiments with high saline AQ and varying Pb content. After washing the residue, the intensity of the Gordaite peaks slightly decreased, and that of Namuwite increased.

5.1.4. Discussion

5.1.4.1. Effect of salinity in the Zn and Zn-Pb system (Sets 1 and 2)

Figure 5.8 gives an overview of the experimental results. The increasing salinity in the AQ promotes the formation of phases with higher sulfate, chlorine, and hydroxide in the structure. The various types of Zn sulfate hydroxides reflect the increasing incorporation of Cl and SO_4 in the residue.

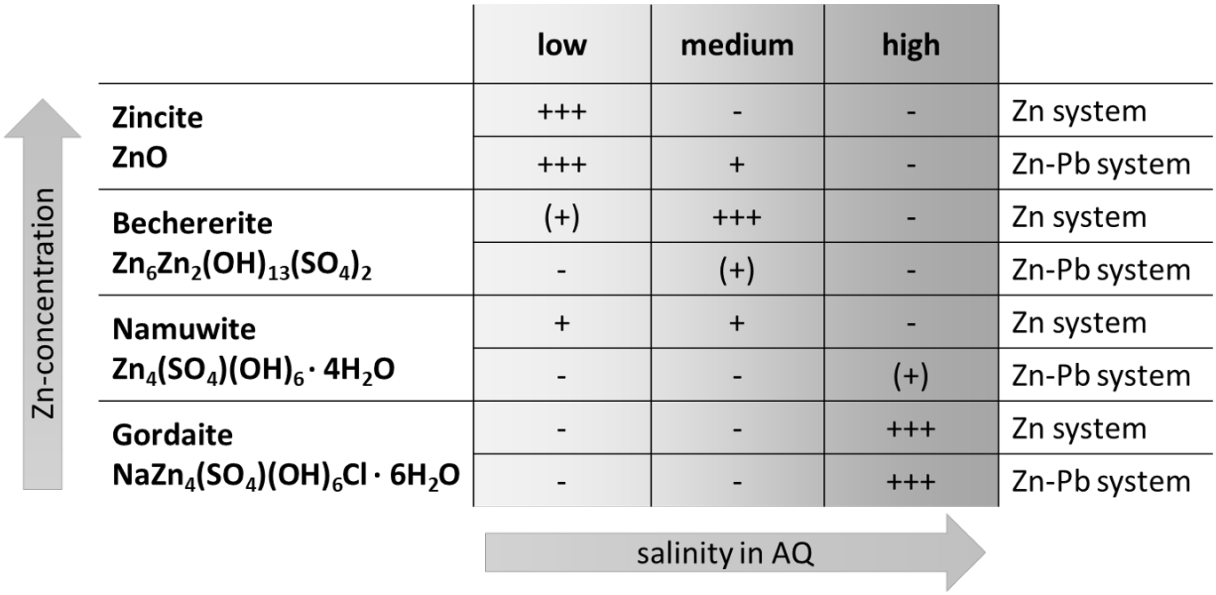

Figure 5.8: Crystalline phases in the Zn system (Set 1) and the Zn-Pb system (Set 2) as a function of the salinity in the AQ. +++ = high relative proportion, (+) = traces of the phase, - = not detected.

In the Zn system (Set 1), Zincite is only formed in low saline AQ together with low amounts of Zn-sulfate-phase Namuwite. The high recovery rate > 99.9% for low saline AQ is in accordance with John et al. (2016d). At optimum conditions, the authors obtained mainly Zincite nanoparticles and noticed that the amount of co-precipitated phases, Smithsonite ($ZnCO_3$) and Zinc-hydroxide ($Zn(OH)_2$), was below the detection limit of XRD. The occurrence of Namuwite and the lack of Smithsonite or Zinc-hydroxide in our experiment Zn_low is most probably due to the differing AQ composition. With increasing salinity, at medium concentrations (7000 to 9200 mg/l chlorine, 250 to 3150 mg/l sulfate), Zincite is replaced by Bechererite, whereas Namuwite is still present. An absence of Cu and Si does not limit the formation of Bechererite; it solely affects the chemistry of the solid solution. The broad profile of the Namuwite peaks indicates that this phase has low crystallinity (Le Bail 2008). At high salinity (≥ 70000 mg/l Cl), Gordaite preferentially grows, which means the additional incorporation of Na, Cl, and water into the crystal structure.

The addition of 10 % Pb to the AQ in the Zn-Pb system (Set 2) has a strong impact on the stability of Zincite (see Figures 5.1, 5.4, and 5.8). The lower Zn removal efficiency observed in the presence of Pb at low salinity indicates that Pb inhibits the precipitation of Zincite. However, the presence of Zincite at medium salinity means that the stability field of Zincite can be enlarged significantly by adding Pb. The changing intensity of the three main peaks of ZnO in low and medium AQs is a strong indication for a changed morphology of the ZnO particles (Wu et al. 2007; John et al. 2016d). In the presence of foreign atoms, the preferential growth of the ZnO nanostructure can be modified (Abdelmohsen et al. 2017). Furthermore, the low intensity of the reflexes in medium saline AQ is interpreted as a decrease in the crystallinity or size of the phases. Changes in the crystal structure (atomic positions, occupancy,

and texture) of the precipitates may also lead to a decrease in their intensity with respect to the background (Dinnebier and Billinge 2008; Le Bail 2008). A lower content of Bechererite at intermediate salt contents compared to the Zn system is obviously affected by the larger stability field of Zincite. In contrast to the Zn system, the presence of Pb in the solution shifts the stability field of Namuwite to higher Cl concentrations. Gordaite is the stable phase in the high saline AQ independently of the Pb-concentration (see Figure 5.8).

5.1.4.2. Effect of Pb in the Zn-Pb-salt system

Figure 5.9 displays the formation of crystalline phases with varying Pb concentration. The experiments in the high saline Zn-Pb-salt system show that Pb has no impact on the removal efficiency of Zn. Furthermore, the removal efficiency of Pb increases with higher Pb concentration in the solution, even though Pb-containing phases were only detected at 40 % Pb by XRD. The absence of Laurionite at < 40 % Pb in AQ implies that a sufficiently high concentration of Pb in the solution is necessary to form a distinct Pb-containing phase that can be detected via XRD. The very similar IR spectra of the three experiments in Figure 5.6 show that almost all bands of Gordaite, Namuwite, Bechererite, and Laurionite are superimposed. Therefore, it also seems possible that Laurionite is already present at lower Pb concentrations < 40 % but is not detected because the content lies below the detection limit of XRD, which is approximately at 3 wt.-%. These results correspond very well with observations in natural environments, as Laurionite is only observed in the presence of salt in rocks. Regenspurg et al. (2015) identified Laurionite in highly saline geothermal fluids from a Permian Rotliegend reservoir. They concluded that the formation of the Pb-hydroxychloride is favored at pH values above 7.2 and low temperatures (Regenspurg et al. 2015).

	5 % Pb	10 % Pb	40 % Pb
Zn-concentration ↑			
Bechererite $Zn_6Zn_2(OH)_{13}(SO_4)_2$	-	-	-
Namuwite $Zn_4(SO_4)(OH)_6 \cdot 4H_2O$	-	(+)	(+)
Gordaite $NaZn_4(SO_4)(OH)_6Cl \cdot 6H_2O$	+++	+++	+++
Laurionite $Pb(OH)Cl$	-	-	++
	Pb-content in solution →		

Figure 5.9: Crystalline phases in the Zn-Pb-salt system (Set 3) as a function of Pb concentration in the AQ. +++ = high relative proportion, (+) = traces of the phase, - = not detected.

Another possible explanation for the improved removal efficiency of Pb is its incorporation in the structure of the mineral phases, such as Gordaite, Bechererite, or Namuwite. Ion exchanges should be detectable with XRD or FTIR because of the differing size of the ions. However, we observed no shift in the position of the reflexes in XRD or bands in the FTIR pattern. The minor changes in the intensity of the (001) reflex of Namuwite in the experiment with 10% Pb point rather to changed stability fields of Namuwite at the expense of Bechererite.

In general, the substitution of Pb^{2+} by Zn^{2+} is not expected since, compared to Zn^{2+}, the ionic radius of the Pb^{2+} ion in an octahedral environment is too large. However, all these minerals - Gordaite, Bechererite, and Namuwite - have a sheet structure with hydrogen bonds between the layers, which allows for higher flexibility of the structure. Thus, ions such as Pb^{2+} can substitute vacancies and may replace Zn^{2+} in the structure. Maruyama et al. (2017a) synthesized Gordaite and studied the exchange capacity with Ca, K, and Li. They concluded that Gordaite has high potential as a cation exchanger layered hydroxide salt.

5.1.4.3. Effect of washing the precipitates

A dependency between washing the precipitates and Pb concentrations could not be found. There is no change of intensity in the XRD patterns of Laurionite. The same was observed for Zincite; we could not find a difference in the XRD pattern of Zincite after washing. However, the comparison of the washed and unwashed XRD patterns showed that the Cl-rich phases of Gordaite and Halite disappeared after washing with pure water. This effect is very reasonable for Halite because of its high solubility in water. Gordaite, however, is not soluble in pure water. Maruyama et al. (2017b) also washed their precipitates after synthesis, and the Gordaite did not disappear. Comparing the XRD pattern of the Zn_medium unwashed and washed (Set 1) residues showed no change for Bechererite. However, the disappearance of Gordaite after washing was accompanied by the occurrence of Namuwite with broad peaks. The washed precipitates of both the Zn-Pb system (Set 2) and the Zn-Pb-salt system (Set 3) show the same trend; the only difference is the changed intensity of the phases, with the highest effect observed at medium salinity. The lower intensity observed in medium saline AQ is interpreted as a decrease in the crystallinity or size of the phases. Changes in the crystal structure (atomic positions, occupancy, and texture) of the precipitates may also lead to a decrease in their intensity (Dinnebier and Billinge 2008; Le Bail 2008).

According to Hawthorne and Sokolova (2002), the structures of Gordaite, Namuwite, and Bechererite are closely related as they all contain alternating sheets with octahedral and tetrahedral sites (homeomorphic to graph 4b of Hawthorne and Schindler (2000)). Figure 5.10 shows the generic structure for Gordaite and Namuwite. Zn occurs mainly in the center of the tetrahedrons and partly in the center of the octahedrons. Bechererite has six octahedrally coordinated cations, and every seventh

octahedron is vacant. Furthermore, two tetrahedrally coordinated Zn cations form a pyro-group leading to a very ordered structure of this mineral phase (Hawthorne and Sokolova 2002). Therefore, Bechererite can be excluded as an exchange product of Gordaite.

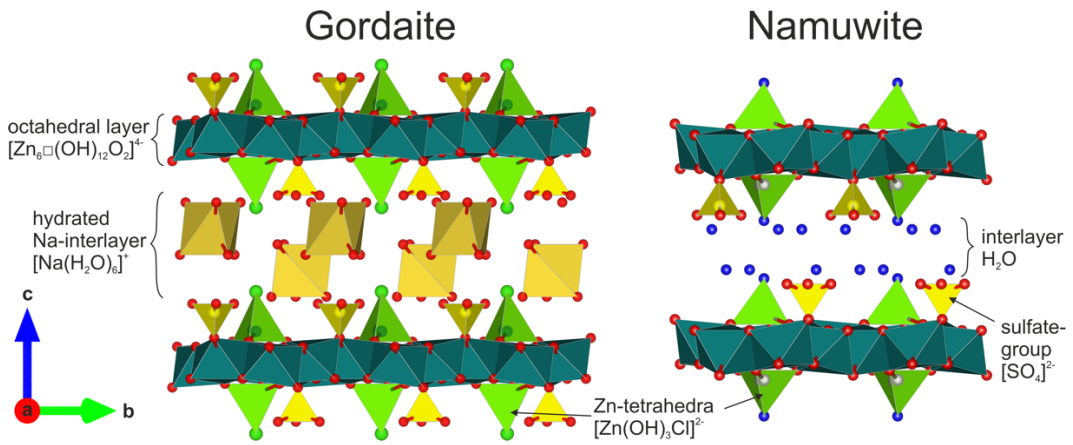

Figure 5.10: Structure of Gordaite (left, after Adiwidjaja et al. (1997)) and Namuwite (right, after Groat (1996)) along the c-axis; crystal structures were created with the software VESTA (Momma and Izumi 2011).

The sheet-like structures of Gordaite and Namuwite consist of alternating sheets with tetrahedral and octahedral sites. In Gordaite, Cl^- atoms (see Figure 5.10a, left) occupy the tip of the tetrahedron, resulting in a negative charge, which is balanced by incorporating Na^+-ions between the layers. The Na^+-ions are octahedrally coordinated, surrounded by six water molecules, and held by hydrogen bonds. This means that the intercalated Na^+ ions are weakly bonded between the sheets. The structure of Namuwite is comparable; it also has the sequence tetrahedron – octahedron – tetrahedron, connected via hydrogen bonds; but in contrast with Gordaite, it does not include Na^+ and Cl^- in the structure (see Figure 5.10, right). Therefore, we suggest that washing the precipitate with pure water removes the Na^+ ions from the structure. Without the missing charge, Cl^- in the tetrahedrons of Gordaite is substituted by OH^-. Rearrangement of the structure leads to the formation of low crystalline Namuwite. Our results show that, even at high salinity in the AQ, Gordaite may be transferred to Namuwite. After washing with pure water, the intensity of Gordaite reflexes slightly decreased, whereas that of Namuwite increased. This trend is in agreement with (Maruyama et al. 2017b). They detected small amounts of Osakaite ($Zn_4(SO_4)(OH)_6 \cdot 5H_2O$) in their synthesized residue. Drying at room temperature on air can lead to Namuwite, a partially dehydrated derivative of Osakaite.

5.2. Direct precipitation of ZnO from synthetic, saline AQ at temperatures ≤ 90 °C

5.2.1. Purpose, scope, and nomenclature

In this chapter, two methods are presented to achieve ZnO directly from synthetic saline AQ at temperatures ≤ 90 °C. Accordingly, two sets of experiments were carried out to show the effect of (a) the reaction temperature (Set 4) and (b) the alkalization rate (A) (Set 5) on the precipitation of phases.

Nomenclature: The experiments and the corresponding samples were named according to the following scheme. The first part in the nomenclature stands for the main element Zn. The second part is the reaction temperature in °C. Alkalization rate (A1, A2, A3) is on the 3rd position, with A1 > A2 > A3. When the residue is not washed, it is marked with "_uw". No suffix indicates that the residue is the fresh filtered precipitate, washed three times with deionized water (< 2 µS/cm) immediately after precipitation. For example, Zn_30 °C_A2 refers to the fresh, washed precipitate of the experiment with Zn in synthetic saline AQ, performed at a reaction temperature of 30 °C using the medium alkalization rate A2.

5.2.2. Experimental series (Set 4 and 5)

Set 4: Effect of reaction temperature

In Set 4, six experiments were performed to investigate the influence of the reaction temperature on the obtained precipitation products in the saline AQ. The reaction temperature was varied from 30 °C to 80 °C (Table 5.6). All experiments were alkalized with the medium alkalization rate A2. The reaction volume was 250 ml, except for experiment Zn_30 °C_A2, where the volume was 500 ml.

Table 5.6: Experimental Set 4 with varying reaction temperature.

Set	Experiment	Reaction-temperature [°C]	Alkalization rate A	Volume [ml]
4	Zn_30 °C_A2	30	A2	500
	Zn_40 °C_A2	40		250
	Zn_50 °C_A2	50		
	Zn_60 °C_A2	60		
	Zn_70 °C_A2	70		
	Zn_80 °C_A2	80		

Set 5: Influence of the alkalization rate (A)

The second experimental set (Set 5) was conducted to investigate the effect of alkalization rate (A) on the precipitation of phases from the saline AQ. Table 5.7 gives an overview of the experiments. Three different A´s were tested: fast A1 was carried out at 35 °C, medium A2 at 30 °C, and 60 °C with $ZnCl_2$

as educt and 250 ml reaction volume. The slow A3 was used at 60 °C and 90 °C, respectively. In this case, the reaction volume was 400 ml, and $ZnSO_4 \cdot 7H_2O$ was used as educt.

Table 5.7: Experimental Set 5 with different alkalization rates.

Set	Experiment	Reaction-temperature [°C]	Alkalization rate (A)	Volume [ml]	Zn-Educt
5	Zn_35 °C_A1	35	A 1	250	$ZnCl_2$
	Zn_30 °C_A2	30	A 2	250	$ZnCl_2$
	Zn_60 °C_A2	60			
	Zn_60 °C_A3		A 3	400	$ZnSO_4 \cdot 7H_2O$
	Zn_90 °C_A3	90			

5.2.3. Results

5.2.3.1. Temperature dependence (Set 4)

Water purification

Table 5.8 presents the Zn-concentrations in the filtrates of Set 4 experiments in dependence of reaction temperature at medium alkalization rate (A2) using 2000 – 2500 mg/l Zn as $ZnCl_2$ in a saline AQ and the calculated removal efficiencies. A high removal efficiency implies low Zn concentrations in solution and high Zn concentrations (enrichment) in the precipitate.

Table 5.8: Concentration in the filtrate and removal efficiencies of Zn in Set 4 in dependence of reaction temperature.

Sample	Zn initial [mg/l]	RSD [%]	Zn in filtrate [mg/l]	RSD [%]	Zn-removal efficiency [%]	RSD [%]
Zn_30 °C_A2	2561.8	6.0	20.5	5.0	99.2	7.8
Zn_40 °C_A2	2225.9	5.1	25.3	5.1	98.9	6.3
Zn_50 °C_A2	2007.6	1.5	20.9	3.7	99.0	7.7
Zn_60 °C_A2	2232.8	3.5	< 2	-	99.9	-
Zn_70 °C_A2	1984.0	4.7	< 2	-	99.9	-
Zn_80 °C_A2	1998.7	0.5	< 2	-	99.9	-

Low Zn concentrations (< 2 mg/l) were analyzed in the filtrates of the experiments with reaction temperatures ≥ 60 °C. This corresponds to a removal efficiency of 99.9 %. At lower reaction temperatures ≤ 50 °C, the removal efficiencies varied between 98.9 % (Zn_40 °C_A2) and 99.2 % (Zn_30 °C_A2). The highest Zn concentration in the filtrate (25.3 mg/l Zn) measured after the treatment process – and thus also the lowest Zn removal efficiency of 98.9 % – was obtained in experiment Zn_40 °C_A2, performed at 40 °C.

Mineralogical characterization of Set 4 phases

XRD results

In the unwashed samples of Set 4 is Halite (NaCl) the main phase. Comparing all unwashed samples shows that the relative intensity of Halite in the XRD pattern decreases with increasing reaction temperature. Figure 5.11 shows the effect of washing in comparison to an unwashed residue using Zn_40 °C_A2 as an example. The absence of Halite (COD-ID 9008678) in the washed sample shows that the water-soluble NaCl was completely removed by washing. This effect was observed in all diffractograms. Furthermore, in the unwashed sample, the Halite reflexes overlay those of the other phases. After washing the precipitate of experiment Zn_40 °C_A2, the main phase is Gordaite ($NaZn_4(SO_4)(OH)_6Cl{\cdot}6H_2O$), with main reflex (001) at 6.84° 2θ and related minor peaks (COD-ID 9011511). An additional peak appears at 8.53° 2θ that matches the main reflex (001) of Namuwite, $Zn_4(SO_4)(OH)_6{\cdot}4H_2O$ (COD-ID 9001719). Furthermore, three small peaks at 31.57° 2θ, 34.37° 2θ, and 36.13° 2θ are observed, that can be assigned to the main reflexes of ZnO (COD-ID 9011662).

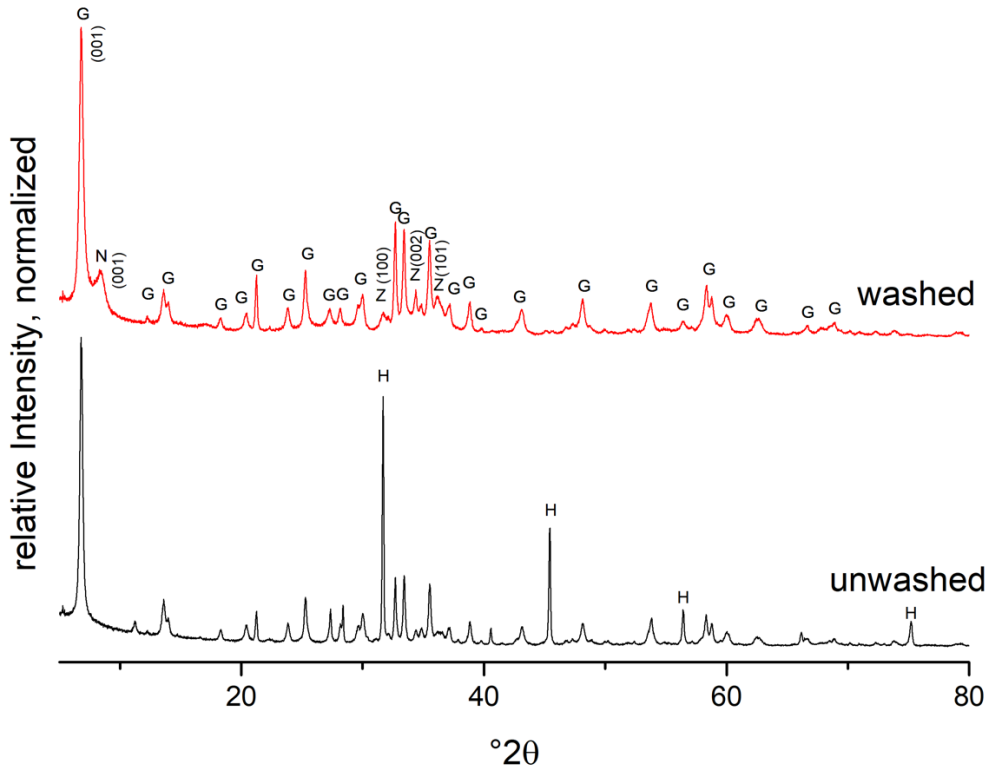

Figure 5.11: XRD pattern of the washed (red, upper) and the unwashed (black, lower) precipitates of sample Zn_40 °C_A2. G = Gordaite, N = Namuwite, Z = Zincite, H= Halite.

Figure 5.12 shows the XRD patterns of all washed, fresh precipitates from Set 4 experiments depending on reaction temperature (30 °C – 80 °C). In general, three phases can be observed: Gordaite, Namuwite, and Zincite. The phase assemblage in the samples changes systematically, depending on the reaction temperature.

At 30 °C, only Gordaite can be observed in the diffractogram, and no matching reflexes of Namuwite and ZnO were observed. In contrast, at 40 °C, all three phases, Gordaite, Namuwite, and Zincite, are present. The (001) reflex of Gordaite is broadened, and a hill at 8.53° 2θ matches the main reflex (001) of Namuwite, and small amounts of Zincite are indicated by the low intensity of the main reflexes. With a further increase of reaction temperature, the relative proportion of Gordaite decreases, while that of Zincite increases. At 50 °C, Zincite is the main phase, and at reaction temperatures of 60 °C and above, only Zincite can be detected. As shown in Figure 5.12, all peaks of the Zincite pattern are broad. With decreasing temperature from 80 to 40 °C, the width of the ZnO peaks increases slightly, and the relative intensity of the (002) ZnO main reflex at 34.37° 2θ increases too. At 80 °C, the (002) and (100) reflexes have equal relative intensity, whereas at 50 °C, the relative intensity of the (002) main reflex of ZnO is highest.

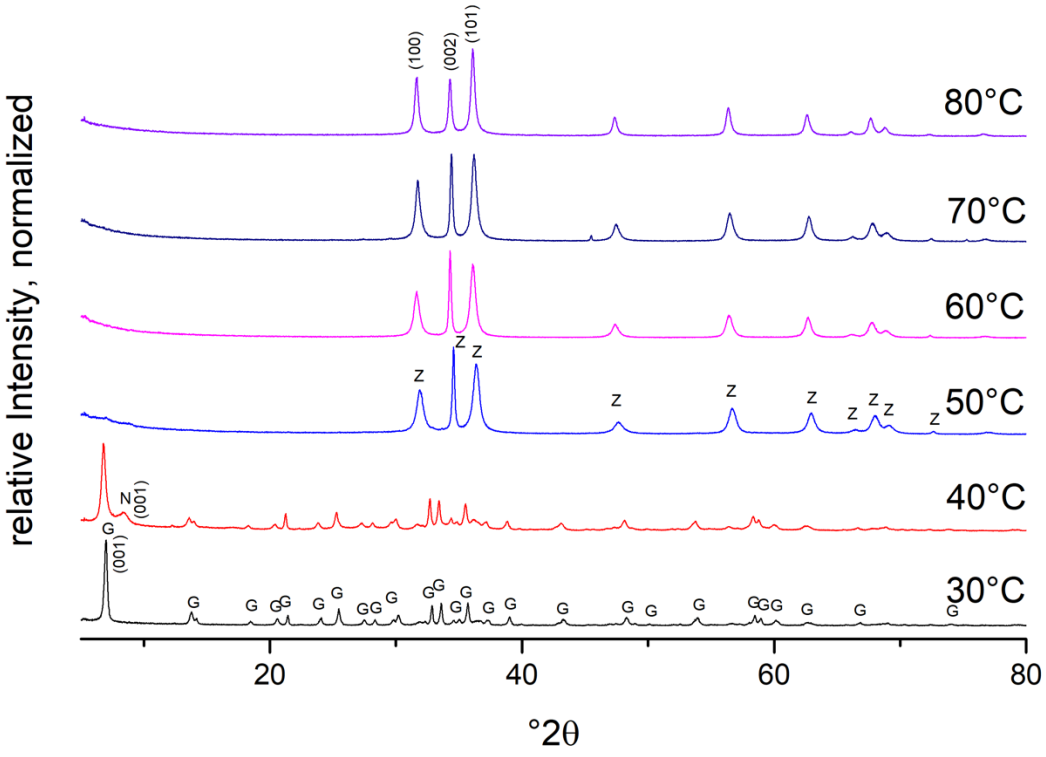

Figure 5.12: XRD pattern of the fresh washed precipitates from Set 4 with increasing reaction temperature from 30 to 80 °C; G = Gordaite, N = Namuwite, Z = Zincite.

FTIR spectroscopy

The phases of Set 4 determined by FTIR present the same trend in dependence of reaction temperature as already observed by XRD. As shown in Figure 5.13, at low temperatures ≤ 40° C, the fresh precipitates show band positions that can be assigned to Gordaite (Stanimirova et al. 2018). In addition, bands with low intensity at 669 cm^{-1}, 783 cm^{-1}, 955 cm^{-1}, and 1080 cm^{-1}can be assigned to Namuwite (Stanimirova et al. 2018), with other bands superimposed by Gordaite bands. All spectra show weak bands in the region of 3500 cm^{-1}, which match the O-H bands of Gordaite. With increasing reaction temperature, the intensity of the OH-bands decreases, and at 70 °C, they are no longer visible. At 40 °C (Zn_40 °C_A2), additional bands of low intensity indicate the presence of Zincite (Chukanov 2014). At reaction temperatures ≥ 50 °C, Zincite is the main phase of the FTIR spectra. Two very weak bands observed at 1400 cm^{-1} and 1501 cm^{-1} can be assigned to C-O bands of Hydrozincite, $Zn_5[(OH)_6|(CO_3)_2]$ (Prosek et al. 2007).

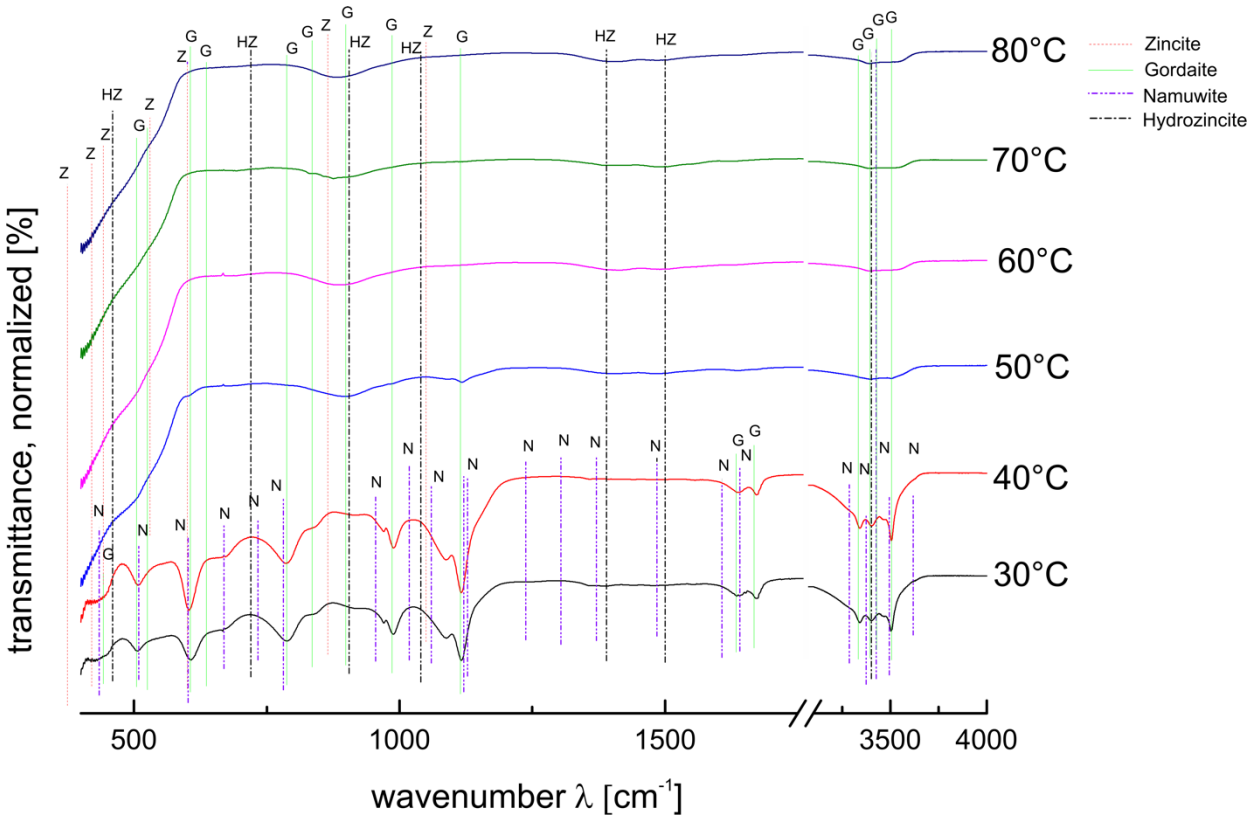

Figure 5.13: FTIR-spectra of fresh precipitates of experiments Set 4 in dependence of reaction temperature from 30 – 80 °C. G = Gordaite, N = Namuwite, Z = Zincite, HZ = Hydrozincite.

5.2.3.2. Dependence on alkalization rate (Set 5)

Water purification

Table 5.9 shows the initial Zn concentration in starting solution and that in the filtrate after the precipitation reaction of Set 5 as a function of the alkalization rate. It includes the calculated removal efficiencies of Zn.

Table 5.9: Zn concentration in filtrates and calculated removal efficiencies of Zn of Set 5, dependent on three different alkalization rates and temperatures.

Name	Initial Zn-concentration [mg/l]	RSD [%]	Zn in filtrate [mg/l]	RSD [%]	Zn-Recovery [%]	RSD [%]
Zn_35 °C_A1	1964.7	1.8	5.6	6.3	99.7	6.6
Zn_30 °C_A2	2561.8	6.0	20.5	5.0	99.2	7.8
Zn_60 °C_A2	2232.8	3.5	< 2	-	99.9	-
Zn_60 °C_A3	1837.9	0.5	36.0	2.0	98.0	2.1
Zn_90 °C_A3	1812.9	0.6	11.1	3.9	99.4	4.0

In general, in all experiments of Set 5, the Zn-removal efficiencies are above 99% with one exception: Experiment Zn_60 °C_A3 showed a Zn-removal efficiency of "only" 98.0 %. After the experiments, the Zn concentrations in the filtrates vary between < 2 mg/l Zn (experiment Zn_60 °C_A2) and 36.0 mg/l Zn (experiment Zn_60 °C_A3). It is noteworthy that these two distinctly different Zn concentrations were obtained in experiments performed at the same reaction temperature but with different alkalization rates. At a lower temperature (35° C) but significantly higher alkalization rate (A1), 5.6 mg/l Zn was detected in the filtrate after precipitation (Zn_35 °C_A1), corresponding to a removal efficiency of 99.7 %. In contrast, at the same alkalization rate, the removal efficiency increased with increasing reaction temperature, as shown by the following experiments: At a low alkalization rate (A3), the removal efficiency increased from 98 % at 60° C (Zn_60 °C_A3) to 99.4 % at 90 °C (Zn_90 °C_A3).

Mineralogical characterization of Set 5 phases

XRD results

The XRD pattern of the fresh precipitates from Set 5 show either Gordaite or Zincite as the main phase depending on the reaction conditions. As shown in Figure 5.14, at a slow alkalization rate (A3), Zincite was only observed at 90 °C (Zn_90 °C_A3). A broad hill at approx. 8.5 °2θ matches with the main peak of Namuwite. No other phases were detected in the diffractogram. In comparison, at the same alkalization rate and lower reaction temperature of 60 °C, Gordaite is the main phase (Zn_60 °C_A3).

With medium alkalization rate A2, only Zincite was observed at 60 °C (Zn_60 °C_A2), but not at 30 °C, where Gordaite is the main phase (Zn_30 °C_A2). At the fast alkalization rate (A1), Zincite was already detected at a reaction temperature of 35 °C (Zn_35 °C_A1).

The comparison of the XRD pattern Zn_35 °C_A1 over Zn_60 °C_A2 to Zn_90 °C_A3 shows that the peak width of Zincite increases with increasing temperature and decreasing alkalization rate. The intensity of the three main peaks of Zincite changes, too. In the experiments Zn_35 °C_A1 and Zn_90 °C_A3, the (101) reflex of Zincite is highest, while in the experiment Zn_60 °C_A2, the intensity of the (002) reflex is highest. This change in relative intensity of the ZnO main reflexes was also observed in Set 4.

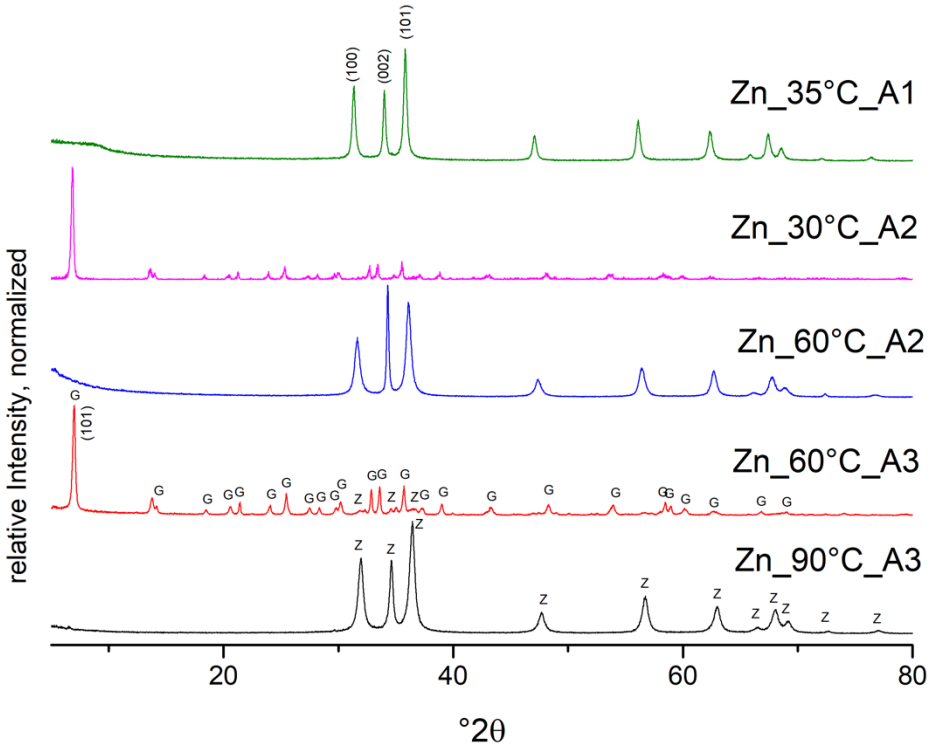

Figure 5.14: XRD pattern of Set 5 precipitates dependent on temperature and alkalization rate (A). G = Gordaite, Z = Zincite (ZnO).

FTIR Spectroscopy

A comparison of the FTIR spectra of Set 5 shown in Figure 5.15 confirms the results of the XRD. Zincite is the only phase detected by FTIR at 90 °C and slow A3 (experiment Zn_90 °C_A3). Under the same alkalization rate (A3) but 60 °C reaction temperature (experiment Zn_60 °C_A3), Gordaite is the main phase. At a medium alkalization rate (A2) and a reaction temperature of 60° C, ZnO is the main phase observed in the FTIR spectra. At A2 and 30 °C, however, Gordaite is the main phase. In the experiment performed at 35 °C and alkalized with the fast A1 (Zn_35 °C_A1), Zincite was identified as the main phase.

The FTIR spectra with ZnO as the main phase (experiments Zn_90 °C_A3, Zn_60 °C_A2, and Zn_35 °C_A1) show the following common features. Weak bands at 505 cm^{-1} and 525 cm^{-1} and around 3340 cm^{-1} – 3505 cm^{-1} indicate remains of Gordaite. Comparing these spectra shows that the Gordaite bands in the experiment Zn_35 °C_A1 have the lowest relative intensities. With increasing temperature and decreasing alkalization rate, the relative intensity of the absorption bands of Gordaite increases indicating a higher proportion of Gordaite. Weak bands at 1400 cm^{-1} and 1501 cm^{-1} observed in the experiments Zn_35 °C_A1 and Zn_60 °C_A2 are assigned to Hydrozincite. These bands were not observed in experiment Zn_90 °C_A3.

In the two experiments with Gordaite as the main phase, the proportion of Gordaite is higher in experiment Zn_60 °C_A3 than in experiment Zn_30 °C_A2. Additional bands at 669 cm^{-1}, 783 cm^{-1}, 955 cm^{-1}, and 1080 cm^{-1} match with the band maxima for Namuwite; the other bands of Namuwite are superimposed by Gordaite.

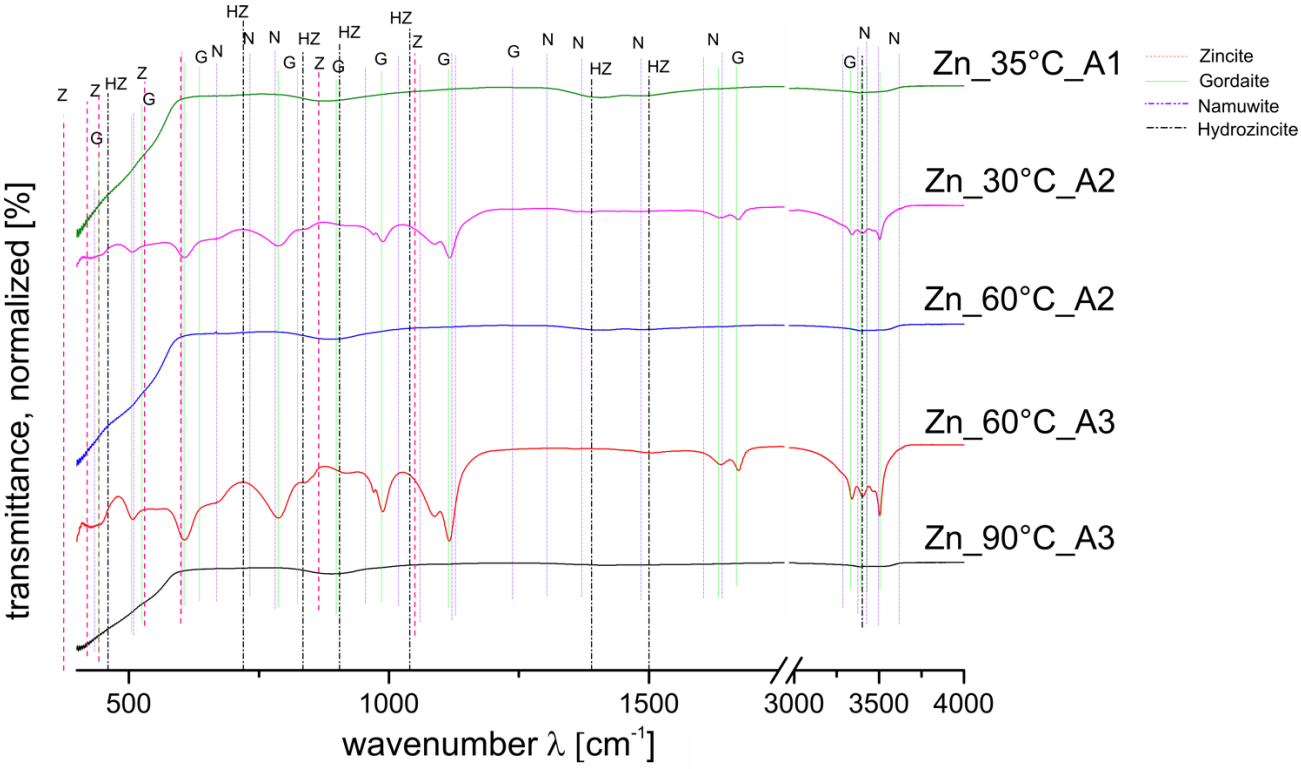

Figure 5.15: FTIR spectra of Set 5 with increasing alkalization rate and decreasing reaction temperature. G = Gordaite, N = Namuwite, Z = Zincite (ZnO), HZ = Hydrozincite.

5.2.4. Discussion

5.2.4.1. Effect of the reaction temperature

Figure 5.16a gives an overview of the water analysis results of Set 4 in dependence of the reaction temperature at constant alkalization rate (A2), including the RSD in mg/l, and Figure 5.16b shows the calculated removal efficiencies. Two different ranges can be observed: at temperatures ≤ 50 °C, Zn-concentrations decrease from about 2000 mg/l to values between 20 and 25 mg/l; this corresponds to a removal efficiency of 99.0 ± 0.2 %. At temperatures ≥ 60 °C, the concentrations are consistently below the detection limit (< 2 mg/l; green dashed line in Figure 5.16a), corresponding to a removal efficiency > 99.9 %.

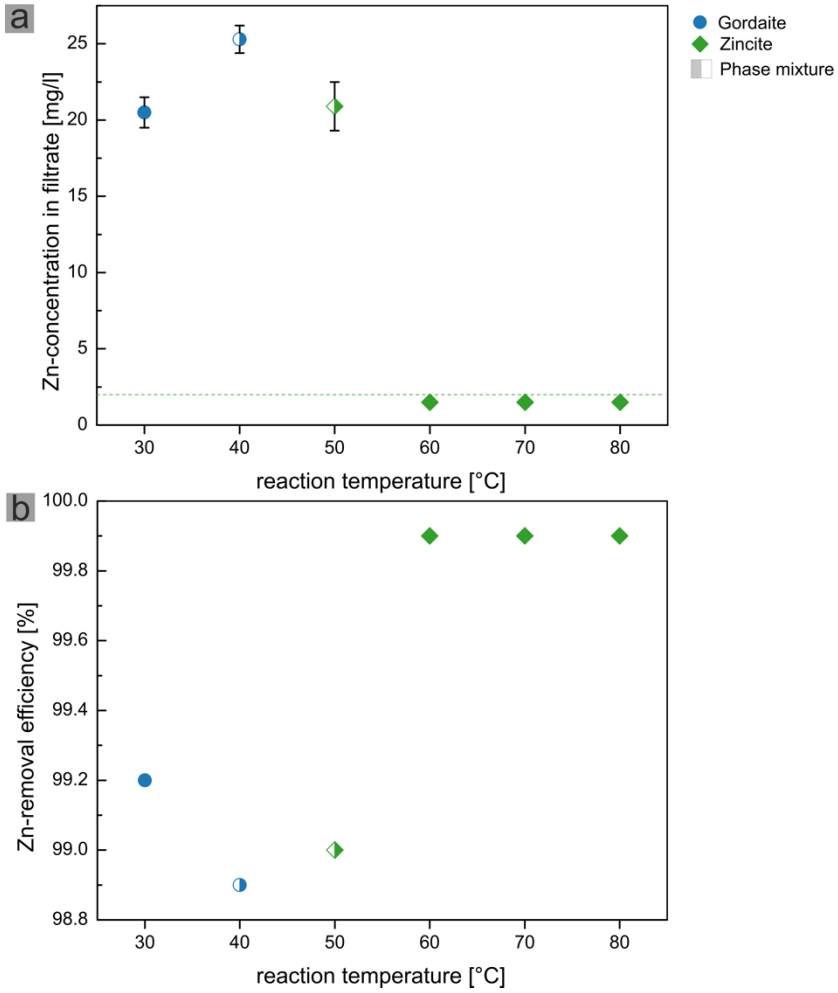

Figure 5.16: a) Zn concentration in filtrate including RSD in mg/l in dependence of reaction temperature (Set 4); the green symbols ≥ 60 °C were inserted to visulaize that the concentration was below detection limit of 2mg/l. b) Magnification of the corresponding removal efficiency in the range 98.8 – 100%. The color of the symbols indicates the main phases in the precipitates, blue for Gordaite, green for Zincite. Half-filled symbols point to phase mixtures with the color of the main phase.

ZnO was successfully synthesized directly from synthetic saline solution at temperatures ≤ 90 °C. The overview of the phases observed after washing the precipitates shows a clear systematic trend as a function of temperature. As shown in Figure 5.17, pure Gordaite occurs at 30 °C. Between 30 °C and 60 °C, the amount of Gordaite decreases continuously. In comparison, the Zn-concentration in the filtrate remains relatively high. The results for Gordaite correspond to the study of Tandon et al. (2018), observing Gordaite at high saline AQ and 30 °C reaction temperature, with a slightly higher removal efficiency for Zn (99.8 %). John et al. (2016d) and Tandon et al. (2018) studied ZnO precipitation in SO_4 containing solutions. They observed high removal efficiencies for ZnO (> 99.9 %) at 40 °C, indicating that ZnO can be formed at lower temperatures in a chloride-poor environment.

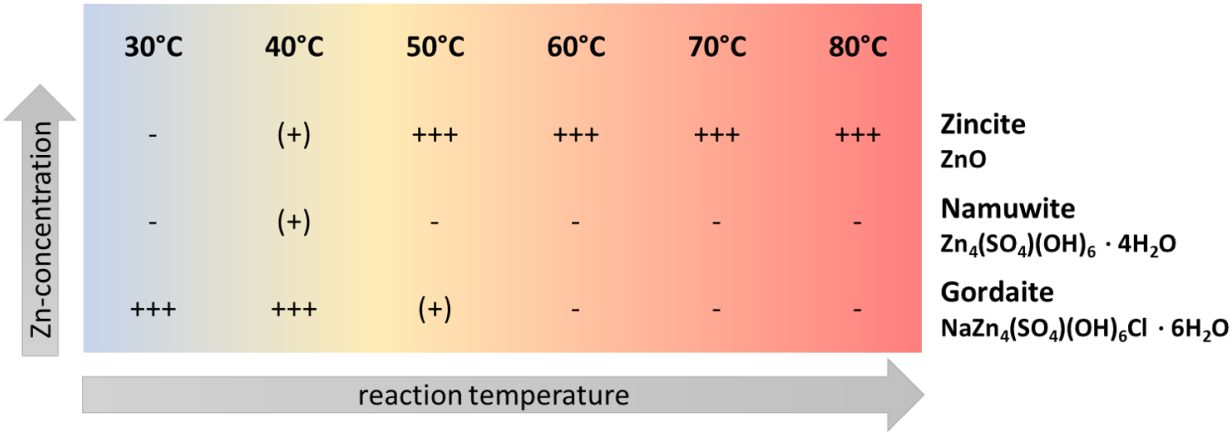

Figure 5.17: Overview of the phases formed as a function of reaction temperature after washing the precipitates from Set 4. +++ = high relative proportion, (+) = traces of the phase, - = not detected.

The abrupt drop of the Zn-concentration in the filtrate at temperatures ≥ 60 °C correlates with the formation of Zincite as the main phase, shown by the XRD pattern. Gordaite/Namuwite can only be detected in the FTIR spectra, indicating that they occur only in traces. Based on the observations, the presence of both phases, Zincite and Gordaite, within the temperature range 40 - 50 °C brackets the stability boundary between Gordaite and Zincite in saline AQ.

The broad shape of the ZnO peaks in the XRD pattern indicates that the synthesized ZnO is nanocrystalline. The change in the intensity ratio of the ZnO main peaks in dependence of temperature points to a change in the preferred orientation of the nanocrystals (Holder and Schaak 2019). This effect indicates a change in morphology from needle-like at 50 °C to platy crystals at 80 °C. John et al. (2016d) also observed the peak broadening and a changed intensity ratio of ZnO main peaks during the synthesis of ZnO from chloride-free solutions.

5.2.4.2. Effect of alkalization rate (A)

Figure 5.18a presents the Zn concentrations in the filtrates determined for Set 5, including the RSD in mg/l, and the calculated removal efficiencies are in Figure 5.18b. It shows the effect of the alkalization rate (A) and reaction temperature on the one hand and the precipitated main phases on the other. As already observed in Set 4, the RSD of Zn value analyzed in a highly saline AQ is high for analytical reasons.

Set 5 shows the same trend as Set 4: with Gordaite as the main phase, the Zn concentration in the filtrate is higher than 20 mg/l, which leads to a comparably lower removal efficiency for Zn (98.0 % and 99.2 %). On the contrary, when Zincite precipitates, the Zn concentrations in the filtrate are lower (< 11.1 mg/l), which corresponds to a higher yield (≥ 99.4 %), with the best result for the reaction temperature 60 °C and A2. Furthermore, the results show that the alkalization rate has a decisive influence on the removal efficiency of Zn. Increasing the alkalization rate from slow (A3) to a medium rate (A2) has the effect of decreasing the Zn concentration below the detection limit, which corresponds to a removal efficiency of > 99.9 %.

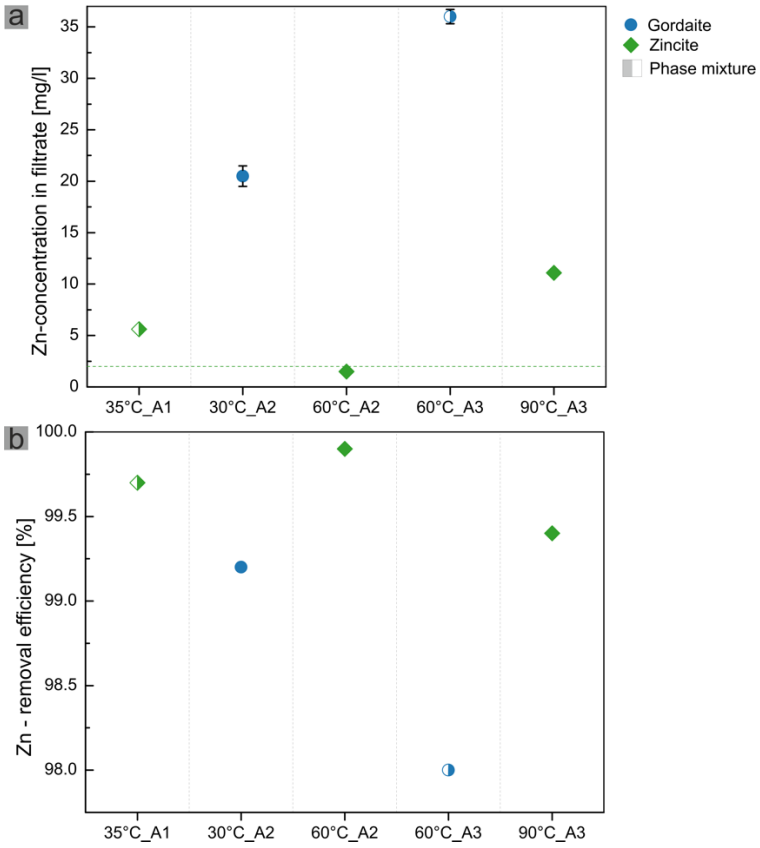

Figure 5.18: a) Zn-concentration in the filtrate of Set 5 in dependence of alkalization rate and RSD in mg/l. If no error bars are displayed, the RSD is within the size of the symbol; b) the corresponding removal efficiency in the range 97.5 – 100 %. The colors indicate the precipitated main phase, Gordaite (blue), ZnO (green), and phase mixtures, which are half-filled with the respective color of the main phase.

Figure 5.19 presents the results of the mineralogical characterization of Set 5 precipitates, with the area of successful ZnO synthesis. It clearly shows a systematic relationship between ZnO formation, reaction temperature, and alkalization rate: At a low alkalization rate (A3), the formation of ZnO requires high reaction temperatures (90 °C). By increasing the alkalization rate, the ZnO formation shifts to lower temperatures. Our experiments show that ZnO can also be synthesized from salt-rich solutions at temperatures < 40 °C, whereby the reaction kinetics is the decisive factor for successful synthesis. With a fast A1 and 8M NaOH, ZnO is already the dominant product phase at 35 °C. This means that the process is not only dependent on the temperature, as additional parameters have to be considered. Similar results were obtained by John et al. (2016d) where they performed the experiments with an SO_4 rich solution. They achieved Zincite with a high yield (> 99.9 %) already at 40 °C using a fast alkalization rate and 4M NaOH at saline poor conditions.

This study clearly shows that Gordaite is the stable phase in saline environments and at low temperatures (≤ 40 °C). The small amounts of low crystalline Namuwite are suggested to be the result of washing out Na^+ and Cl^- from the structure of remanent Gordaite. This phenomenon was already observed by Tandon et al. (2018). By using a high alkalization rate, it is possible to gain Zincite at low temperatures. The reaction kinetics plays a significant role for the reaction yield / removal efficiency: For both, Zincite and Gordaite, experiments with a slow alkalization rate (A3) lead to low removal efficiencies. For example, the experiment Zn_60° C_A3 with Gordaite as the main phase and traces of Zincite has the lowest removal efficiencies. Comparing all the experiments with Zincite as the main phase, the experiment at 90 °C but with slow A3 (Zn_90 °C_A3) achieved the lowest removal efficiency (99.4%).

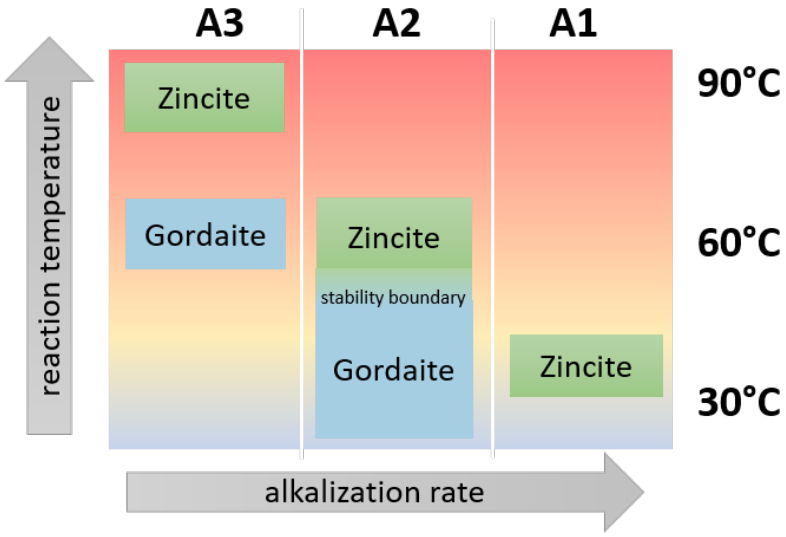

Figure 5.19: Summary of the main phases of Set 5 in dependence of reaction temperature and alkalization rate (A). The experimentally determined stability boundary when using alkalization rate A2 between Gordaite and Zincite is displayed, too.

5.2.4.3. Reaction mechanisms for the direct synthesis of Zincite and Gordaite

The comparison of the washed and unwashed samples shows that NaCl is the only water-soluble salt in the highly saline AQ. The decrease in Halite peak intensity in the XRD patterns of the unwashed samples indicates increasing solubility of Halite in the solution with increasing reaction temperature. At 40 °C, in addition to Gordaite, traces of ZnO were detected in the washed sample, which was presumably already present before washing but could not be detected due to the overlap of the ZnO peaks with those of Halite with significantly higher intensity in the XRD pattern.

Several studies investigated the formation of Zincite (ZnO) and Gordaite. Generally, the formation of Gordaite requires a salt-rich aqueous solution. Leal et al. (2020) synthesized Gordaite according to the methods already described in the literature (Stanimirova et al. 2017; Maruyama et al. 2017a; Maruyama et al. 2017b) by using 1g ZnO powder mixed with a solution made of 15 ml (1.5 Mol/l) NaCl and 15 ml (0.5 Mol/l) $ZnSO_4$. The suspension was stirred for 120h, centrifuged, washed with deionized water, and dried at room temperature in a desiccator. Considering several studies (Chen et al. 2006; Mouanga and Berçot 2010; Vera et al. 2013), the authors proposed the following reaction mechanism. They supposed the formation of Zn-hydroxide $Zn(OH)_2$ as intermediate phase, which reacts in the presence of Na^+ and Cl^- ions in the solution and at a ratio of $Cl^- > SO_4^{2-}$ to the next intermediate phase Simonkolleite $Zn_5(OH)_8Cl_2 \cdot H_2O$, according to the equations (5.1) and (5.2). In the presence of Na^+ and SO_4^{2-}, Simonkolleite reacts to Gordaite (equation 5.3).

(5.1) $$Zn^{2+} + 2OH^- \leftrightarrow Zn(OH)_2$$

(5.2) $$5Zn(OH)_2 + 2Cl^- + 2H_2O \leftrightarrow Zn_5(OH)_8Cl_2 \cdot H_2O + 2OH^-$$

(5.3) $$4Zn_5(OH)_8Cl_2 \cdot H_2O + 5SO_4^{2-} + 5Na^+ + 26H_2O \leftrightarrow 5NaZn_4(SO_4)(OH_6)Cl \cdot 6H_2O + 3Cl^- + 2OH^-$$

In our study, the synthesis of Gordaite from the saline AQ occurs in less than 10 minutes. This argues for direct precipitation of Gordaite without intermediate phases like $Zn(OH)_2$ or Simonkolleite, according to equation (5.4):

(5.4) $$4Zn^{2+} + 8Cl^- + 8Na^+ + 8OH^- + SO_4^{2-} + 6H_2O \leftrightarrow NaZn_4(SO_4)(OH_6)Cl \cdot 6H_2O + 7NaCl \downarrow + 2OH^-$$

Similarly, for the synthesis of Zincite from Cl-rich media, the formation of intermediate phases such as zinc hydroxide, zinc carbonate, or layered zinc hydroxide chlorides have been postulated. Samanta and Mishra (2013) proposed the following reaction mechanisms: during the alkalization of the $ZnCl_2$ solution, $Zn(OH)_2$ first precipitates according to equation (5.5), which is converted to ZnO upon further alkalization, according to equations (5.6) - (5.8). Note, equation (5.5) was stoichiometrically corrected.

(5.5) $$ZnCl_2 + 2NaOH + H_2O \leftrightarrow Zn(OH)_2 \downarrow + 2NaCl \downarrow + H_2O$$

(5.6) $$Zn(OH)_2 + 2H_2O \leftrightarrow Zn^{2+} + 2OH^- + 2H_2O$$

(5.7) $$Zn^{2+} + 2OH^- + 2H_2O \leftrightarrow Zn(OH)_4^{2-} + 2H^+$$

(5.8) $$Zn(OH)_4^{2-} \leftrightarrow ZnO + H_2O + 2OH^-$$

Thomas et al. (2012) investigated the corrosion of Zn in marine environments by placing a ground Zn-alloy (99.99% pure Zn) in a 0.1 M NaCl solution and adjusting the pH accordingly. The authors also used the above equations (5.5) - (5.8) to describe the formation of ZnO.

Samanta and Mishra (2013) used very high Zn concentrations and an elaborate process to synthesize ZnO from solutions containing similar Cl-concentrations. Their synthesis products were annealed in an oven at 150 °C for more than 2 hours. In contrast, our experiments for ZnO synthesis took less than 10 minutes. Furthermore, the mineralogical characterization of the fresh precipitates showed no evidence of the formation of $Zn(OH)_2$ as an intermediate precipitation product. This suggests that the tetrahydroxozincate ions $[Zn(OH)_4]^{2-}$ are formed directly after alkalization of the Zn-solution and immediately react to form ZnO. Therefore, we propose an alternative formation mechanism for ZnO according to equations (5.9) and (5.10):

(5.9) $$Zn^{2+} + 2Cl^- + 2Na^+ + 2\,OH^- + 2H_2O \leftrightarrow Zn(OH)_4^{2-} + 2H^+ + 2Cl^- + 2Na^+$$

(5.10) $$Zn(OH)_4^{2-} + 2Cl^- + 2Na^+ + 2H^+ \leftrightarrow ZnO \downarrow + 2NaCl \downarrow + 3H_2O$$

Our results clearly show that in the presence of Na^+, Cl^-, and SO_4^{2-} and under the same reaction conditions (pH and temperature), both ZnO and Gordaite can precipitate (Figure 5.20). At low temperature and saline conditions, Gordaite is the stable phase. At a higher reaction temperature, the equilibrium shifts in favor of ZnO, even in a chloride-rich environment. This is confirmed by our results from Set 4, with the precipitation of ZnO at T ≥ 60 °C from the saline AQ. The occurrence of the two phases between 40 - 60 °C is evidence that the stability boundary between these two phases lies within this temperature range (see Figure 5.19). The significantly lower removal efficiency of Zn observed in the experiments of Sets 4 and 5 in the presence of both phases indicates a slow transformation rate from Gordaite to Zincite. Additionally, the Zn concentrations are with > 20 mg/l consistently elevated when Gordaite is part of the precipitate compared to when ZnO precipitates (Zn < 2 mg/l). This suggests that Gordaite has a higher solubility in the saline AQ than Zincite.

These observations point to a solution-precipitation reaction mechanism, as Gordaite must first be dissolved to form Zincite. One argument is the different structure of these phases: In Zincite, the coordination environment of the Zn ion is tetrahedral, whereas in Gordaite, it mainly consists of edge-shared $Zn(OH)_6$ octahedra (Adiwidjaja et al. 1997). Another argument for this is the specific

reaction of Gordaite to changes in the environment. There is strong evidence that washing the precipitates apparently influences the Gordaite structure. Our study showed that at 40 °C, Na^+ and Cl^- ions can be partially removed from the Gordaite structure by washing the precipitate, as evidenced by traces of low crystalline Namuwite identified by the broad main peak at 8.53° 2θ. Tandon et al. (2018) have also observed this effect at 40 °C reaction temperature. They suggested that Na^+ and Cl^- removal from the Gordaite was caused by the concentration gradient during washing the filtered precipitate with pure water, resulting in a low crystalline Namuwite (Tandon et al. 2018).

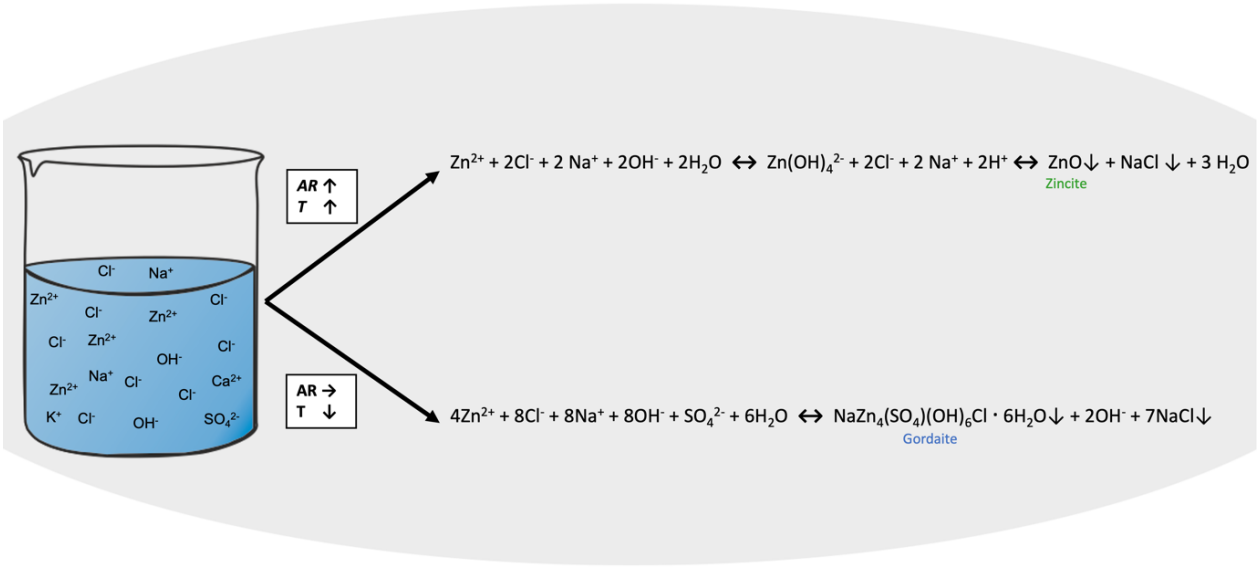

Figure 5.20: Precipitation of Zincite (ZnO) and/or Gordaite ($NaZn_4(SO_4)(OH)_6Cl{\cdot}6H_2O$) from the saline solution depending on temperature and alkalization rate.

This process can be explained by comparing the structures of these phases. As shown in Figure 5.21, Gordaite has a layered crystal structure whose main building unit is a brucite-like octahedral hydroxide layer with Zinc in the center. The sulfate groups are interconnected with the octahedral layer by substituting 1/7 of the hydroxide atoms with oxygen atoms giving the structural unit of $[Zn_6\square(OH)_{12}O_2]^{4-}$, which means every 7. octahedral site is vacant. On top and bottom of the vacancies are $[Zn(OH)_3Cl]^{2-}$ tetrahedrons located, connected to three OH-groups of the octahedral layer, and contain a Cl^--ion on the apex of the Zn-tetrahedron. In consequence, the hydroxide layers are negatively charged. This negative charge is neutralized by incorporating Na^+ -ions with a hydrate shell $[Na^+(H_2O)_x]$ between the hydroxide layers. The hydroxide layers are connected by a strong hydrogen bonding system (Adiwidjaja et al. 1997).

Namuwite has the same sheet-like structure as Gordaite with one difference; it has H_2O-molecules instead of Cl^- on the apexes of the Zn-tetrahedra, and in consequence, Na is not needed to balance the charge. Accordingly, in a more water-rich environment, the Gordaite structure reorganizes to form Namuwite.

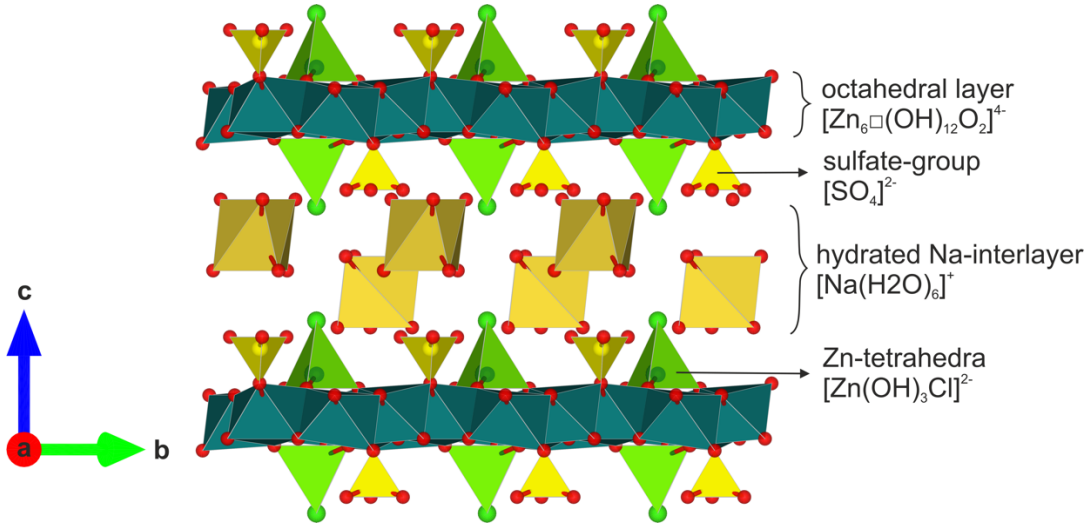

Figure 5.21: Crystal structure of Gordaite in b-c projection. Structure after Adiwidjaja et al. (1997). The crystal structure is created using the software VESTA 3 (Momma and Izumi 2011).

The consistency of our observation across the different experimental approaches confirms that Gordaite is the stable structure at temperatures < 40 °C. At 40 °C and above, the transformation to Namuwite is favored by the facile removal of Na^+ and Cl^- from the Gordaite structure during washing. This conclusion is consistent with the recent study of Stanimirova (2019), who also found that washing Gordaite with pure water forms different types of zinc hydroxy sulfates, including Namuwite. Stanimirova (2019) explained it by an "exchange mechanism, where together with the interlayer cations the halide anions leave the interlayer space." Stanimirova (2019) concluded that the interaction between the Cl-ion and the interlayer Na-cation must be stronger than the interaction with the Zn^{2+}-ion in the Zn-tetrahedra. The author suggests that this coupled cation-anion exchange reaction of H_2O with Na and Cl depends on the amount of H_2O used for washing. A ratio of Gordaite : H_2O = 2:1 during washing leads to Namuwite formation.

In another work, Stanimirova et al. (2016) studied the thermal decomposition of Zn-hydroxy sulfate minerals, including Gordaite, between 20 – 1000 °C. They observed a selective broadening of the (001) reflex of Gordaite at 180 – 200 °C and attributed that to partial dehydration of the $[Na^+(H_2O)_x]$ groups. The authors explain it with the removal of H_2O molecules from the Gordaite structure with increasing temperature. At first, the interlayer H_2O molecules, linking the octahedral hydroxide sheets via hydrogen bonds, are lost, resulting in a turbostratic disorder of the layers against each other. This phenomenon was also observed at 180 °C by Delcheva et al. (2019), who studied the thermal stability

of well-crystallized Br-Gordaite $NaZn_4(OH)_6(SO_4)Br{\cdot}6H_2O$, synthesized at room temperature. The turbostratic disorder described by Stanimirova (2019) and Delcheva et al. (2019) can apparently occur as early as 40 °C. Correspondingly, we observed a selective broadening of the (001) reflex of Gordaite at 40 °C after washing in the XRD pattern of samples Zn_30_A2 and Zn_40_A2 from Set 1 with Gordaite as the main phase, while this effect does not occur at 30 °C. Gordaite precipitation at 40 °C leads to disturbed and partially dehydrated $[Na^+(H_2O)_x]$ interlayer sheets. In consequence, Na^+ can be easily removed from the disturbed layers of Gordaite. Removal of Cl^- coupled with the exchange of the cations with H_2O leads to low crystalline Namuwite.

5.3. Precipitation of ZnO from synthetic, saline AQ by aging

5.3.1. Purpose, scope, and nomenclature

The central topic in this chapter is to synthesize ZnO from the saline AQ by aging the suspension. Gordaite will be educt for the aging experiments and was synthesized according to the procedure in chapter 5.2. Following, the effect of aging time (Set 6) and aging temperature (Set 7) will be presented.

All experiments were performed using $ZnCl_2$ as educt in high saline AQ. Conditions for Gordaite precipitation were 30 °C reaction temperature and medium alkalization rate A2. After precipitation, the samples were aged by filling 100 ml of the suspension into a closed vessel directly after the precipitation and then aging the suspension at the respective conditions of Set 6 or 7. All precipitates were filtered and washed three times with deionized water (< 2 µS/cm).

Nomenclature: In this chapter, the first part in the nomenclature stands for the main element Zn. The second part is the reaction temperature in °C, followed by the alkalization rate (A). The suffix indicates the aging conditions of the suspension, f for the fresh precipitate that was taken immediately at the end of the experiment, or the aging time in hours (h) followed by the aging temperature in °C (RT = room temperature).

For example, Zn_30 °C_A2_24h_110 °C refers to the washed precipitate of the experiment with Zn in synthetic saline AQ, performed at a reaction temperature of 30 °C using medium alkalization rate A2. After the experiment, the suspension was aged in a closed vessel for 24 hours at 110 °C.

5.3.2. Experimental series (Sets 6 and 7)

<u>Set 6: Influence of aging time</u>

Set 6 consists of 8 samples to study the effect of aging time on ZnO formation using Gordaite as educt. After Gordaite precipitation, the suspension was divided. Preliminary experiments showed that the transformation of Gordaite to Zincite occurs within 6 h. Therefore, seven samples were aged in 1 h steps from no aging (f) to 6 h. In addition, one sample was aged for 24 h at 110 °C (Table 5.10).

Table 5.10: Set 6 with varying aging time at 110 °C.

Set	Experiment	Aging-temperature [°C]	Aging-time [h]
6	Zn_30 °C_A2_f	110	no aging
	Zn_30 °C_A2_1h_110 °C		1
	Zn_30 °C_A2_2h_110 °C		2
	Zn_30 °C_A2_3h_110 °C		3
	Zn_30 °C_A2_4h_110 °C		4
	Zn_30 °C_A2_5h_110 °C		5
	Zn_30 °C_A2_6h_110 °C		6
	Zn_30 °C_A2_24h_110 °C		24

Set 7: Influence of aging temperature

In Set 7, seven suspensions with Gordaite were prepared and aged 24h at different temperatures, starting at room temperature (RT) and varying from 70 °C to 110 °C in 10 °C steps (Table 5.11). The effect of stirring (_stir) the suspension during aging was investigated with an additional sample aged at 70 °C.

Table 5.11: Set 7 with varying aging temperature after aging for 24 h.

Set	Experiment	Aging-temperature [°C]	Aging-time [h]
7	Zn_30 °C_A2_24h_RT	RT	24
	Zn_30 °C_A2_24h_70 °C	70	
	Zn_30 °C_A2_24h_70 °C_stir	70 *	
	Zn_30 °C_A2_24h_80 °C	80	
	Zn_30 °C_A2_24h_90 °C	90	
	Zn_30 °C_A2_24h_100 °C	100	
	Zn_30 °C_A2_24h_110 °C	110	

* = stirred during aging.

5.3.3. Results

5.3.3.1. Results of Set 6 in dependence of aging time

Water purification

Table 5.12 shows the Zn-concentration in the filtrates of the Set 6 experiments in dependence of aging time at 110 °C and the calculated removal efficiencies. The experiments were performed with medium alkalization rate A2 using 2000 - 2500 mg/l Zn as $ZnCl_2$ in a saline AQ.

Table 5.12: Initial concentration, concentration in the filtrate, and removal efficiencies of Zn of Set 6 in dependence of aging time at 110 °C.

Name	Zn initial [mg/l]	RSD [%]	Zn in filtrate [mg/l]	RSD [%]	Zn-removal efficiency [%]	RSD [%]
Zn_30 °C_A2_f	2561.8	6.0	20.5	5.0	99.2	7.8
Zn_30 °C_A2_1h_110 °C	2144.4	1.7	158.7	2.8	92.6	3.3
Zn_30 °C_A2_2h_110 °C	2561.8	6.0	162.9	1.9	93.6	6.3
Zn_30 °C_A2_3h_110 °C	2561.8	6.0	163.8	3.1	93.6	6.8
Zn_30 °C_A2_4h_110 °C	2561.8	6.0	177.4	6.4	93.1	8.8
Zn_30 °C_A2_5h_110 °C	2561.8	6.0	176.7	1.4	93.1	6.2
Zn_30 °C_A2_6h_110 °C	2561.8	6.0	176.6	1.6	93.1	6.2
Zn_30 °C_A2_24h_110 °C	2561.8	6.0	199.4	1.9	92.2	6.3

After Gordaite precipitation at 30 °C using medium A2, the concentration in the filtrate of sample Zn_30 °C_A2_f decreased from initially 2562 mg/l to 20.5 mg/l. Already after aging Gordaite for 1 h at 110 °C, the Zn concentration in the filtrate was higher than 150 mg/l. Even taking into account the (relatively high) RSD, an increase in Zn concentration with increasing aging time is observable. After 24 h aging at 110 °C, the highest Zn concentrations were measured in the filtrate with 199.4 mg/l Zn. Accordingly, the calculated Zn-removal efficiencies of the aged samples decrease to 92.2 % – 93.6 % compared to the fresh sample with 99.2 %.

Mineralogical characterization of Set 6 phases

XRD results

Figure 5.22 shows the XRD patterns of the fresh and of the aged precipitates of Set 6 tempered at 110 °C in dependence of aging time. Without aging, as a fresh precipitate, Gordaite is the only phase observed in the diffractogram, with the main peak at 6.84 °2θ (COD-ID 9011511). Already after one hour of aging at 110 °C, two main phases can be observed: Gordaite and Zincite. After 1 h aging, the intensity of all Gordaite reflexes decreased while the main reflex (001) was broadened. The three distinctive reflexes at 31.57 °2θ, 34.47 °2θ and 36.13 °2θ indicate Zincite (COD-ID 9011662) as the main

phase. In addition, a small hill at 8.53 °2θ matches the main reflex (001) of Namuwite (COD-ID 9001719). After 3 h aging, in sample Zn_30 °C_A2_3h_110 °C, only Zincite can be detected, and no Gordaite is present in the XRD pattern. This observation also applies to all samples that have been aged for more than 3 h at 110 °C. Only in the sample Zn_30 °C_A2_24h_110 °C, which was aged for 24 h, a small hill at 6.84 °2θ can be seen at high magnification of the XRD pattern, which can be assigned to the main reflex (001) of Gordaite. The ZnO peaks in all diffractograms are broadened, and the intensity of the ZnO (002) reflex at 34.37 °2θ is lower than the reference.

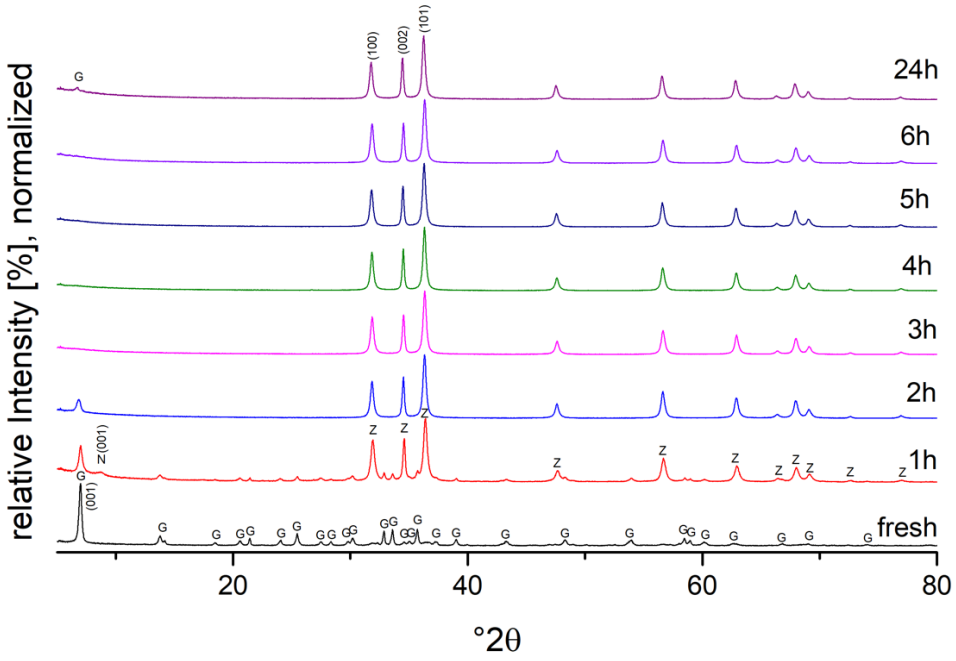

Figure 5.22: XRD pattern of the washed fresh precipitates of Set 6 and those aged at 110 °C with aging times from 1h up to 24h; G = Gordaite, Z = Zincite.

FTIR spectroscopy

The phases determined for Set 6 by FTIR support the results observed by XRD. As shown in Figure 5.23, the band positions of the fresh precipitate and the precipitate aged for 1 h at 110 °C can be assigned to Gordaite (Stanimirova et al. 2018). After one hour of aging, additional bands are observed where the positions match Zincite (Chukanov 2014). With aging time, the intensity of Gordaite bands in the FTIR spectra decrease. From 3 h onwards, only bands with low intensity in the range of 3500 cm^{-1} are observed, corresponding to the O-H bands of Gordaite. Partially, no bands could be assigned to Gordaite, as observed in the case of sample Zn_30 °C_A2_6h. In addition to the Gordaite and Zincite bands, the fresh sample, as well as the sample that was aged for 1 h, show bands of low intensity, which can be assigned to Namuwite (Stanimirova et al. 2018). Namuwite can be identified by the band positions at 669 cm^{-1}, 783 cm^{-1}, 955 $cm^{-1,}$ and 1080 cm^{-1}, which are not superimposed by Gordaite bands.

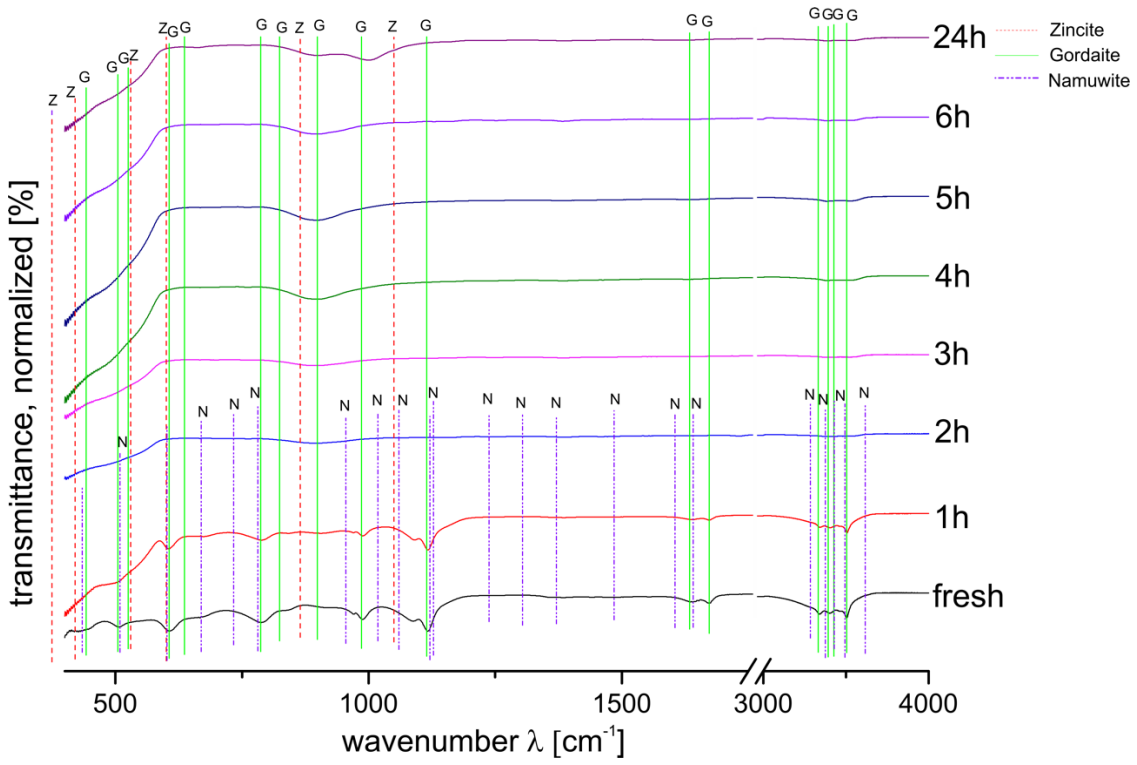

Figure 5.23: FTIR-spectra of the washed precipitates from Set 6 tempered at 110 °C in dependence of aging time varying between zero (fresh) up to 24h. G = Gordaite; N = Namuwite; Z = Zincite.

Scanning electron microscopy (SEM)

Figures 5.24a-d show SEM images of fresh Gordaite and the precipitates after an aging period of 1 h, 6 h, and 24 h at 110 °C. The fresh precipitates (Figure 5.24a) consist of thin, platy hexagonal crystals, typical for Gordaite. The idiomorphic crystals with sizes of 1- 2 µm have a smooth surface and sharp edges. According to the EDX-measurements, fresh precipitates contain Zn, Na, S, Cl, and O. The Cl/S-ratio of 1:1 corresponds to the Cl/S ratio in Gordaite. Small stalky aggregates of some nm size can be seen isolated on the surface of the Gordaite crystals, which couldn't be identified further. After 1 h aging (Figure 5.24b), the shape of Gordaite changes, as only a few platy and strongly rounded crystals are present with sizes < 1 µm. Stalky aggregates replace them with sizes of approximately 50 - 100 nm, which form clusters and partially cover the remains of the Gordaite crystals. The Zn:O ratio of 1:1 confirms the formation of ZnO.

After 6 h aging, the Gordaite crystals have been almost entirely replaced by the rod-like ZnO. Correspondingly, the EDX analysis shows an increase in the amount of Zn in the precipitate and a decrease of Na, S, and Cl. After 6 h, only Zn and O were detected by EDX with a ratio of Zn:O of approximately 1:1. Figure 5.24c shows larger, rod-shaped ZnO crystals with a size of about 500 nm that are surrounded by agglomerates of smaller ZnO crystals with a size of few nm and irregular shape. Occasionally, still tiny, round-shaped Gordaite crystals with sizes < 100 nm can be seen. As shown in Figure 5.24d, with aging the suspension for 24 hours, the size of the ZnO rods increases to

500 nm - 1 µm. Thus, the size distribution of ZnO is more homogeneous as no small ZnO crystals are present. However, there are also platy crystals with an irregular shape, which correspond to Gordaite.

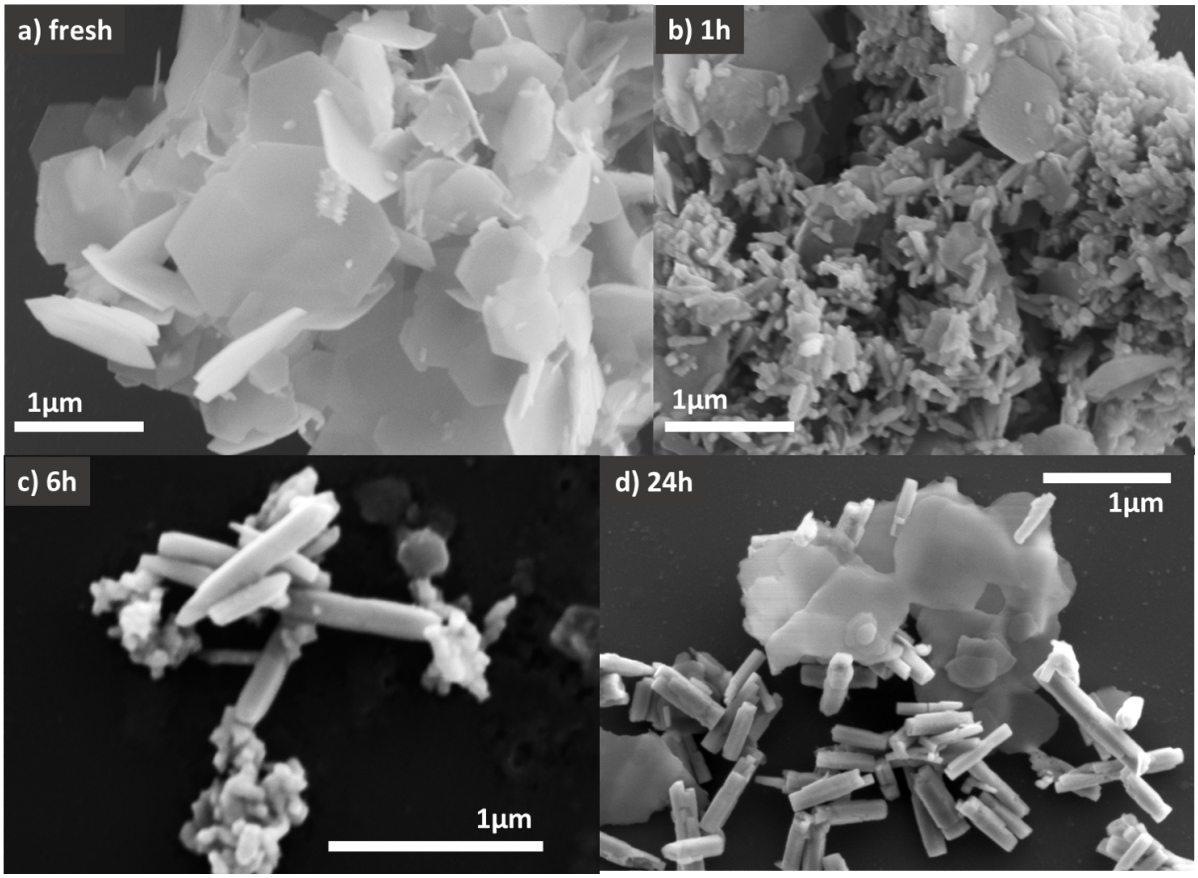

Figure 5.24: SEM images of the washed precipitates (a) fresh and after aging at 110 °C for (b) 1 h, (c) 2 h, (d) 6 h, and (e) after 24 h.

5.3.3.2. Dependence of aging temperature

Water purification

Table 5.13 shows the Zn-concentrations of Set 7 before the Gordaite precipitation and after the temperature-dependent aging of the precipitates for 24 h together with the calculated Zn-removal efficiencies. Gordaite was synthesized using medium A2 and 30 °C reaction temperature. After 24 hours of tempering, independent of the aging temperature, the Zn concentrations in all examined filtrates were > 150 mg/l. The lowest Zn concentrations of 154.7 mg/l are analyzed at 70 °C aging temperature. This corresponds to a Zn-removal efficiency of 94 %. Aging temperatures between 80 – 100 °C show even higher Zn concentrations, with the highest value of 257.7 mg/l at 100 °C. In comparison, at the aging temperature of 110 °C, the Zn-concentration is with 199.4 mg/l lower, although the initial concentration was higher.

Table 5.13: Zn-concentration in the filtrate and removal efficiencies of Zn in Set 7 at constant aging time of 24 hours in dependence of aging temperature.

Name	Zn initial [mg/l]	RSD [%]	Zn in filtrate [mg/l]	RSD [%]	Zn-removal efficiency [%]	RSD [%]
Zn_30 °C_A2_24_RT	n.d.	n.d.	n.d.	-	-	-
Zn_30 °C_A2_24_70 °C	2561.8	6.0	154.7	5.9	94.0	8.5
Zn_30 °C_A2_24_70 °C_stir	n.d.	n.d.	n.d.	-	-	-
Zn_30 °C_A2_24_80 °C	2144.4	1.7	224.8	2.3	89.5	2.9
Zn_30 °C_A2_24_90 °C	2144.4	1.7	234.3	2.2	89.1	2.8
Zn_30 °C_A2_24_100 °C	2144.4	1.7	257.7	1.9	88.0	2.5
Zn_30 °C_A2_24h_110 °C	2561.8	6.0	199.4	1.9	92.2	6.3

Mineralogical characterization of Set 7 phases

XRD results

Figure 5.25 shows the XRD pattern of the washed precipitates aged 24 h at temperatures between 70 °C and 110 °C. As a reference, one sample was aged for 24 h at room temperature (RT). Additionally, one suspension was stirred continuously during aging at 70 °C for 24 h (70 °C_stir).

Depending on the aging temperature, either Gordaite or Zincite is the main phase in the XRD pattern. At room temperature, Gordaite is the only phase detected. At 70 °C, Gordaite is still the main phase. In addition, a broad hill at approx. 8.5° 2θ matches the main reflex (001) of Namuwite. In the diffractogram, there are three peaks with low intensity at 31.57 °2θ, 34.37 °2θ and at 36.13 °2θ that match the main reflexes of ZnO. Stirring the suspension during aging at the same temperature causes a remarkable effect: In contrast to undisturbed aging, stirring causes the formation of ZnO, as can be seen in the example Zn_30 °C_A2_24_70 °C_stir in Figure 5.25. Apart from ZnO peaks, only a small peak at 6.84 °2θ was detected, which matches to the main reflex (001) of Gordaite. At 80 °C and above, ZnO is the main phase. In addition, the samples that were aged at 80 °C and 90 °C show peaks with a low intensity that match to Bechererite (COD 9001720) with main reflex (001) at 11.99 °2θ. In the sample aged at 110 °C, an additional reflex with low intensity at 6.84 °2θ indicates that Gordaite is still present.

In all diffractograms of Set 7 with ZnO as the main phase except for sample Zn_30 °C_A2_24_70 °C_stir that was stirred during aging, the (002) reflex of ZnO at 34.37° 2θ has higher relative intensity compared to the reference. In addition, the broadness of the ZnO reflexes increases with increasing aging temperature. Two peaks in the diffraction patterns of Set 7 could not be identified, one peak at 11.63° 2θ and one at 11.27° 2θ in sample Zn_A2_24h_80 °C and Zn_A2_24h_90 °C, respectively.

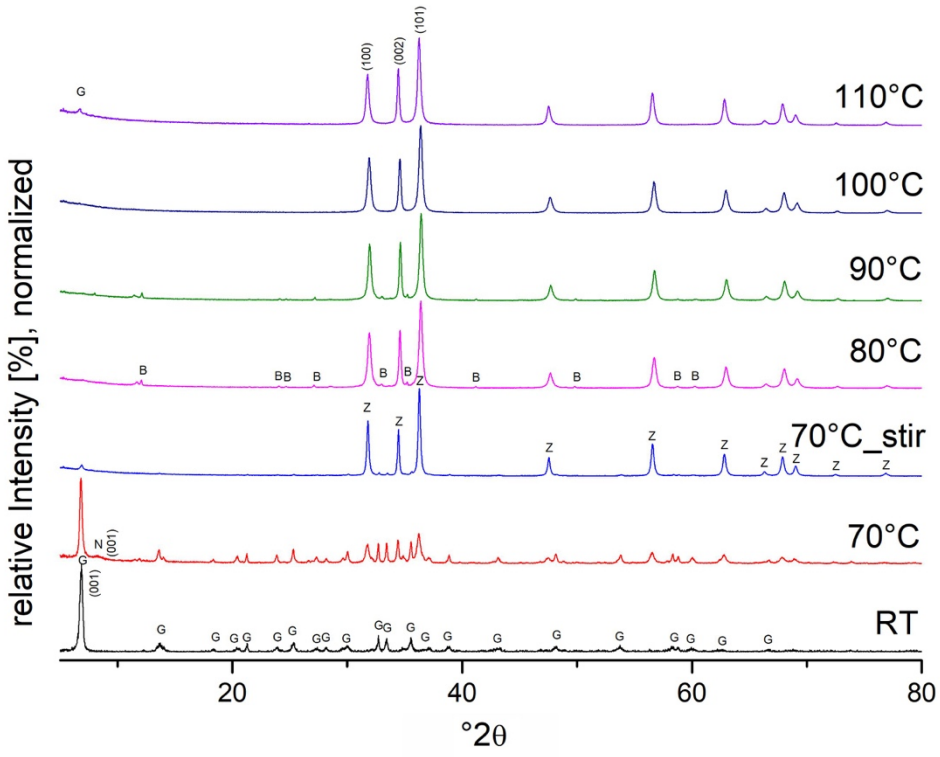

Figure 5.25: XRD pattern of the washed precipitates of Set 7 after 24h tempering as a function of the aging temperature. G = Gordaite, N = Namuwite, Z = Zincite, B = Bechererite.

FTIR spectroscopy

The phases determined by FTIR in the samples of Set 7 correspond to the results from XRD (see Figure 5.26). In all FTIR spectra are bands with low intensity in the range of 3500 cm^{-1} present, corresponding to the Gordaite O-H bands. After aging the suspension at room temperature, the band maxima can be assigned to Gordaite. At 70 °C aging temperature, there are additional bands of low intensity at positions that match Namuwite bands. The FTIR spectra of the precipitate that was stirred in suspension during aging at 70 °C is different. Stirring during aging at 70 °C leads to a different FTIR spectrum. It shows bands of high intensity at positions that match ZnO bands and only bands with low intensity matching Gordaite. In general, aging the saline suspension at temperatures ≥ 80 °C for 24 h leads to FTIR spectra with bands at positions assigned to Zincite. In addition, the samples that were aged at 80 °C and 90 °C show bands of low intensity at 1020 cm^{-1}, 1103 $cm^{-1,}$ and 1122 cm^{-1} that can be assigned to Bechererite (Chukanov 2014). At 841 cm^{-1} and 902 cm^{-1}, two bands observed in the sample Zn_30 °C_A2_24h_110 °C aged at 110 °C can be assigned to Gordaite.

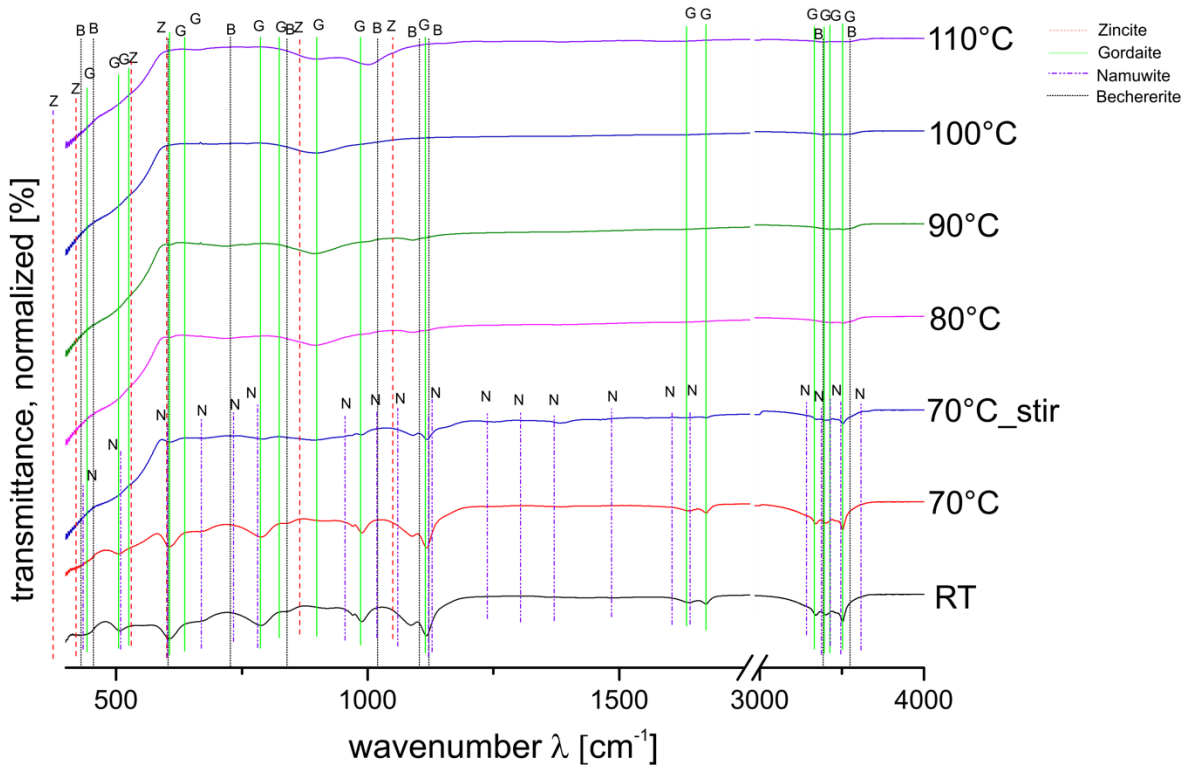

Figure 5.26: FTIR-spectra of the washed precipitates from Set 7 at a constant aging time (24 h) in dependence of aging temperature. G = Gordaite, N = Namuwite, Z = Zincite, B = Bechererite.

SEM

Figures 5.27a and b show SEM images of the precipitates aged for 24 h at 70 °C. Clusters of crystals with approximately 1-2 µm in size dominate. The crystals have a hexagonal shape with a smooth surface but partly only slightly rounded edges. EDX analysis proof that they are Gordaite. On the surface of the Gordaite crystals, single rod-shaped crystals of a few nm up to 200 nm in size occur, forming clusters in the range of approximately 1 µm. These clusters are typically observed on the surface of the Gordaite crystals, which are more rounded, as shown in the upper center of Figure 5.27a and the upper left corner of Figure 5.27b.

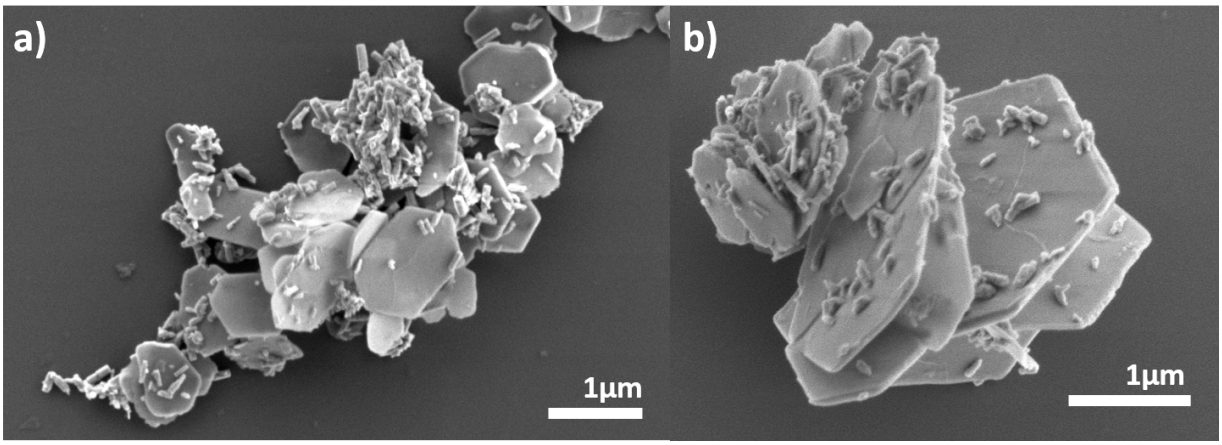

Figure 5.27: (a) and (b) SEM images of the washed precipitates after aging at 70 °C for 24h in a suspension.

5.3.4. Discussion

5.3.4.1. Effect of aging time for samples tempered at 110 °C

Gordaite was successfully synthesized according to the method described in chapter 5.2. The effect of aging time on the Zn concentration in the filtrate of the Set 6 experiments tempered at 110 °C shows Figure 5.28. The symbols in the figure represent the main phases in the fresh and aged precipitates. Due to matrix effects and related analytical reasons, the RSD is relatively high.

When Gordaite precipitates, the Zn-concentration drops from initially about 2000 mg/l to 20.5 mg/l in the fresh filtrate. Aging at 110 °C increases the Zn-concentration in the filtrate to over 150 mg/l. Already after 1 h aging, Zn-concentration rises by a factor of 8 to 158.7 mg/l. It increases slightly with aging time, resulting in the highest Zn-concentrations of 199.4 mg/l after 24 h aging at 110 °C. Correspondingly, the calculated removal efficiencies of the aged precipitates for Zn decrease with aging time from 99.2 % (fresh) over 93.6 % (2 h) to 92.2 % (24 h), with one exception. Considering the absolute concentration, the 1 h aged sample Zn_30 °C_A2_1h_110 °C fits into the observed trend, that the Zn-concentration in the filtrate increases with increasing aging time. The lower removal efficiency of the sample compared to the others is caused by the lower initial Zn-concentration with 2144.4 mg/l (± 1,7 %) in comparison to that of the other samples (2561.8 mg/l ± 6 %).

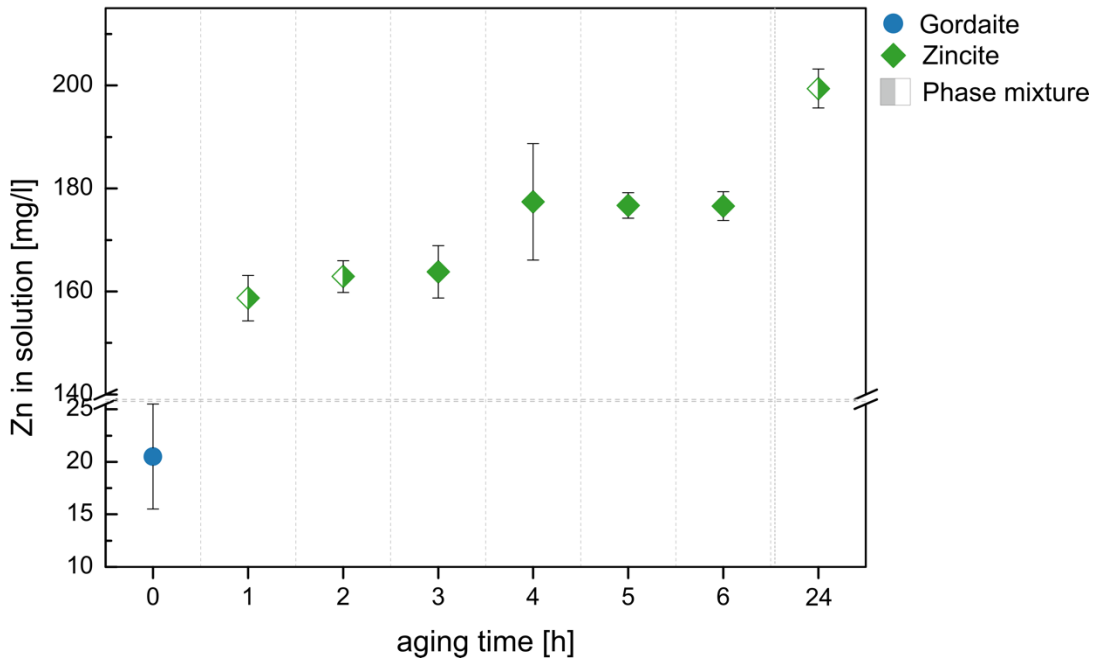

Figure 5.28: Zn-concentration in mg/l in dependence of aging time for Set 6 experiments, tempered at 110 °C. The color of the symbols indicates the main phases in the fresh and aged precipitates: blue for Gordaite, green for Zincite. Half-filled symbols point to phase mixtures with the color of the main phase.

Figure 5.29 shows a summary of the phases formed as a function of aging time at 110 °C. Aging Gordaite successfully synthesized ZnO in the saline AQ at 110 °C. The XRD patterns show that aging of only one hour is sufficient to replace Gordaite with ZnO as the main phase in the saline suspension. A clear systematic trend can be observed: with increasing aging time, the Gordaite content in the aged precipitate decreases, and the Zincite content increases. After 3 h aging, the analysis of the FTIR spectra still shows traces of Gordaite present in the precipitate, although ZnO is the only phase detected by XRD. After 4 h aging, ZnO is the only phase detected. The high amount of ZnO already observed within less than one hour indicates a high reaction rate. The accompanying significant increase in Zn concentration in the filtrate suggests a dissolution-precipitation reaction. The presence of traces of Gordaite in sample Zn_30 °C_A2_24h_110 °C point to incomplete dissolution of Gordaite in this sample, which is also indicated by the remains of strongly dissolved Gordaite crystals that are present in the SEM image of the sample.

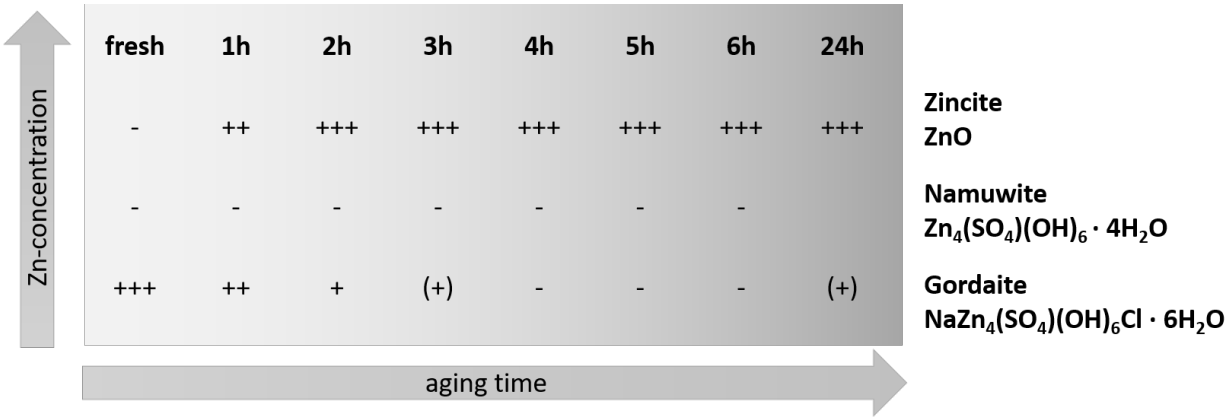

Figure 5.29: Overview of the phases formed as a function of ageing time at 110 °C (Set 6).
+++ = high relative proportion, (+) = traces of the phase, - = not detected.

John et al. (2016d) as well as Tandon et al. (2018) and Tandon and Heuss-Aßbichler (2021b) showed that ZnO can be directly synthesized from SO_4-rich solutions and Cl-rich solutions, respectively, without aging. In both cases, Zn-removal efficiencies of 99.9 % were achieved. In comparison, the synthesis results after aging Gordaite leads to lower removal efficiencies being between 92.2 and 93.6 %. This means that in the model system, in terms of purification and reaction yield for Zn, the direct method is more effective.

Hagemann (2012) described in his work that ZnO directly forms in the system Zn-OH upon aging highly concentrated, caustic Zincate solution (> 8 mol/l OH) but did not provide any details about the exact concentration of Zn. The saline solution in our experiments was solely alkalized with 8M NaOH; the Zn-solution was not put into concentrated NaOH. Accordingly, the OH concentration in the aging solutions of our study is remarkably lower. Dietrich and Johnston (1927) synthesized $Zn(OH)_2$ and observed a temperature and time-dependent decomposition of the Zn-hydroxide to ZnO in H_2O.

At temperatures > 100 °C, the authors observed a decomposition of $Zn(OH)_2$ to ZnO within 1 h. Our study observed a similar time dependence at 110 °C in our considerably more complex system when aging Gordaite in saline solution instead of H_2O. This suggests that accessory elements like Na, K, Ca, Cl, and SO_4 do not inhibit the conversion of the Zn-Hydroxysulfate Gordaite to ZnO, although the Gordaite structure is considerably more complex than that of $Zn(OH)_2$. Our results show that the dissolution-precipitation reaction of Gordaite to ZnO is completed within 4 h in the saline System at 110 °C. The increased aging time of 4 h in our system compared to 1 h in the Zn-OH system of Dietrich and Johnston (1927) can have several reasons; either it is an effect of the remarkably higher ionic strength in the saline solution compared to H_2O, or it may be an effect of the more complex structure of Gordaite. $Zn(OH)_2$ and ZnO have a similar structure, built of Zn-tetrahedra that are corner linked, and instead of O in ZnO in the Zn-hydroxide, the OH ions are located at the corners. Although the authors did not give any information about the transformation process, it is likely that the conversion of $Zn(OH)_2$ to ZnO is based on temperature-induced dehydroxylation (> 100 °C) of the structure since the main building unit of ZnO, the Zn-tetrahedra, are already present. This is very different in our system, where Gordaite dissolves and ZnO precipitates. In addition, this process takes more time. It is also possible that the increased aging time of Gordaite to Zincite may be a combination of both effects.

As a fresh precipitate, Gordaite crystals show idiomorphic shape. The time-dependent aging experiments at 110 °C show that the Gordaite crystals continuously dissolve, starting at the edges, and ZnO nanorods form instead. The ZnO nanorods that precipitate from the solution are nanocrystalline and form preferentially on the surfaces of the Gordaite crystals, which show dissolution signs. All experiments of Set 6 were aged without stirring. The only convection that leads to homogenization of the solution is concentration-driven because the aging vessel is put into an oven for constant aging temperature. So thermal convection in the suspension can be excluded. The preferential crystallization of ZnO on the surfaces of the Gordaite crystals, which show clear dissolution signs, can be explained by a local increase of Zn concentration in the saline suspension. The local concentration gradient between the Gordaite crystal edge and the ZnO nuclei on the surface can be the driving force for the dissolution precipitation process and thus favor the reaction conversion. In addition, the precipitation of ZnO on the surface of the Gordaite crystals points to heterogeneous nucleation. Heterogeneous nucleation drastically reduces the free energy that is needed for nucleation because a stable surface is already present, where nuclei can form (Thanh et al. 2014).

As shown in chapter 3.3 (relevant Zn-phases in Cl-rich solutions), the Gordaite structure contains Zn-tetrahedra on top and bottom of the vacancies of the octahedral layer. These Zn-tetrahedra are very similar to the building unit of ZnO. In ZnO, the tetrahedra are corner linked via O atoms. In contrast, in Gordaite, the tetrahedra are connected to the octahedral layers via 3 OH^- atoms, while

Cl^- is bonded to the 4th corner on the apex. From this point of view, the Zn tetrahedra on the surface of the Gordaite crystals can promote the formation of ZnO crystals via a topotactic reaction. This hypothesis would also explain the presence of small, stalky aggregates that were already observed on fresh Gordaite. Due to their small size in the range of some nm, these crystals could not be analyzed further by EDX. The amount of these nanoparticles in the fresh precipitate is too small to be detected by XRD and FTIR. FTIR spectra are based on the detection of molecular vibrations. This means that in the FTIR spectrum of Gordaite, there are also bands at the same or similar wavenumbers that match Zn-O vibrations, e.g., at 442 cm^{-1} for both minerals or 530 cm^{-1} and 525 cm^{-1} for Zincite or Gordaite, respectively. Therefore, FTIR spectra cannot be used in this case to identify the presence of trace amounts of ZnO, as the ZnO tetrahedra of Gordaite may contribute to the bands. Although these isolated nanocrystals on the surface of the Gordaite crystals in the fresh sample could not be identified with certainty, the SEM images and the reaction mechanism point to the presence of the first ZnO nanoparticles that have grown occasionally on the Zn tetrahedra in the Gordaite.

The SEM images also show that with increasing aging time, some ZnO nuclei grow at the expense of smaller ZnO nanoparticles, indicated by agglomerates of smaller ZnO particles with irregular shape next to the single lager ZnO crystals. After 24 h aging at 110 °C, they have sizes of 500 nm – 1 µm. In their review about the “Mechanisms of Nucleation and Growth of Nanoparticles in Solution”, Thanh et al. (2014) summarized the basic principles of how nanoparticles can form in solutions. These are via the LaMer mechanism, Ostwald ripening, digestive ripening, and Finke-Watzky two-step mechanism, coalescence, and oriented attachment or by intraparticle growth. Ostwald ripening is the only growth mechanism they described that explains the growth of larger nanoparticles at the expense of smaller ones. This suggests that the enlargement of the ZnO crystals upon aging is due to Ostwald ripening. In all XRD patterns of Set 6 with ZnO as the main phase, the (002) reflexes of ZnO were compared to the reference lower, indicating a preferred orientation of the nanoparticles (Holder and Schaak 2019). As the preferred orientation is identical in all diffractograms with increasing aging time, this indicates no change in morphology, which is another indication for growth of the ZnO-nanoparticles by Ostwald ripening. The broad shape of the ZnO peaks in XRD suggests that the synthesized ZnO is nanocrystalline (Holder and Schaak 2019), which matches with the observations of SEM.

5.3.4.2. Effect of aging temperature

Figure 5.30 shows the effect of varying aging temperature at a constant aging time of 24 h on the Zn-concentrations in the filtrates from Set 7 combined with the phases. In Set 7, after aging Gordaite in saline AQ for 24 h at temperatures between 70 – 110 °C, the Zn concentrations in the filtrates

increase from initially 20.5 mg/l to > 150 mg/l. The high RSD of the measurements is due to analytical reasons and was already observed in Set 6.

As in Set 6, the calculated removal efficiencies of the filtrates with aging temperatures 70 °C, 80 °C, and 90 °C have lower initial Zn-concentration. Accordingly, the removal efficiencies are lower compared to the experiments that were performed with higher initial concentrations. The Zn concentrations are elevated in these filtrates compared to the other experiments in this set with higher initial concentrations. The results indicate that these elevated concentrations are not only an effect of the different initial concentrations. When tempering the saline suspension for 24 h at 70 °C, Gordaite remains the main phase. At 70 °C and 80 °C aging temperature, when the main phase in the aged precipitate changes from Gordaite to Zincite, there is a clear jump in Zn-concentration, from 154.7 to 224.8 mg/l. Although the water analysis from this set cannot be compared directly, these two experiments were from the same batch and had the same initial concentrations. This increase in Zn-concentration is therefore reliable and must be due to the dissolution of Gordaite in the aged precipitate and may not be an effect of the experimental setting.

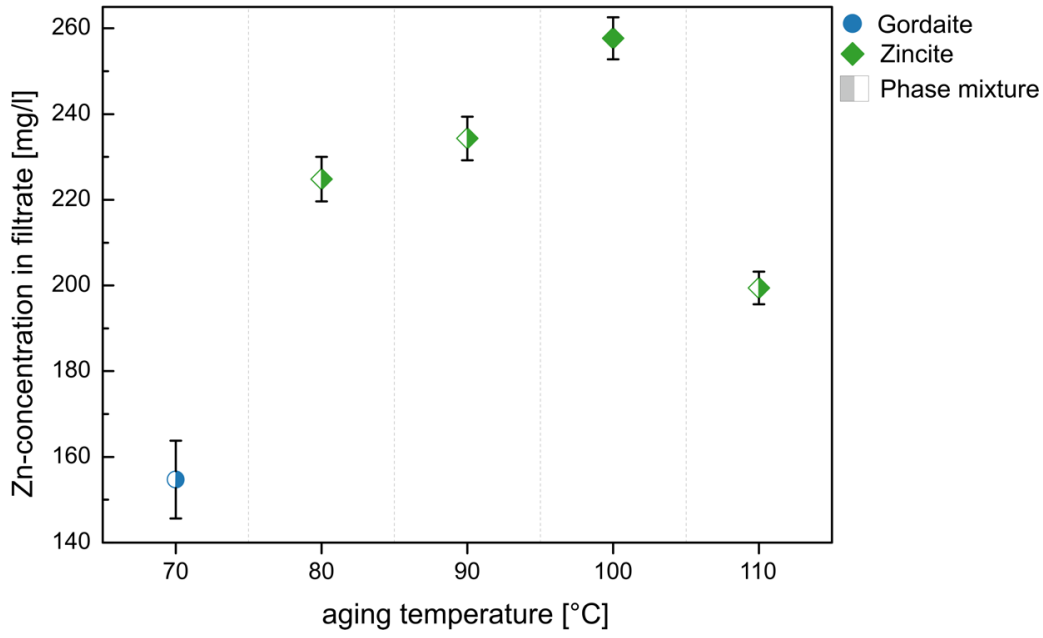

Figure 5.30: Zn-concentration in the filtrates including RSD in mg/l after 24 tempering with increasing aging temperature. The color of the symbols indicates the main phases in the aged precipitates, blue for Gordaite, green for Zincite. Half-filled symbols point to phase mixtures with the color of the main phase.

The phases developed after 24 h tempering as a function of aging temperature (Set 7) and identified by mineralogical characterization are summarized in Figure 5.31. Comparing the phases, a clear trend can be observed. Gordaite is still the main phase after tempering at 70 °C without stirring the solution. SEM pictures show no idiomorphic shape of Gordaite and first dissolution signs at 70 °C. In addition, stalky aggregates of nanocrystalline ZnO-rods are present.

The observations in Set 7 match with that of Set 6. Accordingly, the results support the reaction mechanism of how ZnO forms described in Set 6: a dissolution-precipitation reaction with a beginning dissolution of Gordaite at the edges of the crystals and heterogeneous, topotactic ZnO nucleation. When the suspension is stirred during aging at 70 °C, ZnO is the main phase, and only traces of Gordaite are present in the precipitate. This suggests that stirring during aging accelerates the dissolution of Gordaite and homogenizes the solution. Accordingly, it accelerates the whole dissolution-precipitation reaction of Gordaite to Zincite. Without stirring, Gordaite dissolves slower. This means higher temperatures are necessary to dissolve Gordaite at the set aging time of 24 h. The mineralogical characterization of the aged precipitates after tempering at 80 °C shows in contrast to 70 °C no Gordaite and only Zincite as the main phase. Therefore, aging at 80 °C is sufficient to dissolve Gordaite and precipitate Zincite within 24 h without stirring.

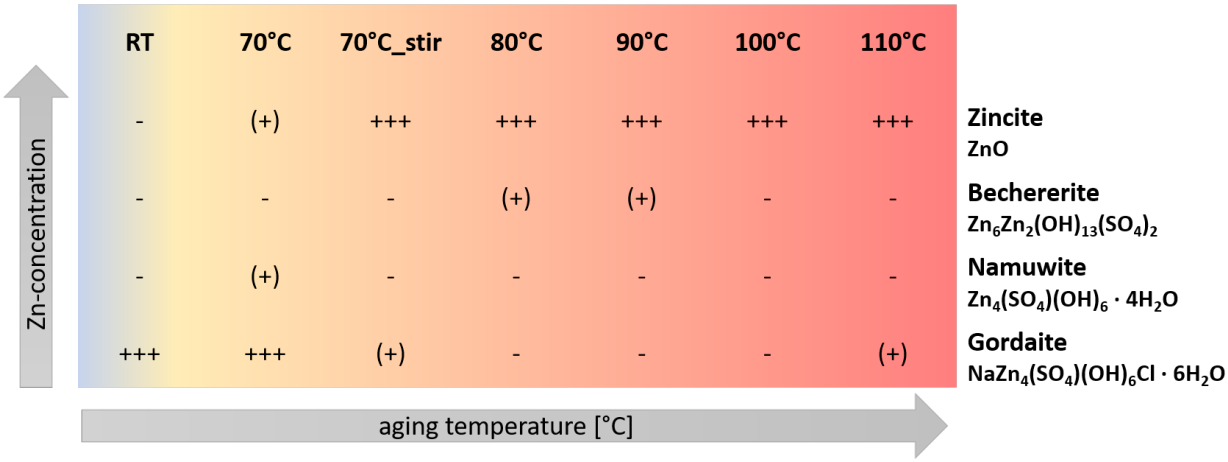

Figure 5.31: Overview of the phases formed after 24 h tempering time as a function of aging temperature, after washing the precipitates from Set 7. +++ = high relative proportion, (+) = traces of the phase, - = not detected.

Tandon and Heuss-Aßbichler (2021b) described high removal efficiencies after direct precipitation of ZnO from saline AQ. When Gordaite or phase mixtures were present in the precipitates, the authors obtained lower removal efficiencies. These results are contrary to that described here in dependence of the aging temperature after 24 h. The removal efficiencies are always higher when Gordaite precipitates, or phase mixtures are present in the precipitate. Accordingly, these deviating results must be due to the different synthesis methods for ZnO, the dissolution-precipitation reaction upon aging Gordaite instead of the direct precipitation of ZnO.

Dietrich and Johnston (1927) synthesized $Zn(OH)_2$ and observed that the decomposition of $Zn(OH)_2$ to ZnO in water is not only time but also temperature-dependent. After aging $Zn(OH)_2$ for 3 weeks at different temperatures in water, they did not observe a remarkable decomposition to ZnO at 65 °C; increasing the temperature by 10 °C to 75 °C resulted in 10 % ZnO. Above this temperature, the authors

observed a rapid increase in the decomposition rate of the Zn-hydroxide to ZnO, and at temperatures > 100 °, the decomposition was completed within 1 h. Our study observed a similar time and temperature dependence in our considerably more complex system upon aging Gordaite in saline solution instead of water. The transformation reaction usually was completed within 24 h instead of 3 weeks, as in the study of Dietrich and Johnston (1927). Gordaite transforms to ZnO in the saline solution already after 24 h aging without stirring between 70 - 80 °C. Stirring increases the dissolution rate of Gordaite and ZnO precipitates already at 70 °C within 24 h. However, in both cases, a liquid phase is essential for the transformation to take place. The studies of Stanimirova et al. (2016) on the thermal decomposition of layered Zn-hydroxy sulfate minerals, including Gordaite, support this. In their work, the authors show the various stages of Gordaite decomposition and detected traces of ZnO for the first time at 200 °C. Delcheva et al. (2019) observed the same results for Br-Gordaite at temperatures between 185 – 230 °C. Both works studied the thermal decomposition of the mineral under vacuum or air. The authors did not age Gordaite hydrothermally in saline suspension as it was done in this study or H_2O, as Dietrich and Johnston (1927) did. Our results clearly show that a dissolution-precipitation reaction takes place when aging the Gordaite hydrothermally. Essential for this process to take place is a liquid phase, which was not the case during the studies of Stanimirova et al. (2016) and Delcheva et al. (2019). Thus, aging Gordaite in saline suspension transforms it to Zincite at temperatures of about 70 °C – 80 °C, instead its partial thermal decomposition to ZnO at temperatures of 185 °C – 230 °C without a liquid phase, as described by Stanimirova et al. (2016) and Delcheva et al. (2019).

Traces of Bechererite are detected in the aged precipitates with ZnO as the main phase tempered at 80 °C and 90 °C. However, Bechererite was not detected in sample Zn_30 °C_A2_24h70 °C_stir. Figure 5.32 compares the structures of Gordaite, Namuwite, and Bechererite. The minerals have closely related structures consisting of octahedral and tetrahedral sheets with Zn in the center, and every 7^{th} octahedron is vacant (Hawthorne and Sokolova 2002).

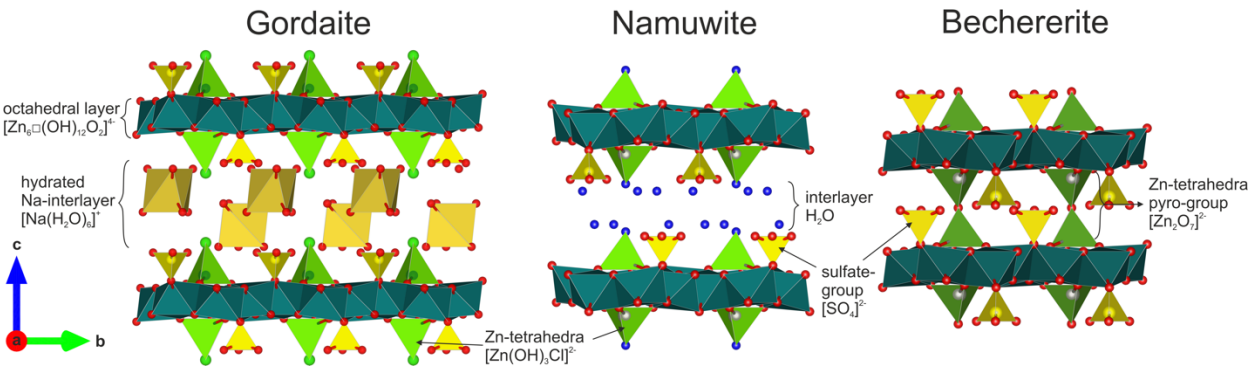

Figure 5.32: Crystal structure of Gordaite (left, after Adiwidjaja et al. (1997)), Namuwite (middle, after Groat (1996)) and Bechererite (right, after Giester and Rieck (1996)) in b-c projection. Crystal structures are created using the software VESTA 3 (Momma and Izumi 2011).

The essential difference between these minerals is the presence of different ions between the octahedral layers and how these layers are connected. Gordaite contains Cl-ions on the apex of the Zn-tetrahedra and hydrated Na-ions between the layers. Due to the incorporation of the ions, the distance between the octahedral layers is relatively large. The layers are solely connected via hydrogen bonds. In Namuwite, H_2O is on the apex of the Zn-tetrahedron, and H_2O is intercalated between the sheets. The octahedral sheets are still connected solely via hydrogen bonds. Bechererite is different. In Bechererite, the octahedral sheets are connected covalently by the Zn-tetrahedra on top and bottom of each octahedral layer, forming $[Zn_2O_7]^{6-}$ pyro-groups and making this structure ordered and more stable compared to Gordaite and Namuwite, where the sheets are connected via hydrogen bonds. Besides its occurrence as a secondary mineral in nature, there is no synthesis method for Bechererite in the laboratory found in the literature. Based on the available data, it cannot be said with certainty how exactly Bechererite forms. A possible hypothesis for the occurrence of Bechererite at 80 °C or 90 °C could be that stacking faults occur locally in Gordaite. This allows the octahedral Zn-layers to be partially bonded directly via the Zn-tetrahedra, forming the pyro-group that connects the octahedral layers in the Bechererite structure. In contrast to Gordaite, Bechererite is stable at higher temperatures due to the covalent bonding system. The temperature-related dehydration upon aging of Gordaite likely causes the stacking faults that lead to Bechererite formation since Bechererite only occurs when the solution has not been stirred during aging. If these stacking faults were already formed during the synthesis of Gordaite, they should be found in the sample with Gordaite as the main phase at 70 °C, too. Temperatures of 100 °C and higher seem to be too high for this phenomenon to occur. The presence of traces of Namuwite observed next to Gordaite as the main phase in XRD and FTIR after tempering at 70 °C for 24 h may be an effect of washing, as was already observed by Tandon et al. (2018) and Tandon and Heuss-Aßbichler (2021b).

Another explanation for the presence of Namuwite after aging for 24 h could be that the mineral is likely to form at 70 °C according to the same mechanism as Bechererite between 80 °C and 90 °C. Above 70 °C, Namuwite is, like Gordaite, not stable because the octahedral sheets are connected via hydrogen bonds.

5.4. MSWI fly ash as a source of Zn as secondary raw material: Application example for Zn recovery using SPOP from the eluates of MSWI fly ash

5.4.1. Purpose, scope, and nomenclature

The transfer of laboratory results to real conditions is a challenge. This final section aims to show that the SPOP process developed in a model system to recover Zn from real wastewater, fly ash eluates from MSWI, also works in practice. Both treatment concepts were developed on a laboratory scale. The direct precipitation of ZnO (Concept C1, based on chapter 5.2) and the recovery of ZnO by aging (Concept C2, based on chapter 5.3), were tested using wastewater from MSWI-plant Ingolstadt after the application of FLUWA.

Nomenclature: The first part of the nomenclature stands for the real wastewater (WW). The second part stands for the applied concept for ZnO synthesis, C1 for the direct precipitation method, and C2 for the aging method. The third suffix indicates the aging conditions of the suspension, f for the fresh precipitate taken immediately after the experiment, or the aging time in hours and aging temperature in °C. For example, WW-G1_C1_f refers to the fresh, washed residue precipitated from WW-G1 using the direct precipitation method. Medium alkalization rate A2 was used for all experiments. All precipitates were washed three times with deionized water (< 2µS/cm) immediately after the filtration.

5.4.2. Experimental series

Two different real wastewaters were used for the experiments. Their composition is shown in Table 5.14. The main matrix components are Na and Cl. The content of K, Ca, and SO_4 are < 10000 mg/l, and Mg is < 1000 mg/l. The concentrations of B and Si in the wastewater are between 25 and 180 mg/l. The dominant heavy metal in both samples is Zn, with 2395.5 mg/l (WW-G1) and 1587.9 mg/l (WW-G2). In both wastewaters, the concentration of the heavy metals Pb, Cu, Cd, and Mn, is < 215 mg/l. In addition, WW-G1 contains Fe and Al, which are not present in WW-G2.

Table 5.14: Composition of real wastewater from MSWI plant in Ingolstadt after application of FLUWA used for the precipitation experiments.

Element (mg/l)	WW-G1	RSD (%)	WW-G2	RSD (%)
Na	20609.6	0.9	22354.6	1.0
K	7181.5	1.1	8189.4	1.5
Ca	6534.1	2.8	3130.3	2.0
Mg	821.5	1.9	613.7	2.5
Cl	55000	< 1	52000	< 1
SO_4	1550	< 1	3000	< 1
Zn	2395.5	0.2	1587.9	1.4
Pb	112.8	1.7	198.7	9.8
Cu	54.6	5.6	10.7	1.2
Cd	37.9	2	214.0	9.0
Mn	40.7	4.2	82.1	1.3
Ni	-	-	1.0	3.1
Fe	187.7	0.5	0.0	-
B	179.5	4.5	32.5	15.8
Al	90.4	7.2	-	-
Si	27.9	0.1	77.8	8.9
Sb	-	-	1.3	7.3

Concept C1: the direct precipitation method

Concept C1, the direct precipitation method, is based on the method described in chapter 5.2 of this thesis. The optimal conditions in the model system for the recovery of ZnO without hydroxides was at 60 °C and using alkalization rate A2. For the experiments with real wastewater, the reaction temperature was increased by 10 °C to 70 °C. Figure 5.33 shows the principle of Concept C1. First, the wastewater was heated up to 70 °C reaction temperature. Then, the solution was alkalized to pH > 9 using alkalization rate A2 to precipitate ZnO. When the pH was reached, it is kept ≥ 9 for at least 5 minutes, and then the suspension was filtered. Wastewater WW-G1 was used to test Concept C1.

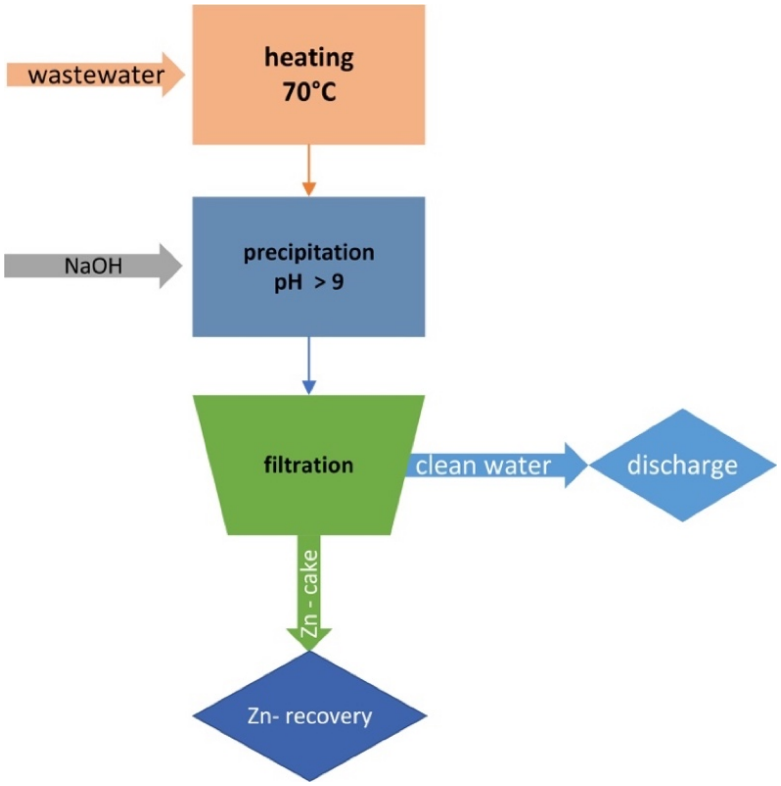

Figure 5.33: Concept C1 for the direct precipitation of ZnO from Cl-rich wastewater from MSWI fly ash eluates.

Concept C2: the aging method

Concept C2 is described in chapter 5.3 of this thesis. As shown in Figure 5.34, it consists of two steps, (i) precipitation of Gordaite and (ii) aging Gordaite in a suspension to form ZnO. First, the wastewater was alkalized to pH > 9 at 30 °C to precipitate Gordaite. After Gordaite precipitation, the main part of the liquid was removed immediately after precipitation. This is based on the experience in the model system that the Zn concentrations in the filtrates are lowest directly after Gordaite precipitation and increase within 1 h after aging. The cleaned water was tested to determine if the requirements for discharge are met. The suspension with Gordaite was aged at 110 °C for 24 hours. Afterward, the suspension was filtered. The Zn-rich filtrate after aging can be re-circulated and treated together with the wastewater after FLUWA. Wastewater WW-G2 was used to test Concept C2.

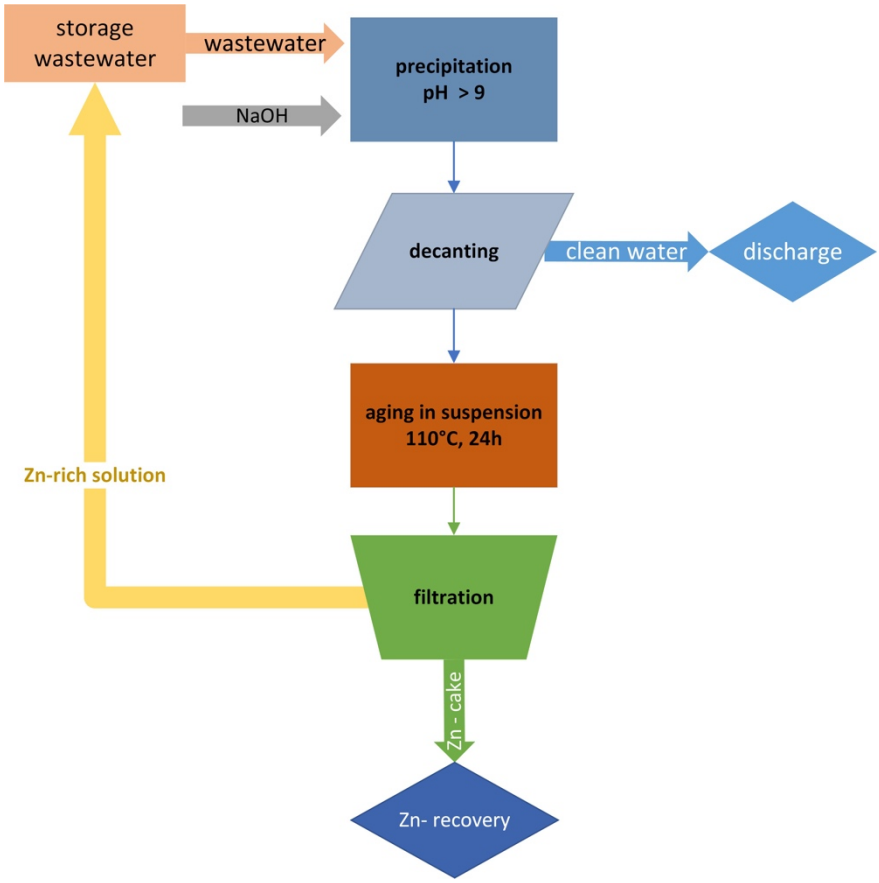

Figure 5.34: Concept C2, the aging method, to recover Zn as ZnO by precipitation and aging Gordaite in wastewater from MSWI fly ash eluates.

5.4.3. Results

5.4.3.1. Concept C1: the direct precipitation method

Water analysis

Table 5.15 presents the initial concentrations of WW-G1, the concentrations in the filtrates after the precipitation according to Concept C1, the calculated removal efficiencies of the matrix elements and the heavy metals, including the RSD. A high removal efficiency means that the target element is enriched in the precipitate.

Concept C1 does not affect the concentration of the matrix components. Compared to the initial solution, the concentrations of K and Ca remained unchanged, while the Na-concentration even increased. Mg is the only matrix component, where the concentration decreased by 97.8 %.

After the direct precipitation, the concentration of all heavy metals drops remarkably. Except for Zn, all concentrations are < 9 mg/l in the filtrate, which means a removal efficiency of the heavy metals > 90 %. The only exception is Cu with 85.2 % (8.1 mg/l Cu). Zn-concentration drops from 2395.5 mg/l to 19.2 mg/l. This corresponds to a removal efficiency of 99.2 %.

The concentration of other elements decreases, too: after precipitation, the B- concentration in the filtrate was 37.1 mg/l, which equals a removal efficiency of 79.3 % and Si-concentration drops from 27.9 mg/l to 2.6 mg/l (90 %).

Table 5.15: Initial concentration, concentration in the filtrate, and removal efficiencies of the matrix components and the heavy metals after applying Concept C-1, the direct precipitation method, to WW-G1.

Element	Initial concentration WW-G1 [mg/l]	RSD [%]	In filtrate [mg/l]	RSD [%]	Removal efficiency [%]	RSD [%]
Na	20609.6	0.9	23638.0	1.9	-14.7	2.1
K	7181.5	1.1	6366.6	2.1	11.3	2.4
Ca	6534.1	2.8	6061.9	0.7	7.2	2.9
Mg	821.5	1.9	17.7	11.9	97.8	12.0
Zn	2395.5	0.2	19.2	5.8	99.2	5.8
Pb	112.8	1.7	< 2	2.2	99.3	2.8
Cu	54.6	5.6	8.1	1.5	85.2	5.8
Cd	37.9	2	2.5	3.2	93.4	3.8
Mn	40.7	4.2	< 2	-	99.9	-
Fe	187.7	0.5	8.6	9.0	95.4	9.0
B	179.5	4.5	37.1	1.1	79.3	4.6
Al	90.4	7.2	4.5	8.1	95.0	10.8
Si	27.9	0.1	2.6	1.2	90.7	1.2

Mineralogical characterization of Concept C1 residues

Figure 5.35 shows the XRD pattern of the washed precipitate after the application of Concept C1 to WW-G1. In general, the relative intensity of the reflexes in the diffraction pattern is low, and the peaks are broad. In the initial range between 5 - 15 °2θ, the intensities are high and show a steep curve. The main phases observed in the XRD pattern of the sample are Simonkolleite, Zn(OH)Cl (COD ID 9004684), and Zincite (COD-ID 9011662). In addition, peaks of low-intensity match Halite (COD-ID 9008678).

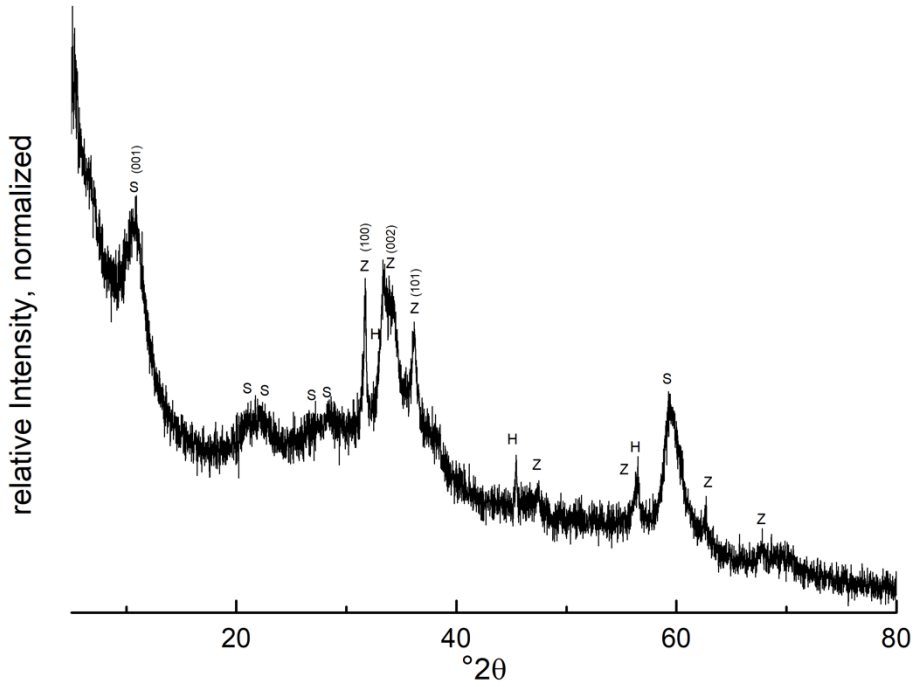

Figure 5.35: XRD pattern of the washed precipitate after treatment of wastewater WW-G1 using Concept C1 (direct precipitation method).

The FTIR spectrum of sample WW-G1_C1_f is shown in Figure 5.36. The spectrum shows band positions that can be assigned to Zincite and Simonkolleite (Chukanov 2014). In addition, bands with low intensity can be observed that match Namuwite (Stanimirova et al. 2018) and Goethite (FeO(OH)) (Chukanov 2014). In comparison, the relative intensities of the bands in the range of 3000 - 4000 cm^{-1} are lower than in the range of 400 - 750 cm^{-1}. In addition, bands are present in the spectrum at 1384 cm^{-1} and 1550 cm^{-1} that match the positions of surface adsorbed carbonate, as observed, for example on ferrihydrite by Hausner et al. (2009).

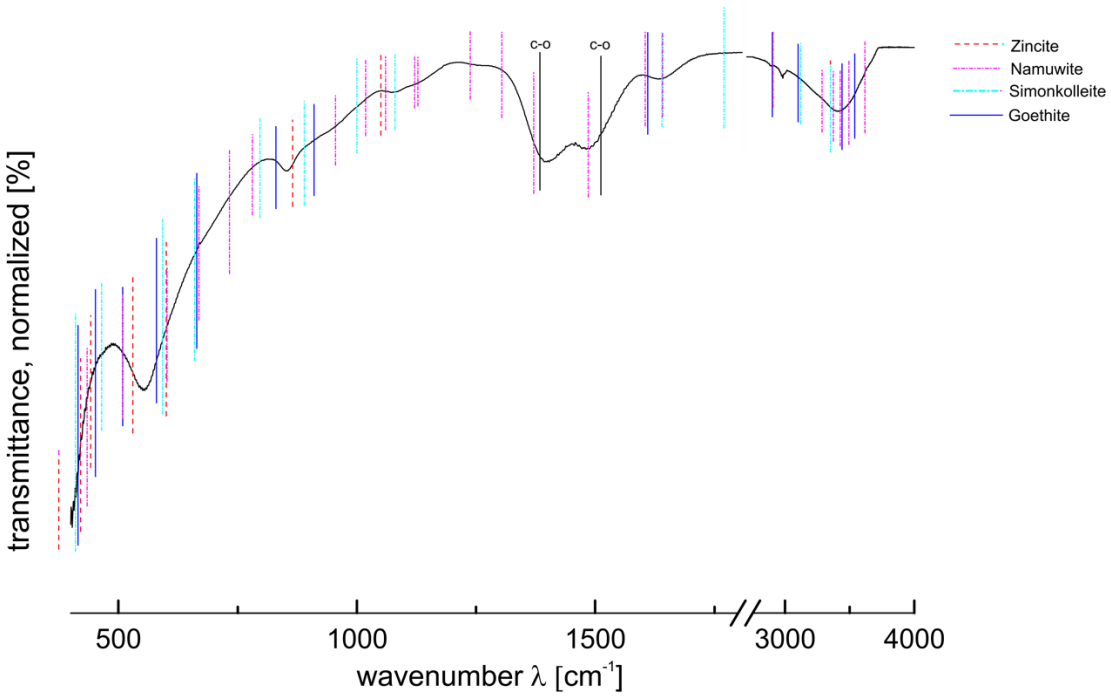

Figure 5.36: FTIR-spectrum of the washed precipitate after treatment of wastewater WW-G1 by Concept C1 (direct precipitation method).

5.4.3.2. Concept C2: the aging method

Water analysis

Table 5.16 shows the concentrations of the matrix elements and the heavy metals of wastewater WW-G2 before and in the fresh filtrate after the precipitation (step 1) using Concept C2, the aging method, as well as the calculated removal efficiencies. After precipitation, the concentration of the matrix components in the filtrate is still high, as indicated by the very low removal efficiencies < 1 %. K concentration is almost the same before and after the precipitation, while the Na-concentration increases. The concentration of Mg and B decreased by approx. 20 %. After precipitation, the Si-concentration in the fresh filtrate is below 2 mg/l, which is the detection limit for analytical reasons.

In WW-G2, after precipitation, the concentration of almost all heavy metals was below the detection limit of 2 mg/l. This corresponds to a removal efficiency of 99.9 % for Zn, Pb, Cu, and Mn. The only exception is Cd with 107.1 mg/l in the filtrate, which corresponds to a removal efficiency of 50 %.

Table 5.16: Initial concentration, concentration in the filtrate, and removal efficiencies of the matrix components and the heavy metals after applying Concept C2, the aging method, to WW-G2.

Element	Initial concentration WW-G2 [mg/l]	RSD [%]	In filtrate [mg/l]	RSD [%]	Removal efficiency [%]	RSD [%]
Na	22354.6	1.0	23992.8	0.8	-7.3	1.3
K	8189.4	1.5	8301.2	0.8	-1.4	1.7
Ca	3130.3	2.0	3097.8	1.9	1.0	2.8
Mg	613.7	2.5	488.4	1.4	20.4	2.9
Zn	1587.9	1.4	< 2	10.4	99.9	10.5
Pb	198.7	9.8	< 2	-	99.9	-
Cu	10.7	1.2	< 2	-	99.9	-
Cd	214.0	9.0	107.1	2.5	50.0	9.3
Mn	82.1	1.3	< 2	8.7	99.9	8.8
B	32.5	15.8	26.3	1.3	19.1	15.9
Si	77.8	8.9	< 2	-	99.9	-

Mineralogical characterization of Concept C2 precipitates

Figure 5.37 shows the XRD pattern of the fresh and aged precipitate after processing WW-G2 by Concept C2, the aging method. Gordaite is the only phase present in the diffractogram of the fresh precipitate. After aging the Gordaite in the suspension at 110 °C for 24 h, the diffraction pattern of sample WW-G2_C2_24h_110 °C differs completely. The three main reflexes with the highest intensity at 31.57 °2θ, 34.47 °2θ and 36.13 °2θ correspond to the ZnO main peaks. In general, the reflexes are broadened, with the (100) reflex at 31.57 °2θ being higher compared to the reference. In addition, two further phases with low relative intensities can be identified in the diffraction pattern. Willemite (COD ID 9014832) with the main reflex at 33.93 °2θ and Simonkolleite with the main reflex at 11.22 °2θ.

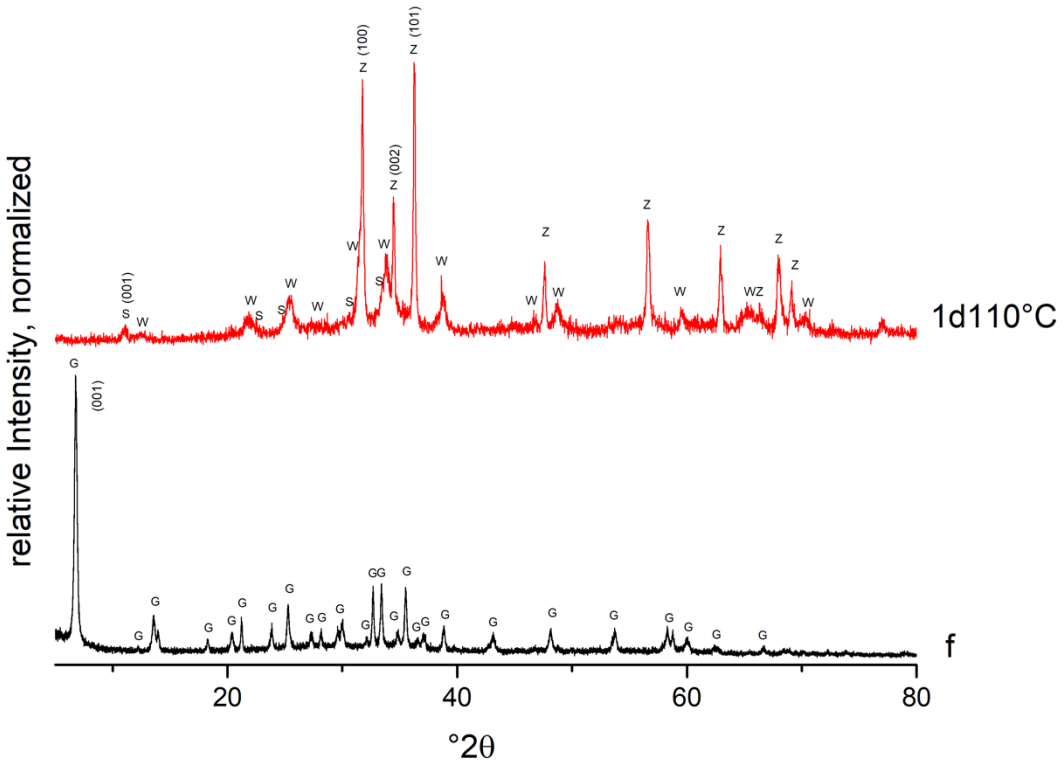

Figure 5.37: XRD pattern of the washed fresh and at 110 °C for 24 h aged precipitates after treatment of wastewater WW-G2 by Concept C2, the aging method.

The phases determined by FTIR (Figure 5.38) in the fresh sample after the aging method show, in general, the same phases as observed by XRD. The fresh precipitate shows band positions that match Gordaite bands. In addition, the sample shows bands of low intensity that can be assigned to Namuwite (Stanimirova et al. 2018), which can be identified by the band positions at 669 cm^{-1}, 783 cm^{-1}, 955 cm^{-1}, and 1080 cm^{-1} because Gordaite bands do not superimpose these bands.

The FTIR spectrum of sample WW-G2_C2_24h_110 °C shows bands of high intensity at 868 cm^{-1}, 901 cm^{-1}, 932 cm^{-1}, 945 cm^{-1}, and 977 cm^{-1} that can be assigned to Willemite. ZnO can also be identified by the characteristic bands at the beginning of the IR spectrum at 375 cm^{-1}, 420 cm^{-1}, 442 cm^{-1}, and 530 cm^{-1}. Bands of low intensity are observed that match Gordaite and Namuwite. Comparing the relative intensities within the FTIR spectra of sample WW-G2_C2_24h_110 °C, Willemite shows the highest relative intensities. Some band positions present in both FTIR spectra could not be assigned: at 1155cm^{-1} (shoulder), at 1412 cm^{-1}, at 1470 cm^{-1} (low relative intensity) and at 1577 cm^{-1}.

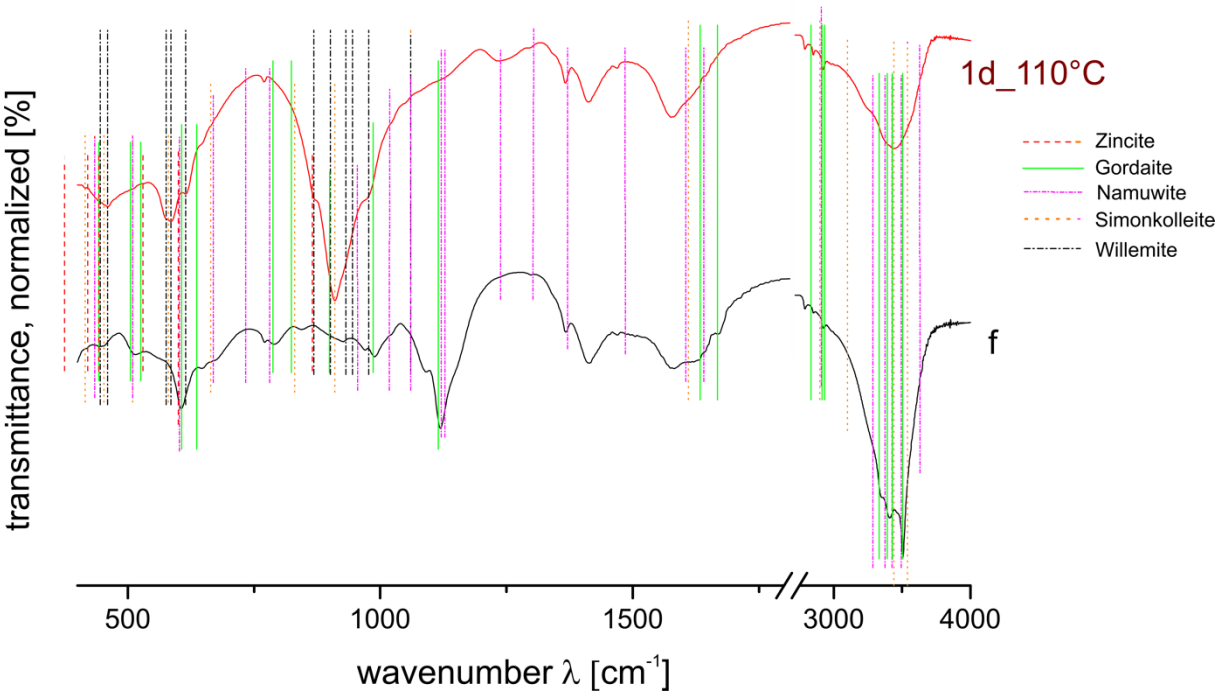

Figure 5.38: FTIR-spectra of the washed fresh and at 110 °C for 24h aged precipitates after treatment of wastewater WW-G2 by Concept C2, the aging method.

5.4.4. Discussion

5.4.4.1. Application of Concept C1, the direct precipitation method

The direct precipitation method C1 aims to precipitate ZnO directly from the wastewater. Figure 5.39 shows the composition of the matrix components and heavy metals before and after applying the direct method to wastewater WW-G1. The precipitation shows no effect on the composition of the matrix elements. The increase of Na in the filtrate after precipitation is due to the addition of Na as NaOH for alkalization. In contrast, the concentrations of the elements Pb and Mn decrease significantly, while the levels of Zn, Cu, Cd, Fe, B, Al, and Si remain slightly elevated. Especially the Zn-concentration with 19.2 mg/l is too high for discharge. In comparison, Zn concentrations below the detection limit (< 2 mg/l) were achieved in the model system with the direct method at 60 °C, corresponding to a removal efficiency of 99.9 %. This demonstrates the difference when treating real wastewater with various impurities and contaminations using Concept C1.

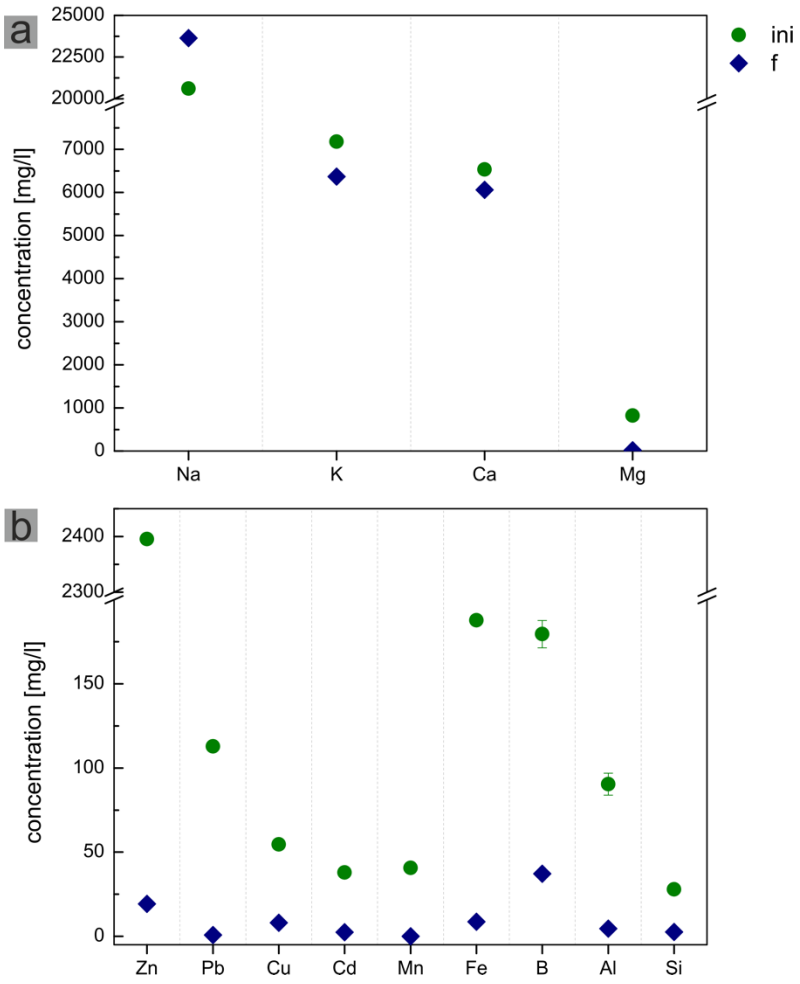

Figure 5.39: Water analysis of (a) the matrix compounds and (b) of the heavy metals including Si and B before and after applying Concept 1, the direct method, to wastewater WW-G1. If no error bars are displayed, the RSD is within the size of the symbol. ini stands for the untreated wastewater and f for the treated wastewater.

Both XRD and FTIR results show that it is possible to precipitate ZnO from real wastewater of MSWI fly ash eluates after FLUWA using the direct precipitation method. In the XRD pattern of sample WW-G1_C1_f, a steep curve at the beginning of the diffraction pattern can be observed. This effect is due to fluorescence radiation, caused by the interference of Fe in WW-G1 with the Cu_{ka1} radiation source. That Fe is present in the precipitate shows (i) the decrease in Fe- concentration in the filtrate after precipitation and (ii) the presence of traces of Goethite identified by FTIR. Because of the low relative intensity of the measurement, it was impossible to measure the sample with a threshold to filter out the Fe-fluorescence radiation, as this reduces the intensity of the whole sample even further. The low relative intensity points to a high amount of (X-ray) amorphous hydroxides (= low crystallinity) and/or nanocrystallinity. FTIR and XRD are complementary methods. If the proportion of hydroxides in the sample were high, the hydroxides' corresponding characteristic bands around 3000 – 4000 cm^{-1} would be present in the FTIR spectrum. Instead, the FTIR spectrum shows a high relative intensity of

ZnO bands and only low amounts of hydroxides. Comparing the FTIR results with the XRD pattern with the low relative intensity, the results point to nanocrystalline ZnO. When the crystallite size decreases to < 25 nm, the peak broadening increases significantly, and the peak intensity is low (Holder and Schaak 2019).

In sample WW-G1_C1_f, traces of Halite are present in the precipitate, and traces of Namuwite are present in the FTIR spectrum. Gordaite is not detected. Instead, the Zn-hydroxy chloride Simonkolleite is present in the precipitate, verified by XRD and FTIR. This phase was not observed in the model system. The relative intensities of Simonkolleite and Zincite in the XRD pattern are comparable, which would indicate a similar ratio of the phases in the precipitate. However, due to the small crystallite size of the ZnO nanoparticles, the proportion of ZnO must be higher. This is also confirmed by FTIR, where ZnO is the main phase. In the model system, only ZnO was observed (see chapter 5.2). The presence of additional phase(s) is obviously an effect of the real wastewater and the various accessory elements it contains. Another reason for the occurrence of Simonkolleite, the absence of Gordaite and only traces of Namuwite, may be the limited SO_4 availability. Simonkolleite is the thermodynamic stable phase in the system $ZnCl_2$-NaCl-H_2O at 25 °C (Hagemann 2012). In wastewater WW-G1, which was used to test the direct method, the SO_4 concentration is 1550 mg/l. In the experiments in the model system, where Gordaite precipitates, the SO_4 concentration were between 2500 – 5440 mg/l.

The water analysis show that most of the heavy metals are removed from the solution. Thus, they must be in the residue. The absence of other phases than Simonkolleite, Zincite, Goethite, and Namuwite point to (i) minerals that contain these elements and that are not detected or (ii) that these metals are incorporated into the present structures, e.g., into ZnO structure. Due to the low relative intensity of the reflexes in the XRD pattern, it is very probable that mineral phases are present that were not detected by XRD. Usually, the detection limit of XRD is approximately 3%. In this case, with real wastewater, fluorescence radiation, and the low intensity of the reflexes, this detection limit is certainly > 3%. This means other phases such as Laurionite (see chapter 5.1) might have precipitated below the detection limit, containing the remaining heavy metals that must be in the residue. John et al. (2016d) demonstrated that doped ZnO could precipitate from Cl-poor industrial wastewater, indicating that various elements can substitute Zn. This is most probably the case here, too. However, the results presented in this application example do not show to what extent Zn was substituted in ZnO. In general, the potential doping of ZnO could be determined by a shift of the ZnO reflexes in the XRD pattern. Due to the significant influence of the real wastewater on the measurements, this is impossible. Magnetic measurements could identify the very likely doping of ZnO.

5.4.4.2. Application of Concept C2, the aging method

Concept C2, the aging method, aims to gain ZnO by aging fresh precipitated Gordaite in saline suspension. Figure 5.40a shows the water analysis of the matrix compounds and Figure 5.40b of the heavy metals before and after applying Concept C2 to WW-G2. It shows that the concentration of the matrix compounds K, Ca, and Mg, as well as B, remains almost unchanged high in the filtrate, except Na. The increase of Na concentration after precipitation is due to adding NaOH for alkalization. In comparison, the heavy metals are effectively removed by Concept C2, except for Cd. After precipitation at 30 °C, the concentration of Zn, Pb, Cu, Mn, Ni, and Sb in the fresh filtrate was < 2 mg/l, which is the detection limit due to analytical reasons.

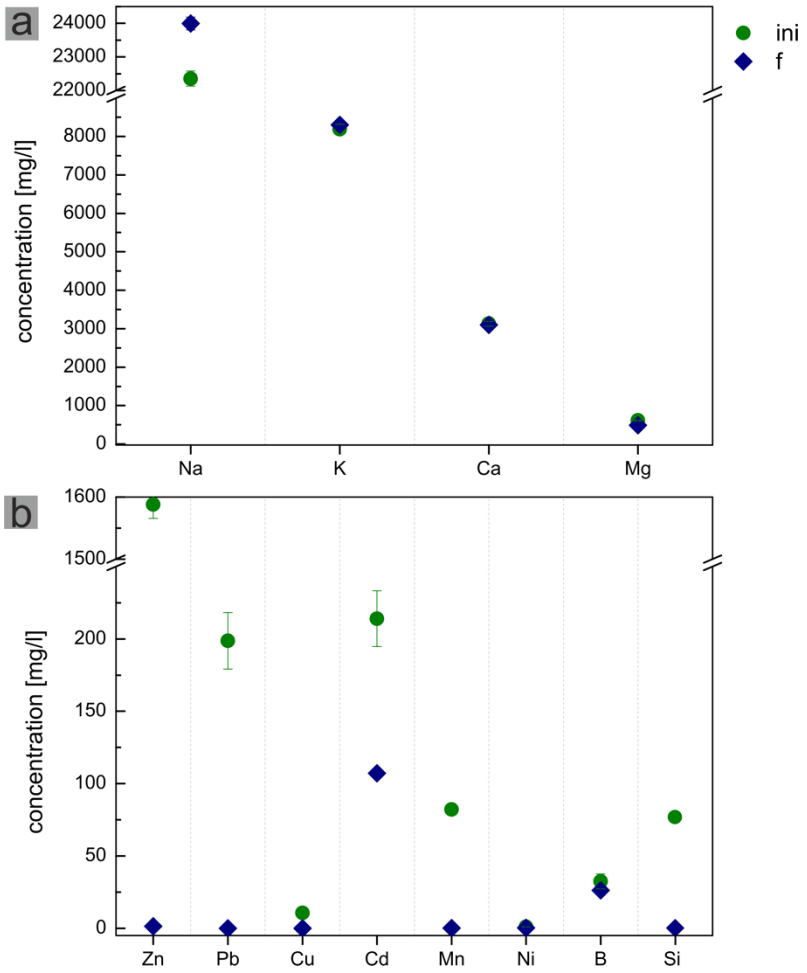

Fig 5.40: Composition of (a) matrix elements and (b) heavy metals in wastewater WW-G2 and fresh filtrate after application of Concept C2. If no error bars are displayed, the RSD is within the size of the symbol. ini stands for the untreated wastewater and f for the treated wastewater.

The mineralogical characterization shows that Gordaite is almost the only phase present immediately after precipitation at 30 °C. Traces of Namuwite, detected by FTIR, are presumably an effect of washing the fresh Gordaite, as was already observed in the model system (see chapters 5.1, 5.2, and 5.3).

The removal efficiency of the heavy metals in the filtrate after step I, the Gordaite precipitation, is high. This means that (i) minerals are present below the detection limit of XRD that contain these elements or (ii) that the heavy metals are incorporated into the Gordaite structure. Gordaite has a high anion and cation exchange capacity (see chapter 3.3.2.1) (Stanimirova 2019). Any significant substitution in a mineral structure should affect the unit cell and thus be detectable in the XRD pattern. A closer look at the peak position of the (001) main reflex of Gordaite compared with the reference shows a shift of + 0.05 °2θ. This indicates an increase of the interlayer spacing along the c-axis due to the incorporation of heavy metals in the Gordaite structure. Cd is the only element that remains in the filtrate in significant concentrations. In the presence of anions, Cd forms complexes such as $CdCl^+$ and $CdSO_4$ that are highly water-soluble (Kubier et al. 2019). The presence of such complexes is most probably the reason for the elevated Cd concentrations in the filtrate.

After aging the precipitates, ZnO was identified as the main phase in the sample WW-G2_C2_24h_110 °C. The ZnO reflexes in the XRD pattern of sample WW-G2_C2_24h_110 °C shows slightly broadened ZnO reflexes suggesting nanocrystallinity (Holder and Schaak 2019). Compared to the reference, the relative intensity of the (100) reflex is almost as high as the (101) reflex of ZnO main peaks. These changes in the relative intensities of the main reflexes point (i) to preferred orientation or (ii) indicate a spherical shape of the ZnO nanoparticles (Holder and Schaak 2019). For clarification, SEM images of the residues should be taken. Within the application example presented in this section, these investigations would have gone beyond the scope.

In addition, traces of Willemite and Simonkolleite were observed in the XRD pattern. The presence of traces of Willemite is conclusive since the Si-concentration drops from initially approx. 78 mg/l to < 2 mg/l after precipitation. Looking at the FTIR-spectra of the sample, the relative intensity of Willemite bands are higher than that of ZnO, indicating that Willemite is the main phase. Regarding the reaction yield, the results of FTIR and XRD of sample WW-G2_C2_24h_110 °C are somewhat contrary. Considering the availability of the elements in the initial wastewater sample, Zn is with 1587.9 mg/l remarkably more concentrated than Si with 77.8 mg/l. This means that the relative amount of ZnO must be higher compared to Willemite. Compared to the fresh precipitate, the intensity of the O-H bands between 3000 – 4000 cm^{-1} decreased, indicating a lower amount of Gordaite, Namuwite, and Simonkolleite. Thus, combining XRD and FTIR results, it can be concluded that the precipitate after application of the aging method C2 is mainly crystalline and that ZnO is the main phase, confirmed by XRD measurements and the lower amount of O-H bands in FTIR. However, some bands in the FTIR spectrum could not be identified, which means that at least one more X-ray amorphous phase present in the precipitate could also contribute to the high band between 868 cm^{-1} and 977 cm^{-1}.

5.4.4.3. SPOP – an effective method for recovering Zn from MSWI fly ash?

The result of the two concepts confirms that the SPOP process is indeed a viable procedure to recover Zn from MSWI fly ash eluates. But it also shows the challenges that must be resolved in practice. Many aspects need to be realized, taking the needs of the end-user of the technology and the smelters into account:

- A viable method should be both, economically and environmentally feasible. This implies a low energy and low-cost recovery process.
- A robust process is required to handle the many impurities and contaminations in real wastewater after FLUWA, as well as the strong fluctuations in the concentrations of the heavy metals and the matrix elements (see chapter 2.4).
- For a successful recovery, the Zn content in the precipitate must be as high as possible,
- and the Cl concentration low, at least < 12 wt.-% of the dry mass substance, depending on local regulations (Annahmekatalog Qualitätsmerkmale Befesa Zinc Freiberg, Table A.5 in annex).
- Ideally, the proportion of hydroxides in the precipitates is low, and the filtrate meets the discharge limits after the treatment process.

With both processes, Concept C1 and C2, it was possible to precipitate ZnO as the main phase. Formation of ZnO means the enrichment of Zn in the residue while keeping the Cl-concentration low (< 12 wt.-% of the dry mass substance). However, the concepts were developed with synthetic wastewater and only tested with one wastewater each. To prove the robustness of the processes, the results must be confirmed with additional wastewater samples.

Table 5.17 shows the results of the direct precipitation method using WW-G1 and the aging method using WW-G2. In Concept C1, the direct precipitation method, Simonkolleite precipitates next to Zincite. This means the formation of a phase with a significant amount of Cl. In contrast, Concept C2, the aging method, leads to a significantly higher removal efficiency for Zn, as Simonkolleite and other hydroxides are detected only in traces. It is assumed that the treated wastewater of C2 complies with the direct discharge limit of 1 mg/l Zn. However, due to the detection limit of 2 mg/l for the salt-rich matrix, this cannot be said with certainty. With Concept C2, the concentrations of other heavy metals in the solution are also significantly lower than with the direct method (Concept C1); an exception is Cd, which forms complexes that remain in the solution.

The comparison shows that Concept C1, the direct precipitation of ZnO, depends strongly on the actual composition of the wastewater, and these impurities significantly affect the result. One explanation for this could be that when ZnO is precipitated directly from wastewater, the other elements are only incorporated into the ZnO structure to a limited extent. The substitution of Zn by other bi-valent heavy

metal ions is possible, as was shown by John et al. (2016d). Although, the concentration of the heavy metals in the wastewater might be too high to be completely incorporated into the ZnO structure, as the formation of a solid solution is limited.

Not so during the aging method. At first, Gordaite precipitates. The low heavy metal concentration indicates a high anion and cation exchange capacity of Gordaite, which results in most heavy metals being incorporated into the Gordaite structure. Furthermore, the results have shown that additional mineral phases precipitate from the solution. This depends on the concentration of the respective elements. Willemite precipitates, for example, if sufficient Si is available in the solution.

Table 5.17: Summary of the mineralogical characterization of the two Concepts C1 and C2 using real wastewater from MSWI Ingolstadt after application of FLUWA, including the Zn concentration in mg/l after the experiment and the calculated removal efficiency in %.

Concept	Zincite		Gordaite		Namuwite		Simonkolleite		Goethite		Halite		Willemite		Zn-removal
	ZnO		$NaZn_4(SO_4)(OH)_6Cl \cdot 6H_2O$		$Zn_4(SO_4)(OH)_6 \cdot 4H_2O$		Zn(OH)Cl		FeO(OH)		NaCl		$ZnSiO_4$		
	XRD	IR	XRD	IR	XRD	IR	XRD	IR	XRD	IR	XRD	IR	XRD	IR	%
C1	++	+++	-	+	-	+	++	+	-	(+)	(+)	-	-	-	99.2
C2	+++	+	-	+	-	+	(+)	+	-	-	-	-	+	++	99.9

The successful implication of the SPOP process depends crucially on the reaction conditions. Therefore, to realize the developed SPOP process in practice, a quick and easy method is needed to evaluate whether the precipitation process was successful or not during the operation of a pilot plant or on an industrial scale. A suitable method could be Eh-pH diagrams, where the stability fields of the minerals are plotted as a function of Eh and pH. By recording the Eh and pH during the precipitation process, one can estimate the product phase. The results in the model system were plotted in two Eh-pH diagrams, one for temperatures ≤ 40 °C (Figure 5.41a) and the other for temperatures > 40 °C (Figure 5.41b) to test the applicability of the Eh-pH diagrams as a monitoring tool. They represent the conditions for Cl-concentrations > 70000 mg/l, SO_4 concentrations 2200 - 5440 mg/l, and sufficiently available oxygen, Na, Ca, and Zn in the solution. The list of the used data can be found in Tables A.3 and A.4 in the annex. The mineral fields in the figures are based solely on available data so that the actual stability limits may differ slightly.

At temperatures ≤ 40 °C, Gordaite has a large stability field at Cl concentrations > 70000 mg/l and precipitates within the range pH 8.7 – pH 10.8 with sufficient oxygen in the system. The stability field of ZnO is very narrow because, at pH > 11.3, Ca-Zincate ($CaZn_2(OH)_6 \cdot 2H_2O$) is stable. At temperatures > 40 °C, the stability field of ZnO enlarges and shifts to lower pH values.

Accordingly, by increasing the temperature, costs for chemicals could be saved since less NaOH is needed for alkalization to a lower pH. It is expected that the stability fields are similar at lower Eh conditions.

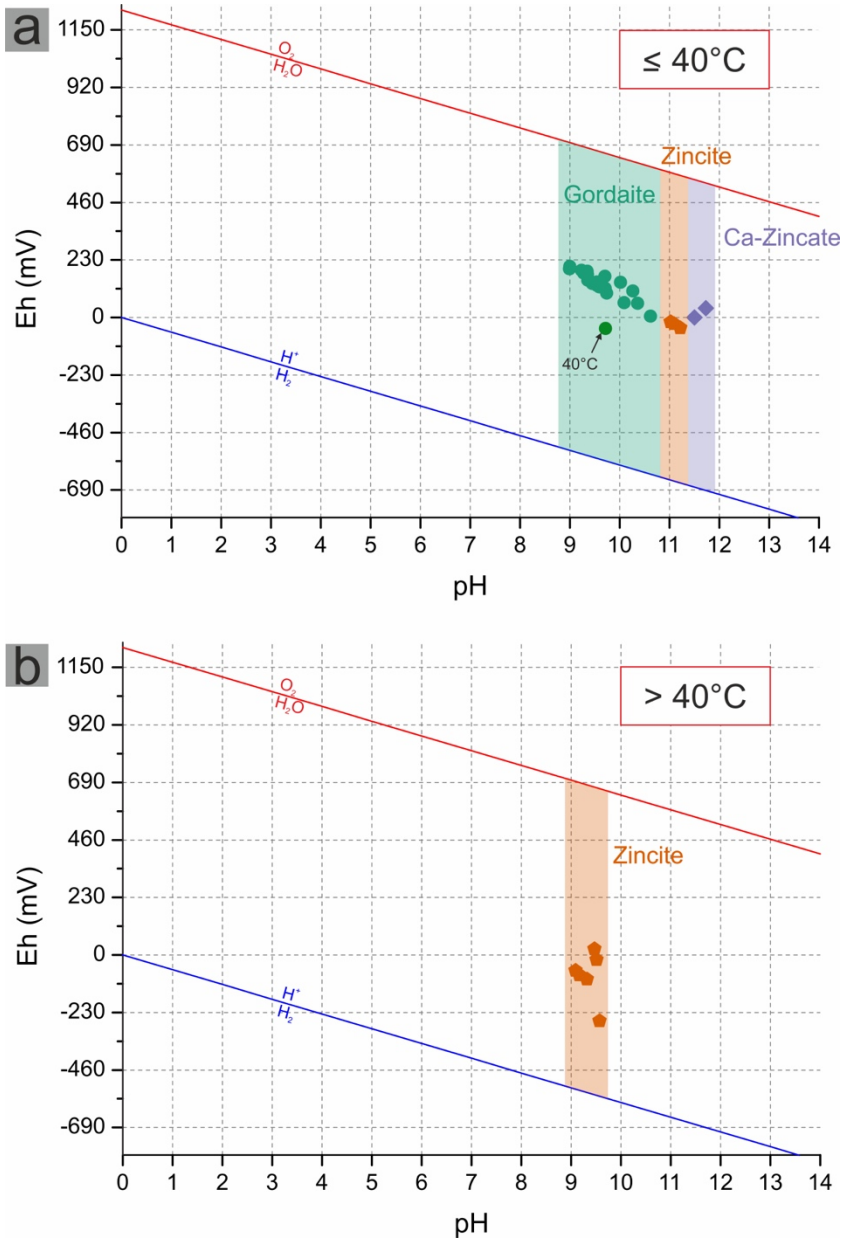

Figure 5.41: Empirical Eh-pH diagrams of Zn phases at a) < 40 °C and b) > 40 °C with Cl-concentrations > 70000 mg/l, SO_4 concentrations 2200 – 5440 mg/l, and sufficiently available oxygen, Na, Ca, and Zn. The data points that are the basis for this stability diagram can be found in Tables A.3 and A.4 in the annex.

The applicability of the diagram as a monitoring tool is checked with the result of the real wastewater WW-G1. In this experiment Concept C1 was applied at 70 °C. The Eh and pH value measured after the experiment plots in Figure 5.42 (red star) within the orange ZnO stability field > 40 °C. The negative Eh value is most likely due to organic substances in the real wastewater, which lower the Eh-value through oxidation. That ZnO is the main phase is confirmed by the analyses.

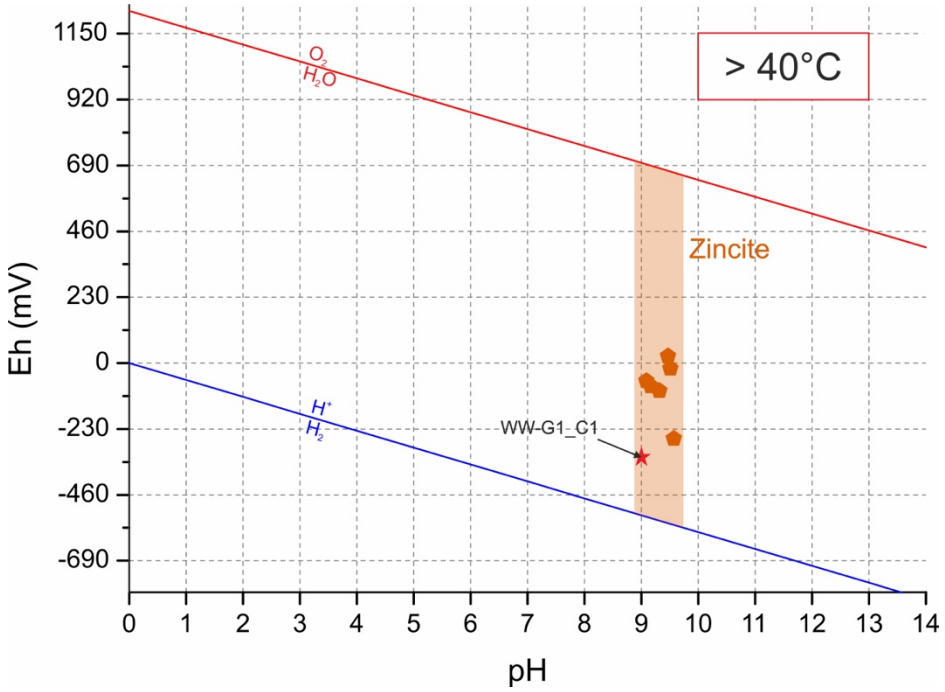

Figure 5.42: Empirical Eh-pH diagram of Zn phases at Cl-concentrations > 70000 mg/l, SO_4 concentrations 2200 - 5440 mg/l, and sufficiently available Na, Ca, and Zn in the solution. The red star refers to the Eh and pH value of experiment WW-G1_C1. The data points that are the basis for the stability diagram can be found in Table A.4 in the annex.

Accordingly, the measurement of Eh-pH values can be a suitable method to control the successful implementation of the process. However, it also shows that for practical purposes, accurate mapping of the stability fields of the minerals is essential in dependence of temperature, regardless of the fact that it is necessary for determining the optimal reaction conditions.

6. Conclusion and outlook

The term “waste” has continuously changed over time: what has been considered as waste and thus worthless for years and decades is in a new context valuable, sometimes out of necessity, often for economic reasons and, recently, for reasons of sustainability (Keller 2009). Today, MSWI fly ash is regarded as hazardous waste due to its high content of easily soluble salts, heavy metals, and POPs. It is therefore disposed of in special landfills, either directly or after processing by S/S techniques, or it is recycled underground as filler. Several studies dealt with the use fly ash as a raw material substitute (e.g., as an additive in cement) with the aim to save landfill space (Stegemann 2014; Quina et al. 2018). However, only small quantities of ash can be added as an aggregate without negatively affecting the properties of the respective products. In addition, toxic heavy metals are introduced into the material cycle, making subsequent recycling of, e.g., building materials problematic. It also leads to the loss of metals like Zn as a resource due to dissipation.

A comparison with primary raw materials highlights the enormous potential of fly ash from municipal waste as an anthropogenic resource. The Zn-content of natural low-grade ores is 2,5 % (Sverdrup et al. 2019), whereas the Zn content in fly ash can be as high as 7 % (see chapter 2.4). In 2017, 26.4 million tons of waste were thermally treated in Germany (ITAD Jahresbericht 2019). With a fly ash proportion of 1 - 5 wt.-% of the original waste input (see chapter 2.2), this means that between 264000 and 1´320000 tons of fly ash were generated by waste incineration in 2017. Assuming an average Zn content of only 2.5 % in the fly ash - comparable to low-grade Zn-ores - this results in a quantity of 6600 - 33000 tons of Zn per year that are lost only in Germany.

This means viable methods are required for an effective recovery of the resources contained in fly ash. In this respect, the gas cleaning system has a massive influence on the efficiency of such a process. The addition of milk of lime to fly ash in dry/semi-dry FGT dilutes the heavy metal content in the ash considerably, making metal recovery unprofitable. Not so with wet flue gas scrubbing. The often-cited disadvantage of this process – the formation of an acidic solution – can be used to mobilize the metals from the fly ash. As demonstrated by the FLUWA (acidic fly ash washing) process (see chapter 3.3.1), Zn, Pb, Cd, and Cu can be leached from the fly ash by optimizing the leaching conditions. However, treatment of the metals-enriched solution with milk of lime leads to a considerable increase in the volume of the residue and causes a reduction in the metal concentration in the neutralization sludge. This makes the recovery of metals uneconomical and the sludge a hazardous waste.

Only a few processes, such as FLUREC (fly ash recycling), were developed to treat salt-rich leachate from fly ash, with a focus on recovering Zn as high purity metal. However, it is also a complex and energy-intensive process. The SPOP (Specific Product-Oriented Precipitation) procedure presented in this thesis provides a low-cost alternative. Two novel processes have been developed to precipitate

ZnO from saline AQ. The precipitation of the phases depends strongly on the reaction conditions. At room temperature, Gordaite is the stable phase. By optimizing the reaction conditions, it is possible to synthesize ZnO as a single-phase directly a) at temperatures ≥ 60 °C with medium alkalization rate A2 or b) at lower temperatures < 40 °C by increasing the alkalization rate (see chapter 5.2). It is also possible to obtain ZnO in a two-step process by aging previously synthesized Gordaite in suspension (see chapter 5.3) by a dissolution-precipitation reaction. Gordaite is not stable at ≥ 80 °C (without stirring). At 110 °C and without stirring, Gordaite completely transforms to ZnO within 3 h. In general, the higher the aging temperature, the faster the transformation reaction. Stirring during aging can accelerate the dissolution-precipitation reaction to form ZnO and thereby lowers the aging temperature.

Based on the results in the model system, two concepts were developed and tested with real wastewater from MSWI plant Ingolstadt in chapter 5.4. Concept 1 (direct precipitation method) aims to precipitate ZnO directly from the wastewater and Concept 2 (aging method) is a two-step process, where ZnO is obtained by aging previously synthesized Gordaite at elevated temperatures. The case studies in chapter 5.4 confirm that the two Concepts C1 (direct precipitation method) and C2 (aging method) developed in the model system can be applied to real wastewater from MSWI. ZnO is the main phase in both methods. This represents the first step towards a viable industrial process. By precipitating mainly ZnO, Zn is enriched in the residue, while the Cl-concentration remains low (at least < 12 wt.-% of the dry mass substance, depending on local regulations), which is a prerequisite for the successful recycling of the residues. These results must be confirmed with different wastewater samples of varying compositions to prove the robustness of the process.

The next step is to build a pilot plant to test the feasibility of both processes on a larger scale. Simultaneously, the laboratory experiments are to be continued in order to record the expansion of the stability fields of the phases in the Eh-pH diagram in dependence of temperature. Based on the results, the method with the better economic viability and the least environmental impact can be determined. This step requires cooperation with a plant manufacturer and close collaboration with the user, the MSWI plant, and potential recyclers. Contact with the recyclers is necessary to confirm that the residues produced by SPOP can be recycled. An evaluation of the SPOP process with life cycle assessment enables the environmental impact of this process to be compared with that of FLUREC process. Such innovative concepts which meet the criteria of circular economy (Helbig et al. 2020) in consideration of the sustainable development goals (SDG) contribute to save primary raw materials and avoid hazardous waste. The recovery of valuable materials from anthropogenic sources in order to reintroduce them into production helps to close the gap in the circular economy and is thus an important step towards an “industrial ecosystem” (Stegemann 2014).

The comparison of the leachate wastewaters from Germany and Switzerland according to FLUWA has shown that an optimized FLUWA remarkably increases the concentration of the heavy metals in the eluate, e.g., by adding H_2O_2 as an oxidizing agent (see chapter 4.1.2). This means that for an optimal use of the anthropogenic resource fly ash, also the FLUWA process must be optimized. This has two advantages; it effectively depletes the metals in the fly ash and enriches the metals in the eluate, which increases the ZnO yield when applying the SPOP process.

The results of this thesis offer another area in which SPOP can be applied. It can be used as an innovative synthesis method for ZnO, Gordaite, Namuwite, and Bechererite from Zn containing Cl-rich solutions. In the case of ZnO, the structural parameters of the nanoparticles such as particle size, defects, and doping directly affect the optical and electrical properties and, thus, the application of the nanoparticles (Fang 2016). The new synthesis methods for nanocrystalline ZnO presented in this thesis are very promising because they are simple, fast, and inexpensive. The results show that the morphology of the particles changes with reaction conditions. Therefore, a systematic study of the relationship between the SPOP-precipitation conditions and the morphological and structural parameters should be carried out. A deeper understanding of these relationships enables the production of technologically interesting ZnO nanoparticles. A promising application of Cu-doped ZnO nanoparticles would be, for example, as a catalyst for the hydrogenation of CO or CO_2 to methanol (Studt et al. 2015; Kattel et al. 2017).

Both minerals, Gordaite and Namuwite, have unique properties regarding their ion exchange capacity. Among other things, they are also discussed as corrosion protection. These minerals can be synthesized much faster and easier using SPOP. Compared to the usual synthesis duration of 5 days for both minerals, the precipitation using SPOP is completed within 10 minutes. Besides the educts for synthesis, only NaOH is needed. The synthesis procedure for these minerals can be further optimized in order to increase the efficiency of this process, e.g., by saving chemicals. As a next step, the ion exchange properties of the minerals should be determined with a focus on Cd, Cu, and Pb because these elements are the most abundant in MSWI fly ash. This approach implies a detailed study of the structure of Gordaite and Namuwite synthesized with SPOP.

According to current knowledge, the synthesis of Bechererite was carried out for the first time in the laboratory. The optimal conditions for synthesis must be determined in order to obtain Bechererite as a single phase. The most promising results were obtained in the Zn system with medium salinity (chapter 5.1, Set 1). This allows the structure and stability of Bechererite, as well as possible applications, to be examined in detail. The possibility of preparing the mineral very easily under controlled laboratory conditions can also help to get a better understanding about the alteration processes in nature leading to Bechererite as a secondary mineral.

Literature

Abanades, S., Flamant, G., Gagnepain, B., and Gauthier, D. (2002) Fate of heavy metals during municipal solid waste incineration. Waste Management & Research, 20, 55–68.

Abdelmohsen, A.H., Rouby, W.M.A. El, Ismail, N., and Farghali, A.A. (2017) Morphology Transition Engineering of ZnO Nanorods to Nanoplatelets Grafted Mo_8O_{23}-MoO_2 by Polyoxometalates: Mechanism and Possible Applicability to other Oxides. Scientific Reports, 7, 5946.

Adiwidjaja, G., Friese, K., Klaska, K.H., and Schlüter, J. (1997) The crystal structure of Gordaite $NaZn_4(SO_4)(OH)_6Cl \cdot 6H_2O$. Zeitschrift fur Kristallographie - New Crystal Structures, 212, 704–707.

Al-Fori, M., Dobretsov, S., Myint, M.T.Z., and Dutta, J. (2014) Antifouling properties of zinc oxide nanorod coatings. Biofouling, 30, 871–882.

Almeida, E., Morcillo, M., and Rosales, B. (2000) Atmospheric corrosion of zinc Part 1: Rural and urban atmospheres. British Corrosion Journal, 35, 284–288.

Anagnostopoulos, I., and Heuss-Aßbichler, S. (2021) Residues of Industrial Wastewater Treatment: Hazardous Waste or Anthropogenic Resource? In H. Pöllmann, Ed., Industrial wastes - Characterization, Modification and Applications of Residues pp. 403–432. De Gruyter, Berlin, Boston.

Anthony, J.W., Bideaux, R.A., Bladh, K.W., and Nichols, M.C. (1997a) Gordaite. In J.W. Anthony, R.A. Bideaux, K.W. Bladh, and M.C. Nichols, Eds., Handbook of Mineralogy. Mineralogical Society of America, Chantilly.

——— (1997b) Namuwite. In J.W. Anthony, R.A. Bideaux, K.W. Bladh, and M.C. Nichols, Eds., Handbook of Mineralogy. Mineralogical Society of America, Chantilly.

——— (1997c) Simonkolleite. In J.W. Anthony, R.A. Bideaux, K.W. Bladh, and M.C. Nichols, Eds., Handbook of Mineralogy. Mineralogical Society of America, Chantilly.

Ao, W., Li, J., Yang, H., Zeng, X., and Ma, X. (2006) Mechanochemical Synthesis of Zinc Oxide Nano Crystalline. Powder Technology, 168, 148–151.

Arizaga, G.G.C., Satyanarayana, K.G., and Wypych, F. (2007) Layered hydroxide salts: Synthesis, properties and potential applications. Solid State Ionics, 178, 1143–1162.

Bacaksiz, E., Parlak, M., Tomakin, M., Özçelik, A., Karakız, M., and Altunbaş, M. (2008) The effects of zinc nitrate, zinc acetate and zinc chloride precursors on investigation of structural and optical properties of ZnO thin films. Journal of Alloys and Compounds, 466, 447–450.

Baruah, S., and Dutta, J. (2009) Hydrothermal growth of ZnO nanostructures. Science and Technology of Advanced Materials, 10.

Bayuseno, A.P., Schmahl, W.W., and Müllejans, T. (2009) Hydrothermal processing of MSWI Fly Ash-towards new stable minerals and fixation of heavy metals. Journal of Hazardous Materials, 167, 250–259.

Bear, I., Grey, I.E., Newnham, I.E., and Rogers, L.J. (1987) The $ZnSO_4$ $3Zn(OH)_2$-H_2O System. I Phase Formation. Australian Journal of Chemistry, 40, 539–556.

Belevi, H., and Moench, H. (2000) Factors Determining the Element Behavior in Municipal Solid Waste Incinerators. 1. Field Studies. Environmental Science & Technology, 34, 2501–2506.

Benassi, L., Pasquali, M., Zanoletti, A., Dalipi, R., Borgese, L., Depero, L.E., Vassura, I., Quina, M.J., and Bontempi, E. (2016) Chemical Stabilization of Municipal Solid Waste Incineration Fly Ash without Any Commercial Chemicals: First Pilot-Plant Scaling Up. ACS Sustainable Chemistry and Engineering.

von Bezing, L., Bode, R., and Jahn, S. (2008) Namibia Minerals and Localities. Edition Schluss Freudenstein, Bode Verlag GmbH, Haltern.

Bing, X., Bloemhof, J.M., Ramos, T.R.P., Barbosa-Povoa, A.P., Wong, C.Y., and van der Vorst, J.G.A.J. (2016) Research challenges in municipal solid waste logistics management. Waste Management, 48, 584–592.

Bogush, A., Stegemann, J.A., Wood, I., and Roy, A. (2015) Element composition and mineralogical characterisation of air pollution control residue from UK energy-from-waste facilities. Waste Management, 36, 119–129.

Bogush, A., Stegemann, J., J., Z., Wang, Z., Zhang, B., Zhang, T., Zhang, W., and Wei, J. (2020) Co-processing of raw and washed air pollution control residues from energy-from-waste facilities in the cement kiln. Journal of Cleaner Production, 254.

Bontempi, E., Zacco, A., Borgese, L., Gianoncelli, A., Ardesi, R., and Depero, L.E. (2010) A new method for municipal solid waste incinerator (MSWI) fly ash inertization, based on colloidal silica. Journal of Environmental Monitoring, 12, 2093–2099.

Bourguignon, D. (2018) Circular economy package: Four legislative proposals on waste. online: https://www.europarl.europa.eu/RegData/etudes/BRIE/2018/625108/EPRS_BRI(2018)625108_EN.pdf, date accessed 07.09.2021.

Bowles, J.F.W., Suárez, S., Prichard, H.M., and Fisher, P.C. (2018) The mineralogy, geochemistry and genesis of the alluvial platinum-group minerals of the Freetown Layered Complex, Sierra Leone. Mineralogical Magazine, 82, S223–S246.

Brugger, J. (2003) Formation of Willemite in Hydrothermal Environments. Economic Geology, 98, 819–835.

Bunge, R. (2014) Wieviel Metall steckt im Abfall? Mineralische Nebenprodukte und Abfälle - Aschen, Schlacken, Stäube und Baurestmassen, 91–104.

Burns, P.C., Roberts, A.C., and Nikischer, A.J. (1998) The crystal structure of $Ca[Zn_8(SO_4)_2(OH)_{12}Cl_2](H_2O)_9$, a new phase from slag dumps at Val Varenna, Italy. European Journal of Mineralogy, 10, 923–930.

Chandler, J.A., Eighmy, T.T., Hartlén, J., Hjelmar, O., Kosson, D.S., Sawell, S.E., Van Der Sloot, H.A., and Vehlow, J. (1997) Municipal solid waste incinerator residues, 973 p. Elsevier Ltd, Amsterdam.

Chang, F.-Y., and Wey, M.-Y. (2006) Comparison of the characteristics of bottom and fly ashes generated from various incineration processes. Journal of Hazardous Materials, 138, 594–603.

Chen, C., Liu, P., and Lu, C. (2008) Synthesis and characterization of nano-sized ZnO powders by direct precipitation method. Chemical Engineering Journal, 144, 509–513.

Chen, X., Song, X., Qiao, W., Zhang, X., Sun, Y., Xu, X., Zhong, W., and Du, Y. (2016) Solvent-directed and anion-modulated self-assemblies of nanoparticles: a case of ZnO. CrystEngComm, 18, 9139–9151.

Chen, Y.Y., Chung, S.C., and Shih, H.C. (2006) Studies on the initial stages of zinc atmospheric corrosion in the presence of chloride. Corrosion Science, 48, 3547–3564.

Choi, K., Kang, T., and Oh, S.-G. (2012) Preparation of disk shaped ZnO particles using surfactant and their PL properties. Materials Letters, 75, 240–243.

Choy, J.-H., and Park, M. (2004) Cationic and Anionic clays for biological applications. In K.G. Satyanarayana and F. Wypych, Eds., Clay Surfaces: Fundamentals and Applications pp. 403–424. Elsevier.

Chukanov, N. V. (2014) Infrared spectra of mineral species, 1st ed., 1726 p. Springer Netherlands, Netherlands.

Cole, I.S., Muster, T.H., Furman, S.A., Wright, N., and Bradbury, A. (2008) Products formed during the interaction of seawater droplets with zinc surfaces: I. Results from 1- and 2.5-day exposures. Journal of the Electrochemical Society, 155, 244–255.

Delcheva, Z., Stanimirova, T., Petrova, N., and Tacheva, E. (2019) Thermal decomposition of bromine gordaite: $NaZn_4(OH)_6(SO_4)Br{\cdot}6H_2O$. Journal of Thermal Analysis and Calorimetry, 5.

Dietrich, H.G., and Johnston, J. (1927) Equilibrium between crystalline zinc hydroxide and aqueous solutions of ammonium hydroxide and of sodium hydroxide. Journal of the American Chemical Society, 49, 1419–1431.

Diler, E., Rouvellou, B., Rioual, S., Lescop, B., Nguyen Vien, G., and Thierry, D. (2014) Characterization of corrosion products of Zn and Zn-Mg-Al coated steel in a marine atmosphere. Corrosion Science, 87, 111–117.

Dinnebier, R.E., and Billinge, S.J. (2008) Principles of powder diffraction. In R.E. Dinnebier and S.J. Billinge, Eds., Powder Diffraction: Theory and Practice pp. 1–19. RSC Publishing, Cambridge, UK.

Dou, X., Ren, F., Nguyen, M.Q., Ahamed, A., Yin, K., Chan, W.P., and Chang, V.W.C. (2017) Review of MSWI bottom ash utilization from perspectives of collective characterization, treatment and existing application. Renewable and Sustainable Energy Reviews, 79, 24–38.

Downs, R.T., and Hall-Wallace, M. (2003) The American Mineralogist Crystal Structure Database. American Mineralogist, 88.

EU (2008) Directive 2008/98/EC of the European Parliament and of the Council of 19 November 2008 on waste and repealing certain Directives – Statement of the European Parliament and the Council of the European Union.

Eurostat (2021) Municipal waste by waste management operations (env_wasmun), Reference Metadata in Euro SDMX Metadata Structure (ESMS), online: https://ec.europa.eu/eurostat/cache/metadata/en/env_wasmun_esms.htm, date accessed 07.09.2021.

Evans, J., and Williams, P.T. (2000) Heavy metal adsorption onto flyash in waste incineration flue gases. In 2nd International Symposium on Incineration and Flue Gas Treatment Technologies, 78, 40–46. Sheffield.

Fang, Y. (2016) Structural Parameters (Size, Defect and Doping) of ZnO Nanostructures and Relations with their Optical and Electrical Properties. Technische Universität Ilmenau.

Ferreira, C., Ribeiro, A., and Ottosen, L. (2003) 49 Possible applications for municipal solid waste fly ash. Journal of hazardous materials, 96, 201–216.

Geels, F.W., and Schot, J. (2007) Typology of sociotechnical transition pathways. Research Policy, 36, 399–417.

Gelaude, P., Rewitzer, C., and van Kalmthout, P. (1996) Laurion : the minerals in the ancient slags. Nijmegen.

Gharoy Ahangar, E., Abbaspour-Fard, M.H., Shahtahmassebi, N., Khojastehpour, M., and Maddahi, P. (2015) Preparation and Characterization of PVA/ZnO Nanocomposite. Journal of Food Processing and Preservation, 39, 1442–1451.

Gianoncelli, A., Zacco, A., Struis, R.P.W.J., Borgese, L., Depero, L.E., and Bontempi, E. (2013) Fly Ash Pollutants, Treatment and Recycling. In E. Lichtfouse, J. Schwarzbauer, and D. Robert, Eds., Pollutant Diseases, Remediation and Recycling pp. 103–213. Springer International Publishing, Cham.

Giester, G., and Rieck, B. (1996) Bechererite, $(Zn,Cu)_6Zn_2(OH)_{13}[(S,Si)(O,OH)_4]_2$, a novel mineral species from the Tonopah-Belmont mine, Arizona. American Mineralogist, 81, 244–248.

Gorodylova, N., Cousy, S., Šulcová, P., and Svoboda, L. (2017) Thermal transformation of layered zinc hydroxide chloride: A review. Journal of Thermal Analysis and Calorimetry, 127, 675–683.

Gražulis, S., Chateigner, D., Downs, R.T., Yokochi, A.F.T., Quirós, M., Lutterotti, L., Manakova, E., Butkus, J., Moeck, P., and Le Bail, A. (2009) Crystallography Open Database (COD): an open-access collection of crystal structures. Journal of Applied Crystallography, 42, 726–729.

Gražulis, S., Daškevič, A., Merkys, A., Chateigner, D., Lutterotti, L., Quirós, M., Serebryanaya, N.R., Moeck, P., Downs, R.T., and Le Bail, A. (2012) Crystallography Open Database (COD): an open-access collection of crystal structures and platform for world-wide collaboration. Nucleic Acids Research, 40, D420–D427.

Gražulis, S., Merkys, A., Vaitkus, A., and Okulič-Kazarinas, M. (2015) Computing stoichiometric molecular composition from crystal structures. Journal of Applied Crystallography, 48, 85–91.

Groat, L.A. (1996) The crystal structure of Namuwite, a mineral with Zn in tetrahedral and octahedral coordination, and its relationship to the synthetic basic zinc sulfates. American Mineralogist, 81, 238–243.

Haberl, J., Koralewska, R., Schlumberger, S., and Schuster, M. (2018) Quantification of main and trace metal components in the fly ash of waste-to-energy plants located in Germany and Switzerland: An overview and comparison of concentration fluctuations within and between several plants with particular focus on valuable metals. Waste Management, 75, 361–371.

Hagemann, S. (2012) Entwicklung eines thermodynamischen Modells für Zink, Blei und Cadmium in salinaren Lösungen. Köln.

Harris, D.C. (2014) Lehrbuch der Quantitativen Analyse, 8th ed., 977 p. (G. Werner & T. Werner, Eds.). Springer Verlag, Berlin, Heidelberg.

Hausner, D.B., Bhandari, N., Pierre-Louis, A.-M., Kubicki, J.D., and Strongin, D.R. (2009) Ferrihydrite reactivity toward carbon dioxide. Journal of Colloid and Interface Science, 337, 492–500.

Hawthorne, F., and Schindler, M. (2000) Topological enumeration of decorated $[Cu^{2+}\phi_2]_N$ sheets in hydroxy-hydrated copper-oxysalt minerals. Canadian Mineralogist, 38, 751–761.

Hawthorne, F.C., and Sokolova, E. (2002) Simonkolleite, $Zn_5(OH)_8Cl_2(H_2O)$, a decorated interrupted-sheet structure of the form $[M\phi_2]_4$. The Canadian Mineralogist, 40, 939–946.

He, P., Gao, X.D., Wu, L. Bin, Jiang, Z.W., Wang, C.L., and Li, X.M. (2013) Porous ZnO sheets transformed from zinc sulfate hydroxide hydrate and their photoluminescence performance. Acta Physico - Chimica Sinica, 29, 874–880.

Helbig, C., Thorenz, A., and Tuma, A. (2020) Quantitative assessment of dissipative losses of 18 metals. Resources, Conservation and Recycling, 153.

Heuss-Aßbichler, S., and John, M. (2017) Gold, silver, and copper in the geosphere and anthroposphere: Can industrial wastewater act as an anthropogenic resource? In S. Heuss-Aßbichler, G. Amthauer, and M. John, Eds., Highlights in Applied Mineralogy pp. 137–151. De Gruyter.

Heuss-Aßbichler, S., and Rettenberger, G. (2016) Geschichte der Deponie – ist Deponie Geschichte? In J. Kersten, Ed., Inwastement - Abfall in Umwelt und Gesellschaft pp. 109–130. Transcript Verlag, Bielefeld.

Heuss-Aßbichler, S., Magel, G., and Fehr, K.T. (2010) Abiotic hydrogen production in fresh and altered MSWI-residues: Texture and microstructure investigation. Waste Management, 30, 1871–1880.

Heuss-Aßbichler, S., John, M., and Huber, A. (2016a) A new procedure for recovering heavy metals in industrial wastewater. In WIT Transactions on Ecology and The Environment. WIT Press, Southampton, UK.

Heuss-Aßbichler, S., John, M., Klapper, D., Bläß, U.W., and Kochetov, G. (2016b) Recovery of copper as zero-valent phase and/or copper oxide nanoparticles from wastewater by ferritization. Journal of Environmental Management, 181, 1–7.

Hjelmar, O. (1996) Disposal strategies for municipal solid waste incineration residues. Journal of Hazardous Materials, 47, 345–368.

Hoffmann, C., Armbruster, T., and Giester, G. (1997) Acentric structure (P3) of bechererite,

$Zn_7Cu(OH)_{13}[SiO(OH)_3SO_4]$. American Mineralogist, 82, 1014–1018.

Holder, C.F., and Schaak, R.E. (2019) Tutorial on Powder X-ray Diffraction for Characterizing Nanoscale Materials. ACS Nano, 13, 7359–7365.

Huang, T.Y., and Chuieh, P.T. (2015) Life Cycle Assessment of Reusing Fly Ash from Municipal Solid Waste Incineration. Procedia Engineering, 118, 984–991.

Huber, A., John, M., and Heuss-Aßbichler, S. (2016) Is an effective recovery of heavy metals from industrial effluents feasible? In Recy&Depotech. Leoben.

Huber, F., Laner, D., and Fellner, J. (2018) Comparative life cycle assessment of MSWI fly ash treatment and disposal. Waste Management, 73, 392–403.

Hyks, J., Astrup, T., and Christensen, T.H. (2009) Long-term leaching from MSWI air-pollution-control residues: Leaching characterization and modeling. Journal of Hazardous Materials, 162, 80–91.

ITAD (2019) Jahresbericht Interessengemeinschaft der Thermischen Abfallbehandlungsanlagen in Deutschland. online https://www.itad.de/service/downloads/itad-jahresbericht-2019-webformat.pdf, date accessed: 07.09.2021.

Jahn, S., and Witzke, T. (1999) Secondary Minerals of Zinc and Copper in Heaps of Kupferschiefer Ores at Helbra, Sachsen-Anhalt, Germany: First Occurence of Cuprian Gordaite. Chemie der Erde, 59, 223–232.

John, M. (2016) Low temperature synthesis of nano crystalline zero-valent phases and (doped) metal oxides as $A_xB_{3-x}O_4$ (ferrite), ABO_2 (delafossite), A_2O and AO. A new process to treat industrial wastewaters? Ludwig-Maximilians-Universität München.

John, M., Heuss-Aßbichler, S., and Ullrich, A. (2016a) Conditions and mechanisms for the formation of nano-sized Delafossite ($CuFeO_2$) at temperatures ≤ 90 °C in aqueous solution. Journal of Solid State Chemistry, 234, 55–62.

John, M., Heuss-Aßbichler, S., Park, S.-H., Ullrich, A., Benka, G., Petersen, N., Rettenwander, D., and Horn, S.R. (2016b) Low-temperature synthesis of $CuFeO_2$ (delafossite) at 70°C: A new process solely by precipitation and ageing. Journal of Solid State Chemistry, 233, 390–396.

John, M., Heuss-Aßbichler, S., Ullrich, A., and Rettenwander, D. (2016c) Purification of heavy metal loaded wastewater from electroplating industry under synthesis of delafossite (ABO_2) by “Lt-delafossite process.” Water Research, 100, 98–104.

John, M., Heuss-Aßbichler, S., and Ullrich, A. (2016) Recovery of Zn from wastewater of zinc plating industry by precipitation of doped ZnO nanoparticles. International Journal of Environmental

Science and Technology, 13, 2127–2134.

John, M., Heuss-Aßbichler, S., Tandon, K., and Ullrich, A. (2017) Recovery of Ag and Au from synthetic and industrial wastewater by 2-step ferritization and Lt-delafossite process via precipitation. Journal of Water Process Engineering, 30, 100532.

Jordan, M.M., Rincón, J.M., and Rincón-Mora, B. (2015) Rustic ceramic covering tiles obtained by recycling of marble residues and MSW fly ash. Fresenius Environmental Bulletin, 24, 533–538.

Karlfeldt Fedje, K., Ekberg, C., Skarnemark, G., and Steenari, B.M. (2010) Removal of hazardous metals from MSW fly ash-An evaluation of ash leaching methods. Journal of Hazardous Materials, 173, 310–317.

Karlfeldt Fedje, K., Ekberg, C., Skarnemark, G., Pires, E., and Steenari, B.-M. (2012) Initial studies of the recovery of Cu from MSWI fly ash leachates using solvent extraction. Waste Management & Research, 30, 1072–1080.

Kasatkin, A. V, Plášil, J., Škoda, R., Belakovskiy, D.I., Marty, J., Meisser, N., and Pekov, I. V (2018) Redefinition of thérèsemagnanite, $NaCo_4(SO_4)(OH)_6Cl{\cdot}6H_2O$: new data and relationship to 'cobaltogordaite.' Mineralogical Magazine, 82, 159–170.

Kattel, S., Ramírez, P.J., Chen, J.G., Rodriguez, J.A., and Liu, P. (2017) Active sites for CO_2 hydrogenation to methanol on Cu/ZnO catalysts. Science, 355, 1296–1299.

Keller, R. (2009) Müll- Die gesellschaftliche Konstruktion des Wertvollen, 2nd ed., 329 p. VS Verlag für Sozialwissenschaften, Wiesbaden.

Kizinievich, O., Voishniene, V., Kizinievich, V., and Shkamat, E. (2019) Effect of Municipal Solid Waste Incineration Fly Ash on the Properties, Durability, and Environmental Toxicity of Fired Aluminosilicates. Glass and Ceramics, 76, 307–310.

Kolodziejczak-Radzimska, A., and Jesionowski, T. (2014) Zinc oxide-from synthesis to application: A review. Materials, 7, 2833–2881.

Kubier, A., Wilkin, R.T., and Pichler, T. (2019) Cadmium in soils and groundwater: A review. Applied Geochemistry, 108.

Lafuente, B., Downs, R.T., Yang, H., and Stone, N. (2015) The power of databases: The RRUFF project. In T. Armbruster and R.M. Danisi, Eds., Highlights in Mineralogical Crystallography pp. 1–30. De Gruyter, Berlin.

Le Bail, A. (2008) The profile of a Bragg reflection for extracting intensities. In R.E. Dinnebier and S.J. Billinge, Eds., Powder Diffraction: theory and practice pp. 134–165. RSC Publishing, Cambridge, UK.

Leal, D.A., Machado Silva, G., Tedim, J., Wypych, F., and Marino, C.E.B. (2020) Synthesis and characterization of gordaite, osakaite and simonkolleite by different methods: Comparison, phase interconversion, and potential corrosion protection applications. Journal of Solid State Chemistry, 291, 121595.

Lechner, P., Mostbauer, P., and Böhm, K. (2010) Grundlagen für die Verwertung von MV-Rostasche. Teil A: Entwicklung des Österreichischen Behandlungsgrundsatzes, 81 p. Wien.

Liang, W., Li, W., Chen, H., Liu, H., and Zhu, L. (2015) Exploiting electrodeposited flower-like $Zn_4(OH)_6SO_4{\cdot}4H_2O$ nanosheets as precursor for porous ZnO nanosheets. Electrochimica Acta, 156, 171–178.

Luo, H., Cheng, Y., He, D., and Yang, E.-H. (2019) Review of leaching behavior of municipal solid waste incineration (MSWI) ash. Science of The Total Environment, 668, 90–103.

Machovsky, M., Kuritka, I., Sedlak, J., and Pastorek, M. (2013) Hexagonal ZnO porous plates prepared from microwave synthesized layered zinc hydroxide sulphate via thermal decomposition. Materials Research Bulletin, 48, 4002–4007.

Makarichi, L., Jutidamrongphan, W., and Techato, K. (2018) The evolution of waste-to-energy incineration: A review. Renewable and Sustainable Energy Reviews, 91, 812–821.

Maruyama, S.A., Westrup, K.C.M., Nakagaki, S., and Wypych, F. (2017a) Immobilization of a cationic manganese(III) porphyrin on lithium gordaite ($LiZn_4(OH)_6(SO_4)Cl{\cdot}6H_2O$), a layered hydroxide salt with cation exchange capacity. Applied Clay Science, 139, 108–111.

Maruyama, S.A., Krause, F., Filho, S.R.T., Leitão, A.A., and Wypych, F. (2017b) Synthesis, cation exchange and dehydration/rehydration of sodium gordaite: $NaZn_4(OH)_6(SO_4)Cl{\cdot}6H_2O$. Applied Clay Science, 146, 100–105.

Mata Arjona, A., Aycart Andres, J., Garcia-Martinez, O., and Cano-Ruiz, J. (1967) Basic salts VII. Thermal decomposition of copper and zinc hydroxychlorides. Anales de la Real Sociedad Española de Física y Química / Ser. B, Química, 63, 331–337.

Meng, Y., Liu, L., Zhang, D., Dong, C., Yan, Y., Volinsky, A.A., and Wang, L.N. (2019) Initial formation of corrosion products on pure zinc in saline solution. Bioactive Materials, 4, 87–96.

Merkys, A., Vaitkus, A., Butkus, J., Okulič-Kazarinas, M., Kairys, V., and Gražulis, S. (2016) {\it

COD::CIF::Parser}: an error-correcting CIF parser for the Perl language. Journal of Applied Crystallography, 49, 292–301.

Mills, S.J., Missen, O.P., and Favreau, G. (2019) The crystal structure of Ni-rich gordaite–thérèsemagnanite from Cap Garonne, France. Mineralogical Magazine, 83, 459–463.

Moezzi, A., Cortie, M.B., and McDonagh, A.M. (2013) Zinc hydroxide sulphate and its transformation to crystalline zinc oxide. Dalton Transactions, 42, 14432–14437.

Momma, K., and Izumi, F. (2011) VESTA 3 for three-dimensional visualization of crystal, volumetric and morphology data. Journal of Applied Crystallography, 44, 1272–1276.

Mouanga, M., and Berçot, P. (2010) Comparison of corrosion behaviour of zinc in NaCl and in NaOH solutions; Part II: Electrochemical analyses. Corrosion Science, 52, 3993–4000.

Muchová, L. (2010) Wet physical separation of MSWI bottom ash. Engineering; VSB - Technical University Ostrava. Ponsen & Looijen b.v.

Müller, U., and Rübner, K. (2006) The microstructure of concrete made with municipal waste incinerator bottom ash as an aggregate component. Cement and Concrete Research, 36, 1434–1443.

Nasdala, L., Witzke, T., Ullrich, B., and Brett, R. (1998) Gordaite [$Zn_4Na(OH)_6(SO_4)Cl{\cdot}6H_2O$]: Second occurrence in the Juan de Fuca Ridge, and new data. American Mineralogist, 83, 1111–1116.

Neuwahl, F., Cusano, G., Gómez Benavides, J., Holbrook, S., and Roudier, S. (2019) Best Available Techniques (BAT) Reference Document for Waste Incineration; Industrial Emissions Directive 2010/75/EU (Integrated Pollution Prevention and Control); EUR 29971 EN. Publications Office of the European Union, Luxembourg.

Ni, P., Li, H., Zhao, Y., Zhang, J., and Zheng, C. (2017) Relation between leaching characteristics of heavy metals and physical properties of fly ashes from typical municipal solid waste incinerators. Environmental Technology, 38, 2105–2118.

Nordberg, G.F., Fowler, B.A., and Nordberg, M., Eds. (2007) Handbook on the Toxicology of metals. Elsevier B.V.

Nuspl, A. (2009) Genesis of nonsulfide zinc deposits and their future utilization. TU Bergakademie Freiberg.

Odnevall, I., and Leygraf, C. (1993) Formation of $NaZn_4Cl(OH)_6SO_4{\cdot}6H_2O$ in a marine atmosphere.

Corrosion Science, 34, 1213–1229.

——— (1994) The formation of $Zn_4Cl_2(OH)_4SO_4{\cdot}5H_2O$ in an urban and an industrial atmosphere. Corrosion Science, 36, 1551–1559.

Ohnishi, M., Kusachi, I., and Kobayashi, S. (2007) Osakaite, $Zn_4SO_4(OH)_6{\cdot}5H_2O$, a new mineral species from the Hirao mine, Osaka, Japan. Canadian Mineralogist, 45, 1511–1517.

Okuda, T., Sugano, I., and Tsuji, T. (1975) Removal of heavy metals from wastewater by ferrite co-precipitation. Filtration and Separation, 12, 472–478.

Ong, C.B., Ng, L.Y., and Mohammad, A.W. (2018) A review of ZnO nanoparticles as solar photocatalysts: Synthesis, mechanisms and applications. Renewable and Sustainable Energy Reviews, 81, 536–551.

PACE, the Platform for Accelerating the Circular Economy (2019) The Circularity Gap Report 2019: Closing the Circularity Gap in a 9% World.

Paraskevi, C., S., P.C., and J., T.N. (2016) WTE plants installed in European cities: a review of success stories. Management of Environmental Quality: An International Journal, 27, 606–620.

Pasquet, J., Chevalier, Y., Couval, E., Bouvier, D., Noizet, G., Morlière, C., and Bolzinger, M.-A. (2014) Antimicrobial activity of zinc oxide particles on five micro-organisms of the Challenge Tests related to their physicochemical properties. International Journal of Pharmaceutics, 460, 92–100.

Pinasseau, A., Zerger, B., Roth, J., Canova, M., and Roudier, S. (2018) Best Available Techniques (BAT) Reference Document for Waste treatment Industrial Emissions Directive 2010/75/EU (Integrated Pollution Prevention and Control); EUR 29362 EN. Publications Office of the European Union, Luxembourg.

Prosek, T., Thierry, D., Taxén, C., and Maixner, J. (2007) Effect of cations on corrosion of zinc and carbon steel covered with chloride deposits under atmospheric conditions. Corrosion Science, 49, 2676–2693.

Quina, M.J., Santos, R.C., Bordado, J.C., and Quinta-Ferreira, R.M. (2008a) Characterization of air pollution control residues produced in a municipal solid waste incinerator in Portugal. Journal of Hazardous Materials, 152, 853–869.

Quina, M.J., Bordado, J.C., and Quinta-Ferreira, R.M. (2008b) Treatment and use of air pollution control residues from MSW incineration: An overview. Waste Management, 28, 2097–2121.

Quina, M.J., Bordado, J.C.M., and Quinta-Ferreira, R.M. (2009) The influence of pH on the leaching behaviour of inorganic components from municipal solid waste APC residues. Waste Management, 29, 2483–2493.

Quina, M.J., Almeida, M.A., Santos, R., Bordado, J.M., and Quinta-Ferreira, R.M. (2014a) Compatibility analysis of municipal solid waste incineration residues and clay for producing lightweight aggregates. Applied Clay Science, 102, 71–80.

Quina, M.J., Bordado, J.M., and Quinta-Ferreira, R.M. (2014b) Recycling of air pollution control residues from municipal solid waste incineration into lightweight aggregates. Waste Management, 34, 430–438.

Quina, M.J., Bontempi, E., Bogush, A., Schlumberger, S., Weibel, G., Braga, R., Funari, V., Hyks, J., Rasmussen, E., and Lederer, J. (2018) Technologies for the management of MSW incineration ashes from gas cleaning: New perspectives on recovery of secondary raw materials and circular economy. Science of the Total Environment.

Quirós, M., Gražulis, S., Girdzijauskaitė, S., Merkys, A., and Vaitkus, A. (2018) Using SMILES strings for the description of chemical connectivity in the Crystallography Open Database. Journal of Cheminformatics, 10, 23.

Rajamathi, M., Thomas, G.S., and Kamath, P.V. (2001) The many ways of making anionic clays. Journal of Chemical Sciences, 113, 671–680.

Rastsvetaeva, R.K., Aksenov, S.M., Chukanov, N. V., and Verin, I.A. (2012) Crystal structure of a new mineral lahnsteinite $Zn_4(SO_4)(OH)_6{\cdot}3H_2O$. Crystallography Reports, 57, 737–741.

Regenspurg, S., Feldbusch, E., Byrne, J., Deon, F., Driba, D.L., Henninges, J., Kappler, A., Naumann, R., Reinsch, T., and Schubert, C. (2015) Mineral precipitation during production of geothermal fluid from a Permian Rotliegend reservoir. Geothermics, 54, 122–135.

Rewitzer, C., and Hochleitner, R. (1989) I minerali delle antiche scorie di Laurion, Grecia. Rivista Mineralogica Italiana, 1, 21-38.

Richards, A.W. (2019) Zinc processing. Encyclopædia Britannica, inc., online: https://www.britannica.com/technology/zinc-processing/Ores, date accessed: 07.09.2021.

Rujiwatra, A., Kepert, C.J., Claridge, J.B., Rosseinsky, M.J., Kumagai, H., and Kurmoo, M. (2001) Layered cobalt hydroxysulfates with both rigid and flexible organic pillars: Synthesis, structure, porosity, and cooperative magnetism. Journal of the American Chemical Society, 123, 10584–10594.

Sabbas, T., Polettini, A., Pomi, R., Astrup, T., Hjelmar, O., Mostbauer, P., Cappai, G., Magel, G., Salhofer, S., Speiser, C., and others (2003) Management of municipal solid waste incineration residues. Waste Management, 23, 61–88.

Sager, D. (2007) Lösungsprozesse und Transport leichtlöslicher Salze in Monodeponien für Rückstände aus der Müllverbrennung. Ludwig-Maximilians-Universität München.

Samanta, P.K., and Mishra, S. (2013) Wet chemical growth and optical property of ZnO nanodiscs. Optik, 124, 2871–2873.

Samanta, P.K., Saha, A., and Kamilya, T. (2015) Morphological and optical property of spherical ZnO nanoparticles. Optik, 126, 1740–1743.

Santana, J.J., Fernández-Pérez, B.M., Morales, J., Vasconcelos, H.C., Souto, R.M., and González, S. (2012) Characterization of the corrosion products formed on zinc in archipelagic subtropical environments. International Journal of Electrochemical Science, 7, 12730–12741.

SCCS Scientific Committee on Consumer Safety (2012) Opinion on Zinc oxide (nano form). online https://ec.europa.eu/health/scientific_committees/consumer_safety/docs/sccs_o_103.pdf, date accessed: 07.09.2021

Schlumberger, S. (2010) Neue Technologien und Möglichkeiten der Behandlung von Rauchgasreinigungsrückständen im Sinne eines nachhaltigen Ressourcenmanagements.

Schlumberger, S., and Bühler, J. (2013) Metallrückgewinnung aus Filterstäuben der thermischen Abfallbehandlung nach dem FLUREC-Verfahren, 377–397.

Schlumberger, S., Schuster, M., Ringmann, S., and Koralewska, R. (2007) Recovery of high purity zinc from filter ash produced during the thermal treatment of waste and inerting of residual materials. Waste Management & Research, 25, 547–555.

Schlüter, J., Klaska, K.-H., Friese, K., Adiwidjaja, G., and Gebhard, G. (1997) Gordaite, $NaZn_4(SO_4)(OH)_6Cl{\cdot}6H_2O$, a new mineral from the San Francisco Mine, Antofagasta, Chile. Neues Jahrbuch für Mineralogie - Monatshefte, 1997, 155–162.

Schneidewind, U. (2018) Die Große Transformation. Eine Einführung in die Kunst gesellschaftlichen Wandels. Fischer Verlag, Frankfurt am Main.

Schnorrer-Köhler, G. (1991a) Mineralogische Notizen V. Aufschluss 39, 153-168.

——— (1991b) Mineralogische Notizen V. Aufschluss 42, 155-171.

Schulze, G. (2016) Grwoth Within: a circular economy vision for a competitive Europe. online: https://ellenmacarthurfoundation.org/growth-within-a-circular-economy-vision-for-a-competitive-europe, date accessed: 07.09.2021.

Schulze, S. (2019) Abfall- und Kreislaufwirtschaft im Kontext der Agenda 2030. In E. Herlyn and M. Lévy-Tödter, Eds., Die Agenda 2030 als Magisches Vieleck der Nachhaltigkeit: Systemische Perspektiven pp. 179–197. Springer Fachmedien Wiesbaden, Wiesbaden.

Silpa, K., Lisa C., Y., Perinaz, B.-T., and Frank, V.W. (2018) What a Waste 2.0 : A Global Snapshot of Solid Waste Management to 2050, 1st ed., World Bank, Washington.

Speiser, C., Baumann, T., and Niessner, R. (2001) Characterization of municipal solid waste incineration (MSWI) bottom ash by scanning electron microscopy and quantitative energy dispersive X-ray microanalysis (SEM/EDX). Fresenius' Journal of Analytical Chemistry, 370, 752–759.

Stanimirova, T., Petrova, N., and Kirov, G. (2016) Thermal decomposition of zinc hydroxy-sulfate-hydrate minerals. Journal of Thermal Analysis and Calorimetry, 125, 85–96.

Stanimirova, T. (2019) Exchange reactions of zinc hydroxide-sulfate minerals in halide solutions. Applied Clay Science, 168, 396–408.

Stanimirova, T., Kerestedjian, T., and Kirov, G. (2017) Dehydration and rehydration of Zn-hydroxy sulfate minerals with interrupted decorated hydroxide sheets. Applied Clay Science, 135, 16–26.

Stanimirova, T., Delcheva, Z., and Petrova, N. (2018) New phase obtained at mutual transformations of zinc hydroxy-salts. Bulgarian Chemical Communications, 50, 63–72.

Stegemann, J.A. (2014) The potential role of energy-from-waste air pollution control residues in the industrial ecology of cement. Journal of Sustainable Cement-Based Materials, 3, 111–127.

Studt, F., Behrens, M., Kunkes, E.L., Nygil, T., Zander, S., Tarasov, A., Schumann, J., Frei, E., Varley, J.B., Abild-Pedersen, F., and others (2015) The Mechanism of CO and CO_2 Hydrogenation to Methanol over Cu-Based Catalysts. ChemCatChem, 7, 1105–1111.

Sverdrup, H.U., Olafsdottir, A.H., and Ragnarsdottir, K.V. (2019) On the long-term sustainability of copper, zinc and lead supply, using a system dynamics model. Resources, Conservation & Recycling: X, 4.

Tamaura, Y., Gyong Sun Chyo, and Katsura, T. (1979) The Fe_3O_4-formation by the 'Ferrite Process': Oxidation of the reactive $Fe(OH)_2$ suspension induced by sucrose. Water Research, 13, 21–31.

Tamaura, Y., Katsura, T., Rojarayanont, S., Yoshida, T., and Abe, H. (1991) Ferrite Process; Heavy Metal Ions Treatment System. Water Science and Technology, 23, 1893–1900.

Tandon, K., and Heuss-Aßbichler, S. (2021a) Fly ash from municipal solid waste Incineration - from industrial residue to resource for zinc. In H. Pöllmann, Ed., Industrial wastes - Characterization, Modification and Applications of Residues pp. 379–402. De Gruyter, Berlin, Boston.

——— (2021b) Low-temperature synthesis of ZnO from saline aqueous solutions. Journal of Solid State Chemistry, submitted.

Tandon, K., John, M., Heuss-aßbichler, S., and Schaller, V. (2018) Influence of Salinity and Pb on the Precipitation of Zn in a Model System. Minerals, 8, 1–16.

Tang, J., and Steenari, B.M. (2015) Solvent extraction separation of copper and zinc from MSWI fly ash leachates. Waste Management, 44, 147–154.

——— (2016) Leaching optimization of municipal solid waste incineration ash for resource recovery: A case study of Cu, Zn, Pb and Cd. Waste Management, 48, 315–322.

Tang, J., Petranikova, M., Ekberg, C., and Steenari, B.M. (2017) Mixer-settler system for the recovery of copper and zinc from MSWI fly ash leachates: An evaluation of a hydrometallurgical process. Journal of Cleaner Production, 148, 595–605.

Thanh, N.T.K., Maclean, N., and Mahiddine, S. (2014) Mechanisms of Nucleation and Growth of Nanoparticles in Solution. Chemical Reviews, 114, 7610–7630.

Thomas, S., Birbilis, N., Venkatraman, M.S., and Cole, I.S. (2012) Corrosion of Zinc as a Function of pH. Corrosion, 68, 15009.

United Nations (2015) Resolution A/RES/70/1 adopted by the General Assembly on 25 September 2015 – Transforming our world: the 2030 Agenda for Sustainable Development. Outcome document of the united Nations summit for the adoption of the post-2015 development agenda.

Vera, R., Guerrero, F., Delgado, D., and Araya, R. (2013) Atmospheric Corrosion of Galvanized Steel and Precipitation Runoff from Zinc in a Marine Environment. Journal of the Brazilian Chemical Society, 24.

Wang, L., Jamro, I.A., Chen, Q., Li, S., Luan, J., and Yang, T. (2015) Immobilization of trace elements in municipal solid waste incinerator (MSWI) fly ash by producing calcium sulphoaluminate cement after carbonation and washing. Waste Management & Research, 34, 184–194.

Wang, L., Wu, W., Sun, W., Yang, Z., Wang, S., and Liu, G. (2019) Partially dehydrated zinc hydroxide sulfate nanoplates reinforced coating for corrosion protection. Chemical Engineering Journal, 373, 8–22.

WBGU - German Advisory Council on Global Change (2016) Humanity on the move : Unlocking the transformative power of cities. Berlin.

Weibel, G. (2017) Optimized Metal Recovery from Fly Ash from Municipal Solid Waste Incineration. Universität Bern.

Weibel, G., Eggenberger, U., Schlumberger, S., and Mäder, U.K. (2017) Chemical associations and mobilization of heavy metals in fly ash from municipal solid waste incineration. Waste Management, 62, 147–159.

Weibel, G., Eggenberger, U., Kulik, D.A., Hummel, W., Schlumberger, S., Klink, W., Fisch, M., and Mäder, U.K. (2018) Extraction of heavy metals from MSWI fly ash using hydrochloric acid and sodium chloride solution. Waste Management, 76, 457–471.

Wikipedia (2008) Zinc Oxide. online: https://en.wikipedia.org/wiki/Zinc_oxide, date accessed: 07.09.2021

Wilson, D.C., Rodic, L., Modak, P., Soos, R., Rogero, A.C., Velis, C., Iyer, M., and Simonett, O. (2016) Global Waste Management Outlook. (D.C. Wilson, Ed.) Global Waste Management Outlook. United Nations Environment Programme (UNEP) and International Solid Waste Association (ISWA).

Wu, C., Qiao, X., Chen, J., and Wang, H. (2007) Controllable ZnO morphology via simple template-free solution route. Materials Chemistry and Physics, 102, 7–12.

Wypych, F. (2004) Chemical Modification of Clay Surfaces. In F. Wypych and K.G.B.T. Satyanarayana, Eds., Clay Surfaces: Fundamentals and Applications Vol. 1, 1–56. Elsevier.

Yin, K., Ahamed, A., and Lisak, G. (2018) Environmental perspectives of recycling various combustion ashes in cement production – A review. Waste Management, 78, 401–416.

Youcai, Z. (2017) Pollution Control and Resource Recovery: Municipal Solid Wastes Incineration Bottom Ash and Fly Ash, (Z. Youcai, Ed.). Butterworth-Heinemann, Oxford.

Youcai, Z., Lijie, S., and Guojian, L. (2002) Chemical stabilization of MSW incinerator fly ashes. Journal of Hazardous Materials, 95, 47–63.

Zacco, A., Borgese, L., Gianoncelli, A., Struis, R.P.W.J., Depero, L.E., and Bontempi, E. (2014) Review of fly ash inertisation treatments and recycling. Environmental Chemistry Letters, 12, 153–175.

Zhang, W., and Yanagisawa, K. (2007) Hydrothermal synthesis of zinc hydroxide chloride sheets and their conversion to ZnO. Chemistry of Materials, 19, 2329–2334.

Annex

Table A.1: Analysis of the "leachate wastewaters" treated after FLUWA at MSWI plant Ingolstadt, Germany, in the sampling period from 2016 - 2020. n.d. stands for not determined.

Element	WW G-1	WW G-2	WW G-3	WW G-4	WW G-5	WW G-6	WW G-7	WW G-8	WW G-9
Zn [mg/l]	3570.0	1650.0	711.4	2614.8	1772.3	1426.4	2517.1	3351.6	1988.2
Pb [mg/l]	1780.0	204.0	69.7	964.9	169.8	215.4	634.1	190.5	106.8
Cu [mg/l]	26.6	13.2	5.26	600.4	8.2	n.d.	4.58	n.d.	11.2
Cd [mg/l]	67.5	230.0	17.2	33.3	29.7	20.0	48.1	44.4	34.3
Na [mg/l]	32200	22500	n.d.	21000	29300	23200	41400	26600	22000
K [mg/l]	6730.0	7780.0	n.d.	4589.5	8463.3	3918.8	6581.9	10012.5	6410.2
Ca [mg/l]	4340.0	3450.0	n.d.	7882.2	5800.1	1967.6	757.5	n.d.	5361.9
SO_4 [mg/l]	2550	3000	1450	1900	1750	4220	15800	n.d.	1550
Cl [mg/l]	72000	60000	69000	71000	64000	43000	63000	n.d.	55000

Table A.2: Analysis of the wastewaters from a Swiss MSWI plant. WW CH-1 was collected directly after the FLUWA process, and the samples ZEM CH 1-3 were sampled after cementation.

Element	WW CH-1	ZEM CH-1	ZEM CH-2	ZEM CH-3
Zn [mg/l]	12909.5	12353.1	14050.6	14761.5
Pb [mg/l]	71.57	7.14	6.06	6.15
Cu [mg/l]	357.94	-	-	-
Cd [mg/l]	96.1	0.98	1.05	1.11
Na [mg/l]	25500	24200	24600	25200
K [mg/l]	10630	10100	10100	10500
Ca [mg/l]	806.5	777.0	740	780
SO_4 [mg/l]	11780	11800	11800	-
Cl [mg/l]	67700	64700	62900	59200

Table A.3: Initial Zn-concentration, reaction temperature, Eh-pH, and main phases of the experiments that were used to construct the empirical Eh-pH diagram for concentrations > 70000 mg/l, SO_4 concentrations 2200 – 5440 mg/l, and at temperatures ≤ 40 °C (Figure 5.41a) of chapter 5.4.

Initial Zn-concentration [mg/l]	Reaction temperature [°C]	pH after experiment	Eh after experiment [mV]	Main Phase*
2000	30	11,2	-39,7	Ca-Zinkate
2000	30	11,5	0,3	Ca-Zinkate
4000	30	9,3	135,9	Gordaite
4000	30	9,2	148,8	Gordaite
4000	30	9,3	141,5	Gordaite
4000	30	9,4	122	Gordaite
4000	30	9,5	97,2	Gordaite
4000	30	9,4	128,3	Gordaite
4000	30	9,3	117	Gordaite
4000	30	9,3	136,3	Gordaite
4000	30	9,2	136	Gordaite
2000	30	9,5	132,8	Gordaite
2000	30	9,8	165	Gordaite
2000	30	9,8	184,8	Gordaite
2000	30	10,1	4,5	Gordaite
2000	30	9,5	140,3	Gordaite
2000	30	9,8	172,9	Gordaite
2000	30	9,3	58,6	Gordaite
2000	30	9,7	188,9	Gordaite
2000	30	9,4	178,2	Gordaite
2000	30	9,5	56,3	Gordaite
2000	30	9,9	106,2	Gordaite
2000	30	9,9	194	Gordaite
2000	30	9,7	203,6	Gordaite
2000	40	9,2	-44,5	Gordaite
2000	35	10,8	-41,8	Zincite
2000	35	10,2	-17,8	Zincite
2000	35	10,7	-25,6	Zincite

* The main phase was determined by XRD and FTIR. The mentioned phase is only the main phase; other phases in low proportions may occur.

Table A.4: Initial Zn-concentration, reaction temperature, Eh-pH, and main phases of the experiments that were used to construct the empirical Eh-pH diagram for concentrations > 70000 mg/l, SO_4 concentrations 2200 – 5440 mg/l, and at temperatures > 40 °C (Figure 5.41b) of chapter 5.4.

Initial Zn-concentration [mg/l]	Reaction temperature [°C]	pH after experiment	Eh after experiment [mV]	Main Phase*
2000	35	10,8	-41,8	Zincite
2000	35	10,2	-17,8	Zincite
2000	35	10,7	-25,6	Zincite
2000	50	10	-61,7	Zincite
2000	60	9,4	-19,4	Zincite
2000	65	9,2	96,8	Zincite
2000	70	9,3	24,2	Zincite
2000	80	9,3	-263,5	Zincite

* The main phase was determined by XRD and FTIR. The mentioned phase is only the main phase; other phases in low proportions may occur.

Table A.5: "Annahmekatalog Qualitätsmerkmale" (2010) displaying the minimum requirements of the smelter Befesa Zinc Freiberg for the recycling of Zn-containing residues.

Anlage 2: Qualitätsparameter

Die zinkhaltigen Materialien haben einen Zinkgehalt von mindestens

5 Masseprozent

aufzuweisen.

Die Inhaltsstoffe in den Vorlaufmaterialien sind wie folgt begrenzt:

– Nickel	**12 Masseprozent**
– Atemgängige pulverförmige Nickelverbindungen (Nickelmonoxid, Nickeldioxid, Nickelsulfid, Trinickeldisulfid, Dinickeltrioxid)	**< 0,1 Masseprozent**
– Chrom und seine Verbindungen, angegeben als Cr	**12 Masseprozent**
– Kadmium und seine Verbindungen, angegeben als Cd	**1 Masseprozent**
– Arsenoxid, Arsensäure und/oder ihre Salze, bezogen auf Arsen(V)-oxid und angegeben als As	**< 0,06 Masseprozent**
– Chlor und seine Verbindungen, angegeben als Cl	**12 Masseprozent**
– Fluor und seine Verbindungen, angegeben als F	**10 Masseprozent**
– Schwefel als Sulfitgehalt, angegeben als **SO_3-S**	**5 Masseprozent**
– Quecksilber und seine Verbindungen, angegeben als Hg	**0,02 Masseprozent**
– organische Stoffe -Bestandteil an brennbarem Material, ausgenommen der Anteil elementaren Kohlenstoffs	**15 Masseprozent**
– Dioxine und Furane	**5000 ng/kg**